Optical properties and development of flat-surface nanostructured gradient index micro-optical vortex phase components

by

Hue Thi Nguyen

UNIVERSITY OF WARSAW

Faculty of Physics

Dissertation presented for the degree of Doctor of Philosophy

Supervisor: Prof. dr. hab Ryszard Buczyński
Co-supervisor: Dr. Krzysztof Switkowski

October 2021

Abstract

The dissertation discusses new prospects for tailoring the properties of optical beams. Specifically, its intensity profile and the phase structure can be modified using developed, flat-surface nanostructured gradient index (nGRIN) micro-components. Both surfaces of the nGRIN micro-components are flat and this unique property enabled novel functionalities of such a phase element.

The thesis mainly focuses on nanostructured Vortex Phase Masks (nVPM), which are designed with the use of effective medium theory and simulated annealing approximation method. Cost-effective modified stack-and-draw nanostructurization was used in the fabrication process. In contrast to Spiral Phase Plates, nVPMs rely only on the internal refractive index gradient, and thereby there is no need for spiral relief on its surfaces. This makes its optical performance not affected by different surrounding media. The mask can be immersed in air, water, ethanol or any other transparent liquids and resulting vortex beam will have the same value of the topological charge. In addition, the dissertation aims at novel fiber-based devices such as fiber-vortex microprobe converters. Furthermore, the design of its improved achromatic version for generation of white-vortex beams was proposed. The vortex fiber probe has high application potential in optical trapping and particle manipulation as well as in laser micromachining. The flat-surface nVPM element can be used as a component of an all-fiber laser vortex beam generator, which can be integrated with an fiber laser resonator. The fiber vortex generator is a compact and reliable device compatible with the fiber technology.

The first part of the dissertation is devoted to the theoretical study on nGRIN VPMs in order to improve the optical quality of the generated optical vortex beam. There is a need for optimization because GRIN VPMs suffer from the light wave-guiding effect leading to the azimuthally non-uniform light intensity distribution in the resulted vortex beam. The effect is a consequence of the azimuthal refractive index profile of the mask. In the profile, there is one area along the radius of abrupt refractive index change, and light tends to concentrate in the highest refractive index area of the mask. The influence of the refractive index contrast of component glasses, effective refractive profile distribution of the masks on the intensity distribution, and phase structures of the generated vortices are studied. Numerical simulations employing Fourier Transform-based Beam Propagation Method were used to validate potential methods of improving the intensity profile of the vortex beam. Eventually, we proved that the best approach so far in this matter is using two types of glass with a large refractive index difference which allows the fabricated mask to be very thin. Lesser thickness minimizes the effect of light waveguiding in the nVPM mask. Research done in scope of the thesis showed that the further improvement can be obtained by making azimuthal gradient of refractive index of the GRIN mask described by power functions. Furthermore, it is possible to utilize the nanostructured phase mask to generate the vortex beam with relatively high topological charges.

The second part of the dissertation focuses on optical experiments performed to evaluate the quality of the generated vortex beams by means of developed nGRIN VPMs. The sample-set consists of our in-house developed nVPMs with different mask thicknesses. The optical performance of one of the selected nVPMs was evaluated in different transparent media air, water, and ethanol to show nVPM's advantage over SPP. We used two experimental techniques to measure topological phase characteristics of the generated vortex beam: the astigmatic transformation and Mach-Zehnder interferometry. Through comprehensive theoretical analysis

and experiments, we proved the robustness of the nVPMs in optical vortex generation vortex beams up to topological charge two. The main advantage of this kind of the phase element (optical performance preservation in any transparent external media) is explained with appropriate theory.

The next part of the dissertation describes the development and characterization of a novel fiber-based microprobe consisting of a 28-μm thick nGRIN VPM integrated at the end of an optical fiber. Specifically, regular single-mode optical fiber operating at the wavelength of 633 nm was used. The additional coreless fiber was designed and assembled with the probe to expand the beam on the mask's surface. Experimental and theoretical studies proved that the probe efficiently converts fiber-guided fundamental mode into the optical vortex beam with a single topological charge. It is worth mentioning, the optical performance of the complete vortex-fiber probe was not affected by immersion in air, water, or any uniform, transparent media. This is not possible for other already reported fiber-based systems, which use conventional SPP relief. The research results also confirm the compatibility of the proposed nanostructurization method with fiber technology, which gives high application potential. In particular, the probe could substantially simplify and improve the reliability of optical set-ups used for optical trapping or particle manipulation. Moreover, fiber-based vortex probe could be beneficial in future vortex beam applications in optical telecommunication. Due to the high laser damage threshold of the mask's materials, the probe's all-glass structure makes it a perfect candidate for vortex beam converter for laser micromachining applications.

Finally, another essential improvement of nGRIN VPMs is presented. The nVPM was redesigned in order to gain achromatic properties. The improved mask aims at white-vortex beams, which is a very vibrant subject in the field of singular optics. It enables generation of optical vortices at multiple wavelengths, all having the exact topological charges. This is achieved by carefully selecting the glass pair to fabricate the mask, those having proper refractive index dispersion curves. It was motivated by the experience of our research team in developing nGRIN microlenses with minimized axial chromatic aberrations. Besides proper refractive index difference profile of glass materials, it has to meet other nVPM fabrication constraints. Furthermore, the designed and optimized white vortex binary mask structure has been prepared for the fiber drawing process.

Streszczenie

Rozprawa doktorska dotyczy nanostrukturyzowanych światłowodowych mikrokomponentów optycznych typu GRIN (nGRIN) - nanostrukturyzowanych masek wirowych. Gaussowska wiązka laserowa po przejściu przez taki element fazowy zamieniana jest na wiązkę wirową. Mikrokomponenty nGRIN są płaskie, a ta unikalna właściwość maski wirowej otwiera nowe możliwości zastosowań takich elementów fazowych w różnych dziedzinach fotoniki. Maski zaprojektowane z wykorzystaniem teoria ośrodka efektywnego oraz Metoda symulowanego wyżarzania. Maski zostały wykonane metoda mozaikowa, która pozwala na ekonomiczne wykonanie takich elementów w produkcji masowej. W przeciwieństwie do klasycznych spiralnych masek wirowych (SPP), zasada działania masek nVPM bazuje na gradiencie współczynnika załamania światła szkła z którego jest ona wykonana. Z tego powodu nie ma potrzeby wykonywania precyzyjnego reliefu na powierzchni szkła. Maska nVPM ma dzięki temu ważną zaletę, zmiana ośrodka w jakim zostanie ona zanurzona nie wpływu na jakość generowanego wiru optycznego. Raz zaprojektowana maska w powietrzu jak i np. w wodzie lub etanolu wygeneruje taką samą wiązkę wirową o dokładnie tej samej wartości ładunku topologicznego.

Na bazie maski, w ramach niniejszej pracy zaprojektowano i wykonano światłowodową mikrosondę do generacji wirów optycznych. Sonda ta została w pełni wykonana w technice światłowodowej. Światłowodowe mikro sondy generujące wiązki wirowe mają wysoki potencjał aplikacyjny w półapkowaniu optycznym, optycznej manipulacji cząsteczkami a także w laserowej mikroobróbce powierzchni. Płaskość powierzchni masek to także duże ułatwienie w tworzeniu bardziej zaawansowanych systemów światłowodowych do generacji wirów optycznych, np. maska nVPM może być stosowana wewnątrz wnęki laserów włóknowych.

W ramach niniejszej pracy dokonano analizy możliwości wykonania achromatycznej maski wirowej do generacji tzw. białych wirów optycznych. Maska fazowa umożliwiająca generację białych wirów optycznych jest bardzo pożądanym elementem optycznym gdyż dotychczas istnieją nieliczne metody generacji takich wirów. Maski do generacji białych wirów mogłyby znaleźć zastosowanie przy źródłach super-continuum i laserach generujących ultrakrótkie impulsy światła.

Pierwsza część pracy poświęcona jest badaniom nad optymalizacją gradientu maski w celu poprawy jednorodności profilu wiązki wirowej. Badania te umotywowane są pewną niedoskonałością masek nVPM. W gradientowej masce wirowej jest zlokalizowany obszar w postaci linii o najwyższym współczynniku załamania światła i graniczy on bezpośrednio z analogicznym o najniższym współczynniku załamania światła, w związku z tym światło jest prowadzone w obszarze o wyższym współczynniku. Skutkuje to nierównomiernym rozkładem intensywności wiązki wirowej. W związku z tym, przedstawiono dwa kierunki poprawy jakości wiązek uzyskiwanych za pomocą masek do generacji wirów optycznych: wykonanie możliwie najcieńszych masek z zastosowaniem szkieł o dużej różnicy współczynnika załamania światła oraz stosując azymutalny nieliniowy profil zmiany współczynnika załamania światła w masce.

W pracy przedstawiono wyniki przeprowadzonych symulacji komputerowych, które pokazują wpływ różnicy współczynników załamania światła szkieł maski oraz jej grubości na jednorodność intensywności wiązki wirowej oraz rozkład jej fazy. Do symulacji wykorzystano metodę propagacji wiązki (ang. Beam Propagation Method) z wykorzystaniem transformacji Fouriera. Na tej podstawie ustalono, że najlepiej jest wybrać szkła o jak największej różnicy współczynników załamania światła, która umożliwi realizację najcieńszej maski fazowej, co zminimalizuje efekt

lokalnego prowadzenia światła. Ponadto na podstawie wyników symulacji, pokazano że jednorodność intensywności wiązki wirowej można poprawić stosując gradient współczynnika załamania światła w masce opisany funkcją potęgową. Wyniki symulacji pokazały także, że w przypadku masek nVPM możliwe jest uzyskanie wirowych wiązek optycznych o stonkowo wysokich ładunkach topologicznych.

Druga część rozprawy skupia się na metodach eksperymentalnych przeprowadzonych w celu weryfikacji jakości generowanych wirów optycznych za pomocą masek nVPM. Zbadane próbki stanowią maski wykonane z jednego rodzaju włókna nastrukuryzowanego, ale maski nVPM przygotowano o różnych grubościach. Maski te zbadano w trzech różnych ośrodkach - powietrzu, wodzie oraz w etanolu. Eksperymenty przeprowadzono w celu zweryfikowanie głównej cechy wyróżniającej maski gradientowych na tle klasycznych płytek spiralnych.

Do zbadania charakterystyki wiązek wirowych wykorzystano dwie metody eksperymentalne: transformację astygmatyczną oraz interferencją w konfiguracji Macha-Zehndera. Wynikom eksperymentów towarzyszą wyniki symulacji metodą BMP przeprowadzone dla warunków analogicznych tym w eksperymencie. W ten sposób przedstawiono faktyczne możliwości generacji wiązek wirowych za pomocą masek GRIN o wartości ładunku topologicznego jeden i dwa. Ostatecznie eksperymentalnie i teoretycznie, pokazano brak wpływu zmiany współczynnika załamania światła zewnętrznego ośrodka wokół maski na jakość generowanych wiązek.

Następnie opisano konstrukcję i wykonanie innowacyjnej mikrosondy optycznej bazującej na masce fazowej nVPM umieszczonej na końcu światłowodu. Do konstrukcji mikrosondy wykorzystano klasyczny światłowód jednodomowy. Ponadto, niezbędne było zastosowanie dodatkowego element miedzy końcem światłowodu a maską – mikro pręta szklanego, który ma na celu rozszerzyć wiązkę, tak aby całkowicie wypełnić wiązką aperturę maski. Także na przykładzie sondy pokazano, że po jej zanurzeniu w jednorodnej przejrzystej cieczy nie zmienia się jakość generowanej wiązki wirowej. Obecnie istniejące tego typu mikrosondy światłowodowe bazują na reliefie SPP i nie posiadają takiej ciekawej własności. Wykonana sonda potwierdza kompatybilność masek gradientowych z technologią światłowodową i stanowi dużą wartość aplikacyjną. Poza wcześniej wymienionymi aplikacjami warto dodać że rozwiązanie światłowodowe zwiększa potencjał aplikacyjny masek wirowych w telekomunikacji optycznej. Ponadto, mikrosonda jest wykonana wyłącznie z elementów szklanych czyniąc ją odporną na duże moce promieniowania laserowego i z tego powodu może ona znaleźć zastosowanie w mikroobróbce laserowej.

Ostatnia część pracy dotyczy własności achromatycznych masek nVPM. Jest to niezbędna cecha potrzebna do stworzenia maski do generacji białego wiru optycznego. Własności achromatyczne można poprawić dzięki precyzyjnemu doborowi pary szkieł w procesie tworzenia maski. Pomysł ten jest konsekwencją tego, że nasz zespół posiada doświadczenie w tworzeniu achromatycznych mikrosoczewek GRIN. Poza wymogiem co do krzywych dyspersji współczynnika załamania szkieł, muszą one spełnić inne pozostałe wymogi technologiczne. W ramach pracy wykonano i zweryfikowano projekt achromatycznej maski nVPM

Acknowledgments

First and foremost, I would like to express my profound gratitude to my academic supervisor, Prof. dr hab. inż. Ryszard Buczyński, for giving me an opportunity to work in the field of nonlinearoptics and photonics. I greatly appreciate the knowledge and skills that he imparted on me. I am and will be forever grateful of the all-out suppor, guidance, motivation, and advice throughout my Phd studies.

I wish to express my sincere gratitude to my supervisor Dr. inż. Krzysztof Świtkowski for his exceptional patience, support and fruitful scientific discussions.

I would like to express my sincere thanks to Dr hab. Rafał Kasztelanic, Dr. Adam Filipkowski, Dr. Alicja Anuszkiewicz for patiently assisting me in the works during my studies. I truly appreciate for the knowledge, experience and advices that they shared in this project.

I wish to express my gratitude to Prof. Wieslaw Krolikowski for valuable insights about singular optics and valuable discussions.

I would like to express my sincere thanks to Mr. Darek Pysz for supporting and expertise on the fabrication process of nanostructured components and fibers.

I would like to express my gratitude to Hong Duc University for supporting me to do my PhD in Poland.

I would also like to thank all the colleagues in my laboratory for their friendship, support and encouragement not only in science but also in daily life which made my days in Poland easy.

Finally, I would like to express my sincere thanks to my parents, sisters in Vietnam; Prof. Van Cao Long in Poland for their continuous support and encouragement. I am particularly grateful to my husband Dr. Hieu Van Le and my daughter Bao Tram Le for their understanding, love, and continuous encouragement, which is the source of my strength to fulfill this PhD dream.

The research has been carried out under the project POIR.04.04.00-00-1C74/16 (TEAM TECH 2016-1/1) operated within the Foundation for Polish Science Team Programme co-financed by the European Regional Development Fund under Smart Growth Operational Programme.

List of publications

The following publications resulted from the work on this dissertation:

Journal publications:

1. R. Buczynski, A. Filipkowski, B. Piechal, H. T. Nguyen, D. Pysz, R. Stepien, A. Waddie, M. R. Taghizadeh, M. Klimczak, and R. Kasztelani, "Achromatic nanostructured gradient index microlense", *Opt. Express* **27**(7), 9588-9600 (2019).
2. A. Filipkowski, H. T. Nguyen, R. Kasztelanic, J. Cimek, R. Stępień, D. Pysz, M. Trippenbach, and R. Buczynski, "Development of large diameter nanostructured GRIN microlenses enhanced with temperature-controlled diffusion", *Opt. Express* **27**(24), 35052-35064 (2019).
3. H. T. Nguyen, K. Switkowski, R.Kasztelanic, A. Anuszkiewicz, A. Filipkowski, H. V. Le, D. Pysz, R. Stepien, W. Krolikowski and R. Buczynski, "Optical characterization of single nanostructured gradient index vortex phase masks fabricated by the modified stack-and-draw technique", *Opt. Commun.* **463**, 125435 (2020).
4. H. T. Nguyen, A. Anuszkiewicz, J. lisowska A. Filipkowski, R. Kasztelanic, R. Buczynski and W. Krolikowski, "Numerical analysis of optical vortices generation with nanostructured phase masks", *Opt. Express*, **28**(14), 21143-21154 (2020).
5. H. T. Nguyen, K. Switkowski, A. Filipkowski, R. Kasztelanic, D. Pysz, H. V. Le, R. Stepien, W. Krolikowski and R. Buczynski, "Fiber microprobe with integrated gradient index vortex mask", *Opt. Commun*. **477**, 126345 (2020).
6. H. T. Nguyen, K. Switkowski, A. Filipkowski, R. Kasztelanic, and A. Anuszkiewicz, R. Kasztelanic, D. Pysz, H. V. Le, B.V. Chu, R. Stepien, W. Krolikowski, and R. Buczynski, "All-fiber nanostructured gradient optics vortex beam converter," *Opt Lasers Eng.* **150**, 106841 (2022).

Conference contributions:

1. H. T. Nguyen, A. Anuszkiewicz, A. Filipkowski, R. Kasztelanic, D. Pysz, A. Waddie, M. R. Taghizadeh and R. Buczynski, "Experimental analysis of nanostructured gradient index microlens", in *18th Conference on Optical fiber and their applications (TAL 2018)*, 20-23 November 2018, Nałęczów – Lublin, Poland. Oral presentation was given by H.T. Nguyen.
2. A. Filipkowski, R. Kasztelanic, H. T. Nguyen, J. Cimek, R. Stępień, Dariusz Pysz, M. Trippenbach, R. Buczynski, "Development of nanostructured GRIN microlenses with temperature-controlled diffusion", in *conference of Photonic and Phononic Properties of Engineered Nanostructures IX*, Proc. SPIE 109270N, 4 March 2019. Oral presentation was given by A. Filipkowski.
3. H.T. Nguyen, K. Switkowski, A. Anuszkiewicz, A. Filipkowski, D. Pysz, R. Stepien, W. Krolikowski and R. Bunczynski, "Numerical and experimental study on nanostructured gradient index vortex phase mask", in *International conference on New Trends in Contemporary Optics*, 22-29 September 2019, Vinh, Vietnam. Oral presentation was given by H.T. Nguyen.
4. R. Buczynski, A. Anuszkiewicz, M. Franczyk, A. Filipkowski, T. Osuch, D. Pysz, T. Stefaniuk, G. Stepniewski, D. Michalik, H. T. Nguyen, M. Klimczak, R. Kasztelanic, "Progress in Development of Nanostructured Gradient Index Optical Fibers and Micro-

Optical Components", in *21st International Conference on Transparent Optical Networks (ICTON)*, 2019. Oral presentation was given by R. Buczynski.

5. H.T. Nguyen, K. Switkowski, R. Kasztelanic, A. Anuszkiewicz, A. Filipkowski, D. Pysz, R. Stepien, W. Krolikowski, R. Buczynski, "Optical Vortex Generation by Nanostructured Vortex Phase Plates Integrated with Single-Mode Fibers", in *2019 IEEE 2nd British and Irish Conference on Optics and Photonics (BICOP),* 11-13 December 2019, London, UK. Oral presentation was given by H.T. Nguyen. ***This presentation was awarded with an Outstanding Contribution Prize for the outstanding contribution to BICOP2019.***
6. H.T. Nguyen, K. Switkowski, R. Kasztelanic, A. Anuszkiewicz, A. Filipkowski, H.V Le, D. Pysz, R. Stepien, W. Krolikowski, R. Buczynski, "Generation optical vortex beam in Liquid media using novel nanostructured vortex phase masks", in *15th Jubilee Conference Integrated Optics – Sensors, Sensing Structures and Methods (IOS'2020)*, 24-28.February 2020, Szczyrk, Poland. Oral presentation given by H.T. Nguyen.
7. H. T. Nguyen, K. Switkowski, A. Filipkowski, R. Kasztelanic, D. Pysz, H. V. Le, R. Stepien, W. Krolikowski and R. Buczynski, "Converting Gaussian beams into optical vortices in water with an integrated vortex-fiber probe", in *IEEE ICCE 2020 - 8th International conference on communication and electronic*, 13-15 January 2021, Phu Quoc, Viet Nam. Poster presentation was given by H. T. Nguyen.
8. H.T. Nguyen, A. Filipkowski, K. Switkowski, D. Pysz, W. Krolikowski, R. Buczynski, "Fiber System with Nanostructured Components for Generation of Optical Vortex Beam", in *2021 Conference on Lasers and Electro-Optics/Europe – European Quantum Electronics Virtual Conferences* CLEO®/Europe-EQEC 2021, 21-25 June 2021. Oral presentation was given by H.T. Nguyen.

Journal publications out of the scope of this thesis:

1. H.V. Le, V.L. Cao, H.T. Nguyen, A. M. Nguyen, R. Buczyński, and R. Kasztelanic, Application of ethanol infiltration for ultra-flattened normal dispersion in fused silica photonic crystal fibers, *Laser Phys*. **28** (2018) 115106.
2. H.V. Le, V. T. Hoang, H. T. Nguyen, V. C. Long, R. Buczynski, and R. Kasztelanic, "Supercontinuum generation in photonic crystal fibers infiltrated with tetrachloroethylene," *Opt. Quantum Electron*. **53**, 187 (2021).
3. H.V.Le, V.T Hoang, T.C Le, Q.D. Ho, H.T. Nguyen, M.N.T. Vo, M. Klimczak, R. Buczynski, and R. Kasztelanic, "Silica-based photonic crystal fiber infiltrated with 1,2-dibromoethane for supercontinuum generation," *Appl. Opt.* **60**, 7268-7278 (2021)

List of acronyms

BPM (FFT BPM) – Fast Fourier Transform-based Beam Propagation Method

EMT – effective medium theory

GRIN – Gradient index

HG – Hermitte-Gaussian mode

LG – Laguerre-Gaussian mode

NA – Numerical aperture

Nanorod – Rod with the cross-section diameter in nano-scale

nVPM (nGRIN VPM) – nanostructured gradient index vortex phase mask

nWVPM – Nanostructured gradient index white vortex phase mask

OAM – Orbital angular momentum

OVB – Optical vortex beam

SAM – Simulated annealing approximation method

SEM – Scanning Electron Microscopy

SLM – Spatial light modulator

SPP – Spiral phase plate

STED – Stimulated emission depletion

TC – Topological charge

VPM (GRIN VPM) – Gradient index vortex phase mask

WVPM – Gradient index white vortex phase mask

Contents

Chapter 1. Introduction

Optical vortex is one of the most extraordinary optical phenomena discovered during last three decades. An optical vortex beam (OVB) has a phase singularity at the center of its wavefront. The wave front rotates with respect to the beam axis and forms a helical structure in three-dimensional space. The vortex beam cross-sectional intensity pattern has an annular shape which remains intact while propagating [1–3]. Moreover, optical vortex beams carries new form of light momentum - orbital angular momentum (OAM) which is directly related with the phase structure of the beams of the azimuthally rotated phase of light beam.

The term of "optical vortex" was first used for this unique beam in a theoretical study of Coullet et. al. [4] in 1989. However, it was initially introduced in a work on screw dislocation lines in wave-trains reported by two physicists, J. Nye and M. Berry in 1974 [5]. To date, OVBs with such unique optical properties have been a subject of intense study enabling great novelties for numerous scientific research fields and found many possibilities for applications [6,7]. The most prominent OVB application is in nonlinear microscopy for which OVB enabled a significant increase of resolution of the imaging. The improved methods is Stimulated Emission Depletion (STED) microscopy [8,9], which authors were awarded the Nobel Prize in Chemistry in 2014. Important applications also include optical trapping and manipulation of micro-particles by transferring OAM from light to particles [10–13] which is useful in Biomedicine [14] and chemistry [15], to name a few. Equally impressive are applications in optical communication [16,17], in particular, OVB multiplexing expands data storage, capacity. In quantum information, OAM-carrying beams make data processing faster and with higher security [18–20]. Moreover, tightly focused helical beams meet requirements for working in laser micromachining to create nano/micro patterns on surfaces of many materials [21]. OVBs have also contributed to advanced techniques in the field of astronomy like optical vortex coronagraph [22,23].

There is high demand of reliable methods for generating optical vortices. The early method for direct generation of OVBs is in laser cavity [24]. The OVBs are subset of Laguerre-Gauss beams (LG), there by precisely controlled misaligned laser cavity can generate OVBs. However, the most common generation method of OVBs is to use optical phase elements for the beam phase control by transmission, diffraction or reflection of fundamental light beams. The main principle of operation of the conventional free-space converters is directly imposing a helically phase structure onto incident waves [25,26]. It is also worth mentioning about spiral phase plates (SPPs) [27–32], q-plates [33], computer-generated holograms [34], and spatial light modulators (SLMs) [35–38]. Among those methods, the liquid-crystal SLM is the most often used due to their considerable advantages. It offers arbitrary phase patterns which can be changed dynamically many times per second to suite different experiment requirements. However, there are some applications for which SLMs cannot be used due to limitations of input power and its working efficiency due to its large footprint. Moreover, its high cost and need for external power supply are also serious downsides of SLM technique. Another solution is to use micro-optical SPPs. The most often, SPPs are made by means of nanolithography and approximated by finite number discrete steps [27]. Recently optimized SPPs with more precise step heights and microscopic size can be fabricated by different high-cost advanced techniques, for instance, electron beam lithography [29–31]; laser nanopolymerization writing techniques [32]. However, material dispersion also contributes to major limitations on the operating bandwidth of such a plate.

Generating optical vortices via bulky free-space systems of discrete optical components often suffers from low purity of spatial modes, losses, alignment and stability issues which maybe serious problems in technical applications. This leads to further requirements of simplifying sophisticated bulk discrete element system for micro-vortex creation setups. As a consequence, all-fiber vortex generators have appeared and been an attracted topic for physicists [39–48]. Recently, the most attractive and widely used techniques is the helical fiber Bragg grating [41] and mode selective couplers [44]; graded-index few mode fiber [40]. Recently, there have been special designed fibers aiming at not only generation but also low-lost transmission of vortex beams, for instance, all-fiber optical systems using polarization-maintaining and ring-core fibers [47] or chiral periodic structures [48]. However, the demand of specific design of those fibers practically restricts the distance of OVB transfer.

Continuous interest in this topic, some groups have recently reported the successful generations of micro-optical vortex beams through a phase structure fabricated directly onto the tip of conventional single-mode optical fibers [49–51]. However, those works are expensive since it requires the use of advanced techniques, for example, a focused ion beam [49] or femto-second 3D direct laser writing [50] or two-photon polymerization [51]. Moreover, as mentioned, the plates are of staircase-surface shape – not continuous – and limit input power of the beam. Especially, a SPP is fabricated for the use in specific external medium which is inconvenient if we need the same OVB to work in different media.

In recent years, we have proposed an alternative cost-effective stack-and-draw approach with nanostrucurization technique for mass fabrication of flat-surface nanostructured gradient index (nGRIN) micro-optical components. This approach was conventionally used for fabrication of photonic crystal fiber and initially developed for realization of nGRIN microlens done by F. Hudelist [52]. Since then it has been employed for developing numerous nanostructured optical components with different functionalities. They include large-diameter GRIN lens [53], elliptic gradient index microlenses [54,55], nGRIN axicons [56], nGRIN vortex phase masks [57]. Those micro-optical components consist of thousands of spatially distributed sub-wavelength rods made of two different glasses to form arbitrary refractive index profile for producing effectively continuous phase profiles. They perform unique optical properties. In particular, having flat-parallel surfaces, they are able to be directly integrated with optical fibers making an optical system robust and compact which allow easier manipulation of the generated beams in 3D space [58,59]. In addition, the optical properties of those nanostructured components are defined by their internal nanostructure. Thus, their properties are not influenced by the refractive index of transparent external media which is extremely advantageous for their potential applications. It is promising to use the same components in different experimental media. Very similarly, our nGRIN vortex phase masks (nVPMs) for vortex generation which have been presented for the first time by Krzysztof Switkowski in 2017 posses such unique properties. However, that work focused on the designed, fabrication and initial test for OVB generations in free space. Moreover, the presented vortices are not perfect - azimuthally non-uniform light intensity distribution due to the wave-guiding effects. This can restrict the possibility of their applications, particularly, in applications with requirement of high uniformity of the beam intensity such as micro-machining for surface or bulky structures [16]. Therefore, it seems that the nVPMs have more optical properties and novel potential developments would need to be extensively investigated.

The motivation of this work is to deeply study on optical performance of selected nanostructured GRIN micro-components and their developments based on nanostructurization technique and effective medium theory. In particular, both numerical simulation and experiments are carried out to study the functionalities of nGRIN VPMs in shaping light into optical vortex beams in different external transparent media such as air, water, ethanol liquids. Besides that, possibilities to overcome the limitation in the quality of generated OVBs are the subjects of the thesis research. Influences of effective refractive profile distribution, refractive index contrast of component glasses and topological charge values on intensity distribution and phase structures of the vortex beams are investigated numerically. In addition, this work also aim to develop a new micro-optical system – a fiber-based vortex converter that is able to efficiently converts fiber guided fundamental mode into an optical vortex with single topological charge no matter in air or water. Lastly, the new nGRIN VPM for formation of achromatic optical vortices, called white-vortex, is also proposed in here. Such a new micro-optical mask is designed and its performance is numerically tested for different wavelengths.

1.1 Thesis objectives

The main objectives of this dissertation are to study optical performance of the nanostructuterd GRIN VPMs for deeper understanding of its properties. Moreover, developments of new fiber-based micro-optical probes exploiting such the VPMs and a new designed white-vortex mask are also aimed at in the scope of the work. The key objectives in here are listed as following:

Thesis 1. *The microscopic optical vortex beams with various topological charge values can be generated in air and liquid media by using the same nano-srtuctured gradient index components. The problem of the light waveguide effect inside the gradient phase components, which accounts to the non-uniformity of the beam intensity profile, can be mitigated.*

Thesis 2. *Fiber-based vortex converter microprobe with the integrated gradient index vortex mask allows the efficient conversion of the Gaussian beam into the vortex beam.*

Thesis 3. *Achromatic vortex beams can be obtained by using nGRIN vortex mask made of glasses with matched material dispersive properties.*

1.2 Outline of dissertation

This dissertation is divided into eight chapters, including this introduction. The fundamental knowledge of optical vortex beams is given in chapter 2. The overview of concept and development technology of nanostructured gradient index vortex phase masks is presented in Chapter 3. Chapter 4, 5, 6, 7 contain my original contributions to the field and they are directly related to verification of the mentioned thesises of my dissertation. The presentation of the topics is organized as follows:

Chapter 2 provides an overview of optical vortices. Their unique optical properties include the phase singularity at the center of the helicoidal spatial wavefront which is associated orbital angular momentum. Then typical vortex verification techniques are briefly shown herein. I also introduce standard approaches for OVB generation basing on vortex phase components and vortex fiber designs. Finally, I discuss various promising applications in different field of science and technology due to extraordinary properties of the optical vortex beams.

Chapter 3 introduces the novel concept and realization of nanostructured gradient index vortex phase masks. Main tools for design and structure optimization are described in detail, which include effective medium Maxell-Garnett theory and simulated annealing method. The selections of materials and exploiting stack-and-draw technique for fabrication of nVPM are also presented at the later part of this chapter. This chapter mainly bases on the knowledge of previous reports [52,57] and a recent results on development of fabrication approach by controlling material diffusion [60]. My main contribution was related to the development of the preform and I also participated in fiber drawing process. I performed measurements of the fabricated components and data analysis of the obtained results. The result of this work was published on Optics Express Vol. 27(24), pp. 35052-35064 (2019).

Chapter 4 contains results of my original contributions in the theoretical study on nanostructured GRIN VPMs for the quality improvement of generated optical vortices to verify Thesis 1. I did theoretical calculation and performed modeling optimization as well as analyzed the obtained results. This study addressed limitations existing in previous reported work done by Krzysztof Switkowski et. al. [57]. The fundamental of Fast Fourier Transform-based Beam Propagation Method (BPM) employed for numerical simulations of beam propagating through the VPMs and then in external media is presented. Additionally, a new parameter called quality parameter Q is proposed in order for easier comparisons of uniformity of vortex intensity distribution. In this chapter, the influence of effective refractive profile distribution, refractive index contrast of component glasses and topological charge values on intensity distribution and phase structures of the vortex beams is analyzed. The results of this work were published in Optics Express Vol. 28, pp. 21143-21154 (2020) [61].

Chapter 5 contains my original contributions in theoretical and experimental investigations of the optical performance of fabricated nanostructured gradient index vortex phase masks in various external media for verification of Thesis 1. In particular, I performed the modeling analysis, developed the experimental setup and conducted experimental investigations as well as data analysis. In this chapter, I presents a brief description of geometrical properties of the selective fabricated VPM samples is introduced. Then the results from a set of computer simulations modeling light propagation through both the designed binary nanostructured pattern and ideal continuous GRIN vortex phase masks are presented. Following, the experimental results are presented and compared with the mentioned theoretical predictions to verify the optical performance of such fabricated nVPMs. It should be noticed that all tests are conducted firstly in the air and then in different liquid media, specially: water and ethanol. Moreover, this chapter also presents results of numerical simulation as well as experimental verifications of generation of the microscopic optical vortices with different topological charges utilizing our fabricated nGRIN VPMs which have the same designed structure but varied thicknesses. The results of this work were reported in Optics communications Vol. 463, pp. 125435 (2020) [62].

Chapter 6 presents an application of nVPM in fiber optics as a new integrated fiber-based vortex converter which are results of my original contributions for verification of Thesis 2. I did integration process and numerical as well as experimental investigations of optical performance of the fiber-based vortex converters. Such an integration of nVPM with the fiber tip was made for the first time which will be described in detail herein. Both experimental and theoretical verifications are presented and confirm that the probe efficiently converts fiber guided fundamental mode into an optical vortex beam of single topological charge. In addition, comparison of the optical performance of the fiber-based vortex converter in the different external media such as air and water are also discussed. The results of this work were published in Optics communications Vol. 477, pp. 126345 (2020) [63] and in Optics and lasers in Engineerings [64].

Chapter 7 presents my original results to verify Thesis 3 on a new version of nGRIN VPMs allowing generation of white-vortex beam. The chapter introduces consideration needed for successful development of chromatically corrected optical elements. The concept of white vortex beam generator is partially based on our previous work devoted to achromatic nanostructured GRIN microlens for near-infrared spectral windows which was reported in Optics Express Vol. 27(7), pp. 9588-9600 (2019) [65]. For this purpose, an appropriate pair of soft glass materials which are mechanically and thermally matched for practically joining in drawing process is specified. Their refractive index difference has to be optimized to make nGRIN VPMs with technically achievable thickness. Results of the numerical verifications of achromatic characteristics of optical vortices generated by the nVPM element will be presented. My main contribution in the work on achromatic nanostructured GRIN microlens was related to the development of the preform and I also participated in fiber drawing process and experimental investigations. For the part of the chapter related to development of the white vortex beam generator, I did the theoretical calculation, design and optimized the nanostructure of the developed component. I also performed modeling optimization of analysis on its optical performance.

Chapter 8 presents the dissertation conclusions and also suggestions for future research and potential applications of nGRIN VPMs, fiber-bases vortex converter microprobe and its achromatic version.

Chapter 2. Optical vortex beams

This chapter presents fundamentals of optical vortex beams. They are the most recognizable representatives of the singular optics which is vibrant field over the last three decades. Firstly, I introduced the novel optical properties of OVBs such as doughnut-like intensity distribution; phase singularity surrounded by the helicoidal spatial wavefront and associated with it the orbital angular momentum. Then typical detection techniques for OVBs are briefly shown herein. I also introduce standard approaches for optical vortex generation basing on surface plates and fiber designs. Finally, I discuss various promising applications in different field of science and technology due to the unique properties of the optical vortex beams.

2.1 Optical properties of vortex beams

Generally, vortices which are commonly seen in nature and often used in science possess a rotational flow of surrounding media having a singularity at the vortex core. In optics, a vortex is a helical electromagnetic wave beam with the phase singularity on its wavefront – a remarkable feature of OVBs. Consequently, the intensity on the propagating axis of those light fields vanishes. And then their cross-sectional intensity pattern has an annular shape which remains during propagation and exists no matter how tightly the beam is focused [1–3].

J. Nye and M. Berry in 1974 [5] observed screw dislocation lines in wave-trains which are analogous to the phenomenon appearing in imperfect crystals. Those lines have indeterminable phase leading to the vanishing of intensity amplitude of the beam. In 1989, Coullet and his group members coined the term "*optical vortex*" named for describing a special laser mode created in its cavity [4]. They pointed out the presence of phase singularity of the light field as a solution of Maxwell-Bloch equations. Afterward, there have been tremendous studies on optical vortices and related effects that led to the establishment of a new branch of modern physical optics – *singular optics* [26,66–68]. Here, the word "singular" refers phase behavior at the null intensity location of the field. For a simple mathematical explanation let consider a scalar monochromatic wave field $U(\mathbf{r}, \omega)$. It is possible to re-write this complex field into two terms: real parts $U_R(\mathbf{r}, \omega)$ and imaginary part $U_I(\mathbf{r}, \omega)$ which can be transformed into real amplitude and phase parts $A(\mathbf{r}, \omega)$ and $\psi(\mathbf{r}, \omega)$, respectively:

$$U(\mathbf{r},\omega)= U_R(\mathbf{r},\omega)+ iU_I(\mathbf{r},\omega)=A(\mathbf{r},\omega)e^{i\psi(\mathbf{r},\omega)}.$$

In case the field intensity amplitude equal to zero, i.e., $A(\mathbf{r}, \omega) = 0$, then phase $\psi(\mathbf{r}, \omega)$ is indeterminable, or dislocation occurs. The zero of wave field is always a point in the 2D cross-sectional plane. In 3D-space, its structure can be described by a line which is circulated around by the wave-field phase helicoids. The confirmation of OVBs is based on those unique properties.

A simplest well-known form of OVBs is the family of scalar monochromatic Laguerre–Gauss beams which are obtained by solving the scalar Helmholtz equation [69]:

$$(\nabla^2 + k^2)E = 0, \tag{2.1}$$

where the wave-number satisfies $k = 2\pi/\lambda$. In cylindrical coordinates, the typical beamlike-paraxial solutions have a below general form:

$$U(r,\theta,z,t) = u(r,\theta,z)\exp[i(kz-\omega t)]. \tag{2.2}$$

Using slowly varying envelop approximation for Eq. (2.1) substituted by Eq. (2.2), we have

$$\frac{1}{r}\frac{\partial}{\partial r}\left(r\frac{\partial u}{\partial r}\right) + \frac{1}{r^2}\frac{\partial^2 u}{\partial \theta^2} + 2ik\frac{\partial u}{\partial z} = 0. \tag{2.3}$$

As a result, the LG_p^l mode solutions are able to attain by separating variables r and ϕ:

$$u(r,\theta,z) = E_0\left(\sqrt{2}\frac{r}{\omega}\right)^l L_p^l\left(2\frac{r^2}{\omega^2}\right)\frac{w_0}{w(z)}\exp[-i\varphi_{pl}(z)]\exp\left[i\frac{k}{2q(z)}r^2\right]\exp(il\theta), \tag{2.4}$$

with E_0 depicts a constant amplitude of electric field, (z) and w_0 are the beam radius of z and beam waist, respectively. The term $z_0=\pi w_0^2/\lambda$ is Rayleigh range and term $\varphi_{pl}(z) = (2p + l + 1)\tan^{-1}(z/z_0)$ Gouy phase shift and $q(z)=z-iz_0$ is a complex parameter of the beam. $L_p^l(x)$ is defined by Laguerre polynomials which satisfies the following equation:

$$x\frac{d^2L_p^l}{dx^2} - (l + 1 - x)\frac{dL_p^l}{dx} + pL_p^l = 0, \tag{2.5}$$

indices p and l are defined as the radial and azimuthal orders of the beam, respectively. Index p can only have nonnegative integer values while l can take any integers. Index l has additional quantitative meaning in AOM and in context of OVBs is called topological charge.

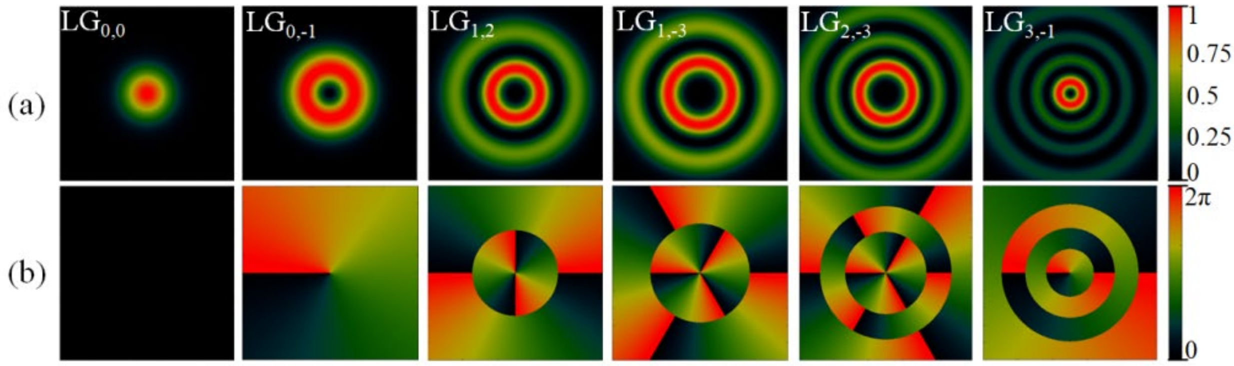

Figure 2.1 The (a) intensity and (b) phase of several Laguerre–Gauss modes.

The field intensity $|u(r,\theta,z)|^2$ and phase $\mathbf{Arg}\{u(r,\theta,z)\}$ of several $LG_{l,p}$ modes are depicted in Fig. 2.1(a) and (b), respectively. It is worth noting that different values of index p gives different number of zero intensity rings in a beam cross-sectional pattern. For example, $p = 2$ means there are 2 circular zeros.

It could be seen that for $l = p = 0$, the solution mode $LG_{0,0}$ is Gaussian beam whose phase is the same everywhere and wave front includes parallel planes. It has the form:

$$u(r,z) = E_0\frac{w_0}{w(z)}\exp[-i\varphi(z)]\exp\left[i\frac{k}{2q(z)}r^2\right], \tag{2.6}$$

where $\varphi(z) = \tan^{-1}(z/z_0)$ is the Gouy phase shift for the fundamental Gaussian beam.

In contrast to the Gaussian beam – for the integer topological charge $l \neq 0$ – all LG modes have a zero-intensity point at the beam center i.e., a phase singularity. Its phase consists of the factor $\exp(il\theta)$ which indicates the wavefronts twisted azimuthally. That means we have optical vortices.

The *topological charge l* of a spatial field region is formally defined as:

$$l = \frac{1}{2\pi}\oint_C \nabla\psi dr \tag{2.7}$$

where the integral is evaluated over a closed C and $\psi(r)$ represents the wave beam phase. For the simple case of scalar monochromatic Laguerre–Gauss beams we considered in this discussion, their intensity amplitude and phase properties would be continuous everywhere except the zero-amplitude point. This restricts the OVBs' phase to increase or decrease only in integer-multiples of 2π; consequently, the topological charge l is only integer. It should be noted that within an enclosed field region may exist more than one spiral, and hence there is a net of topological charges. However, only single-OVBs described by a topological charge of the vortex itself are considered here.

Each OVB carries a specific topological charge l whose sign introduces the singularity sign. In particular, the phase circulates clockwise if l is positive, otherwise it circulates anticlockwise. OVBs are shape-invariant during paraxial propagation. In other words, theirs basic shape and phase structure along the optical axis remains the same. In particular, the vortex dark center area is persisted no matter how far an OVB travels and is a consequence of helical structure of the wavefront. Doughnut shaped vortex beams are the simplified case of LG modes with the index $p = 0$ is selected for those simplest cases (see Fig. 2.2)

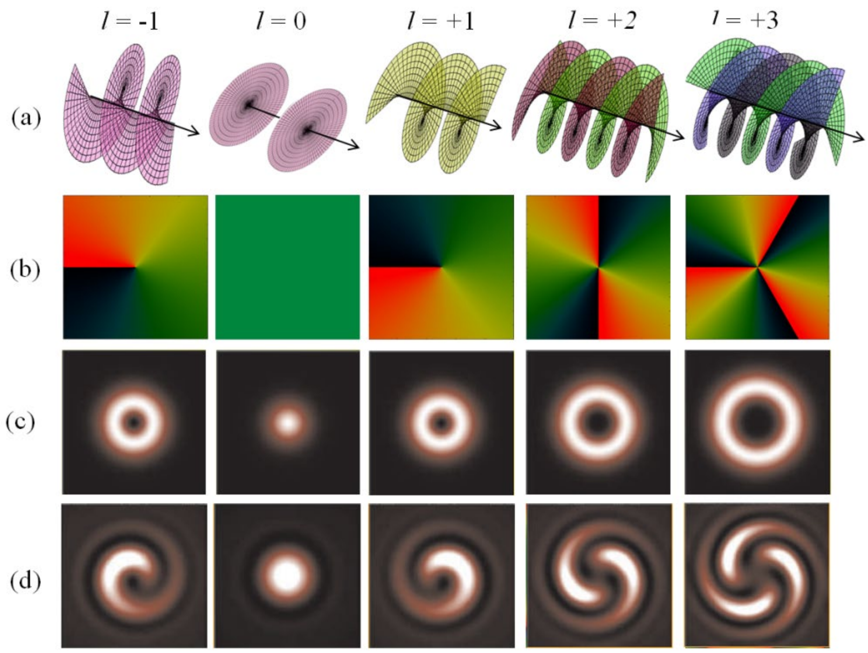

Figure 2.2 Example of some optical vortex beams having different topological charges l: 3D (a) and 2D (b) instantaneous phase structure; (c) cross-sectional intensity profile. (d) Corresponding 2D spiral intensity pattern interfered between these OVBs and a plane wave. The figure is based on [70].

Optical vortices have another unique property – each vortex beam carry orbital angular momentum (OAM) which for the first time was recognized in 1992 by Allen's group at Leiden University in Nertherlands [71]. Here it should noted that OAM is not related to spin angular momentum (SAM) which is associated with circular polarization; OAM arises as a result of the azimuthally varied phase of the light beam. The OAM carried by OVBs is totally independent of the polarization states of the beam, and its magnitude could be much greater than of SAM [70,72]. The magnitude of OAM is related to the number of turns of the helicoid in distance of a wavelength. In particular, a OVB with phase characterized by the term $\exp(il\theta)$ would have an OAM of $l\hbar$ for each photon, l is the topological charge, θ defines the azimuthal angle on the beam's cross section and $\hbar$ is Planck's constant divided by 2π [73]. OAM discovery replenished our fundamental knowledge of the theory of light. This was a crucial point when emerged further studies on novel application of OVBs.

Further, Poynting vector which is defined as the vector product of the electric and magnetic field is often used for explanation of the OAM. In free-space, the Poynting vector gives the direction and magnitude of the momentum flow. For OVB as well as for other Laguerre-Gauss modes, the electromagnetic field transverse to the phase-fronts has nonzero axial components. Equivalently, the Poynting vector, which from its definition is parallel to the normal of the surface of the wave fronts, has an azimuthal component around the beam. This local distribution of the Poynting vector results in OAM along the propagation axis.

At this point in sake of completeness it is worth mentioning other interesting class of Maxwell equations solutions. These beams are often called vector vortex beams or cylindrical beams. Vector vortex beams share common property of OVBs – they have minimum of intensity at the center. It is a result of polarization singularity. Cylindrical beams are also intensively studied filed of singular optics [69,74]. The vector Bessel-Gauss mode is a typical class of vector vortex beams with cylindrical polarization symmetry. It is derived from the full vector wave equation [69,75]:

$$\nabla \times \nabla \times \vec{E} - k^2\vec{E} = 0, \tag{2.8}$$

The general form of an axially symmetric beamlike vector solution with the electric field aligned in the azimuthal direction is as follows:

$$\vec{E}\,(r,z) = U(r,z)\exp[i(kz - \omega t)]\vec{e}_\theta, \tag{2.9}$$

with $U(r,z)$ satisfies the following equation under the paraxial and slowly varying envelope approximation:

$$\frac{1}{r}\frac{\partial}{\partial r}\left(r\frac{\partial u}{\partial r}\right) - \frac{U}{r^2} + 2ik\frac{\partial u}{\partial z} = 0. \tag{2.10}$$

The solution that obeys azimuthal polarization symmetry has the trial solution:

$$\vec{E}(r,z) = E_0 J_1\left(\frac{\beta r}{1+\frac{iz}{z_0}}\right)\exp\left[-\frac{\frac{i\beta^2 z}{2k}}{1+\frac{iz}{z_0}}\right]u(r,z)\exp[i(kz-\omega t)]\vec{e}_\theta, \tag{2.11}$$

which corresponds to the vector Bessel–Gauss beam we are looking for. In this equation, β is a constant scale parameter, $(r,)$ is known as the fundamental Gaussian solution given in Eq. (2.6) and J_1 is the first-order Bessel function of the first kind. $\vec{e}_\phi$ is the unit vector in the azimuthal direction.

Equivalently, the transverse magnetic field solution should take the form:

$$\vec{H}(r,z) = -H_0 J_1\left(\frac{\beta r}{1+\frac{iz}{z_0}}\right)\exp\left[-\frac{\frac{i\beta^2 z}{2k}}{1+\frac{iz}{z_0}}\right]u(r,z)\exp[i(kz-\omega t)]\vec{h}_\theta, \tag{2.12}$$

where H_0 is a constant amplitude of the magnetic field and $\vec{h}_\theta$ is the unit vector in the azimuthal direction. For this azimuthal magnetic field solution, the corresponding electric field in the transverse plane is aligned in the radial direction. Hence Eq. (2.12) represents the radial polarization for the electric field. Clearly there should be a z component of the electric field as well. In many applications, instead of the vector Bessel–Gauss solutions derived above, other simplified distributions have been used, especially for cylindrical vector beams with large cross sections. For very small β, the vector Bessel–Gauss beam at the beam waist can be approximated as

$$\vec{E}(r,z) = Ar\exp\left(-\frac{r^2}{\omega^2}\right)\vec{e}_i, i = r,\theta \tag{2.13}$$

The amplitude profile of these cylindrical vector beam is exactly the same as the scalar LG_{01} mode without the vortex phase term of $\exp(i\theta)$. The polarization distribution is constant for scalar and variable for vector vortex modes. This type of beams can generally be decomposed into two orthogonally polarized components. Each of the polarized components may have identical or different vortex characteristics. Examples of cylindrical vector vortex modes and scalar modes having the same topological charges are shown in Fig. 2.3.

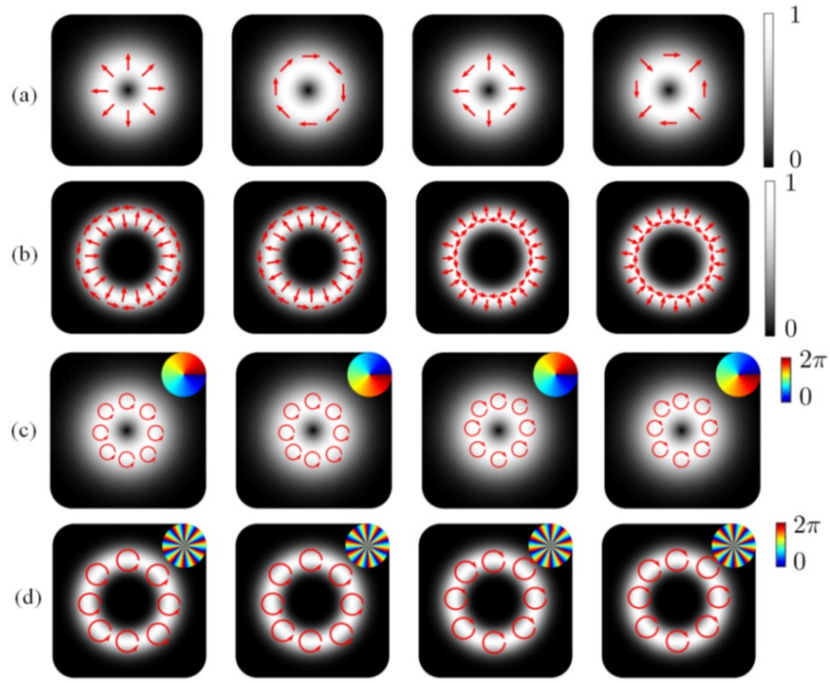

Figure 2.3 Examples of cylindrical vector vortex modes charges l = ±1 (a) and l = ±10 (b), and their corresponding OAM scalar modes (c) and (d), respectively. The insets show the phase profile of the scalar OAM modes [76].

2.2 Method used for vortex beam detection

It is not enough to classify any doughnut or annular beam as a vortex beam. Similar intensity profiles we can witness observing fiber LP modes or Bessel beams.

Moreover, two OVBs with the same value of topological charge ($LG_{0,a}$ and $LG_{0,-a}$ modes) have identical intensity profiles (see the example in Fig. 2.3 for $LG_{0,\pm1}$). Thus, a number of additional approaches that are sensitive to phase are required for accurately evaluate the vortex phase structure and measure the sign and magnitude of the topological charge (TC). Indeed, a wide range of interferometric techniques, diffraction patterns and modes transformation have been employed for this purpose [26]. In the scope of this thesis, I would like to focus on detection approaches for scalar vortex beams - class of $LG_{0,l}$ modes.

The most common technique for TC detection is to use interferometric methods because they provide more intuitive results using simpler implementation. The first practical measurement of the topological charge was published by Vaughan and Willetts in 1979 who studied the properties of light beams with a helical phase structure and their interference patterns. Although this method generates a lobe interference pattern, it does not offer a mechanism to determine the charge signs [77]. In the following years, interference structures from an OVB and a reference beam, commonly, plane wave or Gaussian beam realized in Mach-Zehnder interferometer [78,79] have been employed effectively for characterization of topological charge and phase singularity properties. In this way, interference of the OVB with the collinear reference spherical wave, leads to spiral interfering fringes in the observation plane as indicated in Fig. 2.4(b). By making a count of the number of spiral arms in the pattern and their relative orientations, the vortex order and its corresponding sign can be precisely estimated. The number of spiral arms on that structure shows the value of vortex charge. The spiral orienting clockwise/anti-clockwise indicates the vortex of positive/negative charge. In a mechanically equivalent experiment, if the reference light beam and the OVB are well collimated and tilted with respect to each other, the attained interferogram introduces the fork-like form. The fringe with bifurcation in the fork structure indicates the singularity of the phase. Moreover, the value and relative sign of the charge can be easily deduced from the fork structure by comparing a number of counted fringes at the top and the bottom of the structure. The number of additional fringes in the pattern equals to the topological charge value of the considered OVB. The handedness of the phase structure is related to the topological charge sign thereby to up or down orientation of the fork structure. Examples of fork interference patterns between single charge OVBs and Gaussian beams are shown in Fig. 2.4(c).

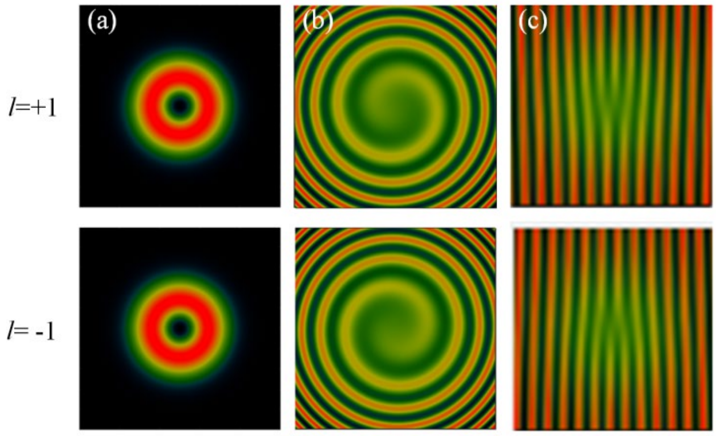

Figure 2.4 Examples of interference patterns obtained between charge $l = \pm 1$ OVBs and Gaussian reference beam: (a) collinear propagation (b) and acute angle propagation of the beams (c). These vortex beams have identical intensity profile. This figure is based on [79].

In addition, self-referenced interferometric technique has been well applied for effectively revealing the sign and magnitude of topological charge of the studied optical vortices. For instance, the input vortex beam interfering with its conjugate copy could be realized in a modified Mach-Zehnder interferometer with Dove prisms, resulting into special patterns revealing both integer and fractional topological charges up to 60 [80]. Another approach is based on an improved Fiezeau interferometry that can be realized much easily with use of a flat-concave mirror. With this, one can obtain distinct-spiral fringe patterns (see Fig. 2.5(a)) providing a convenient solution for topological charge determination [81]. Moreover, this purpose can be achieved by using structures created from interference between vortex beams and their own laterally displaced or misaligned copy [82,83]. Consequently, interferometric patterns exhibit pairs of disjoined fork-like structures as examples represented in Fig. 2.5(b).

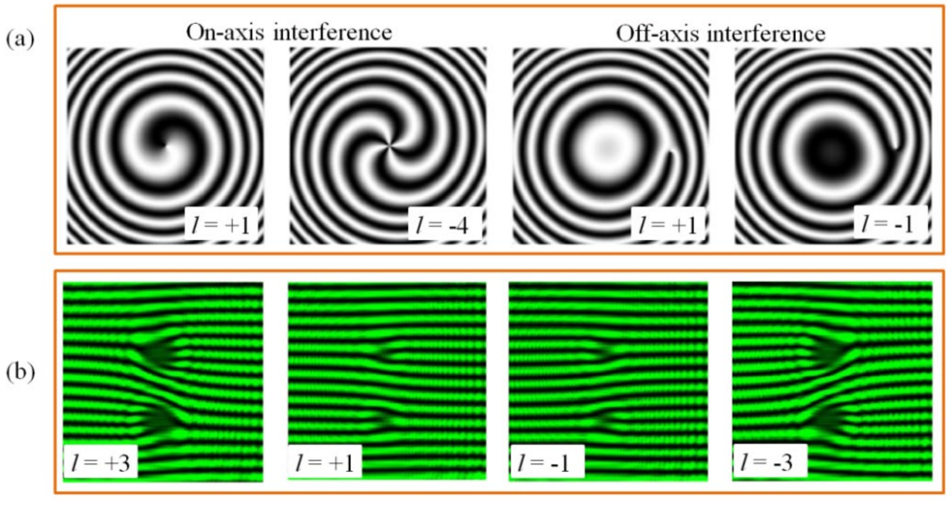

Figure 2.5 Examples of patterns of self-interference of the vortex beam realized using improved Fizeau interferometry (a) [81] and Mach-Zehnder interferometry of spatially misaligned vortex beams (b) [83].

Another practical method employed for determination of topological charge is an astigmatic vortex transformation using either cylindrical lenses or regular tilted lenses. As a result, after passing through the lens, the initially cylindrically symmetric vortex is deformed into Hermite–Gauss (HG) modes [84,85]. An OVB with charge l will be split into a pattern of l extended dark and $n = l + 1$ bright stripes. The number of dark regions indicates the charge of the OVB. For instance, for double charge vortex, the astigmatic transform pattern consists of three bright strips separated by two dark elongated lobes as shown in Fig. 2.6. Additionally, the orientation of lobes (right and left diagonal), determine the sign of the charge, equivalently, the sign of OAM orders.

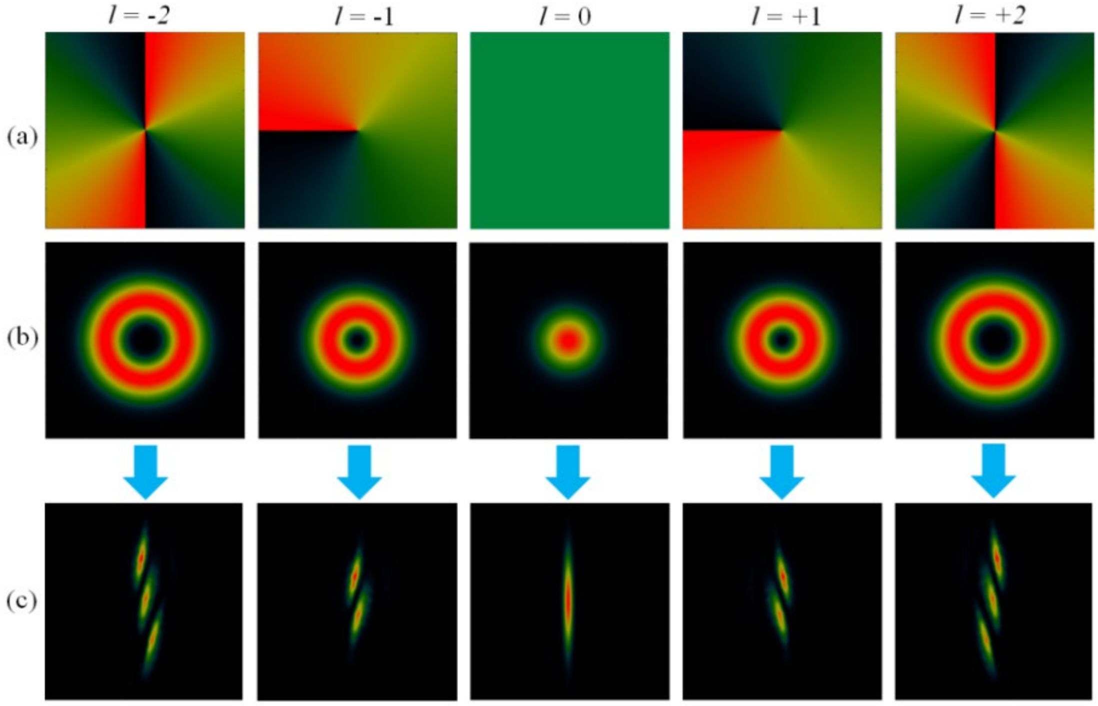

Figure 2.6 Examples of astigmatic transformation patterns (c) of some OVBs with corresponding phase (a) and intensity distribution (b). The figure is based on [85].

There have been also some other less-common methods relying on distinctive far-field diffraction intensity pattern obtained from propagation of the vortex beam through equilateral triangle aperture [86] or annular aperture [87]. In the former case, a diffraction structure associated with the topological charge l would be created. The diffraction pattern is a triangle comprised of multiple bright spots. If there are n dots in the side of the triangle, the absolute value of the OVBs' topological charge will be $l = n - 1$ (see Fig. 2.7(a)). In case of the annular aperture, the diffraction spatial pattern with bright and dark rings is formed as a consequence of optical vortex propagation through the annular aperture. An examples of diffraction patterns for OVBs charge $l = 2$ and 5 are presented in Fig. 2.7(b). It can be seen that the number of separated bright regions indicates the topological charge value of the investigated optical vortex beam.

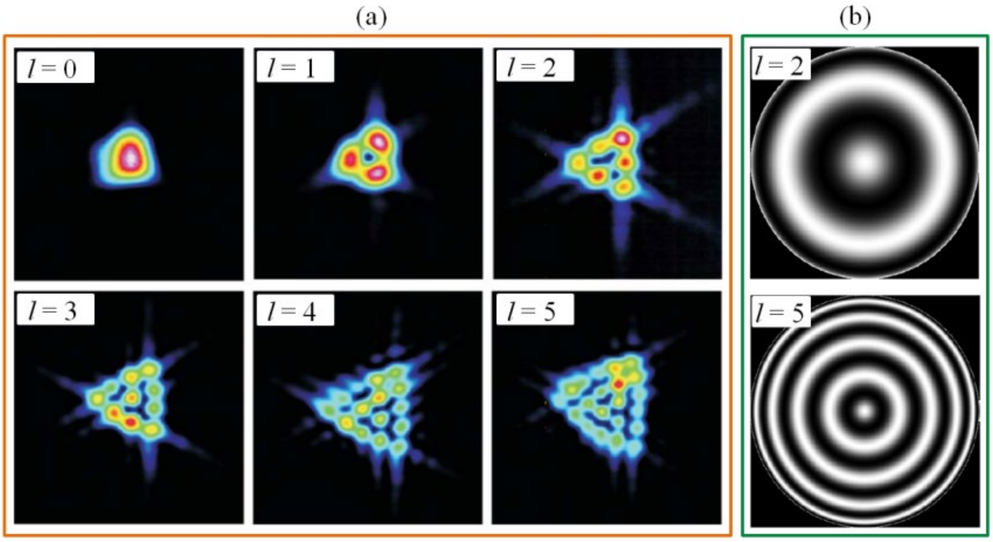

Figure 2.7 Examples of far-field diffraction intensity pattern obtained from propagation of the vortex beam through equilateral triangle aperture [86] (a) or annular aperture [87] (b).

The vortex evaluation techniques based on interference and far-field diffraction rather strongly depend on quality of the obtained characteristic patterns. Topological charge distinction can be troublesome in case of low quality vortex beams. All the aforementioned approaches work best for a pure vortex beam with integer value of the topological charge, being a single LG mode with specific indices *p, l* or a sum of modes having identical charge *l*.

In fact there are a few other techniques for distinguishing or separating vortex states of different singularity orders such as multipinhole plates [88], computer-generated holograms [89], Shack–Hartmann wavefront sensor (SHWS) [90] to name a few. However there is a need for further research to prove reliability of these methods.

2.3 Vortex beam generation

In a broad perspective, optical vortices have become important in many scientific applications as well as in technology, thereby there is a demand for efficient and reliable methods of generation of optical vortex beams [25,91]. The early practical method for direct formation of OVBs is by means of laser cavities which a very effective way to produce high power, high beam quality optical vortices with high efficiency [24]. However, the most common generation method of OVBs involves conversion of a Gaussian beam into helical beams by imposing spiral phase modulation through free-space phase elements [25,26]. This can be realized by transmission, diffraction or reflection of fundamental light beams through the phase elements, particularly, spiral phase plates (SPPs) [27–32], q-plates [33], computer-generated holograms [34]. Especially, the generation of vortex beam with a desired wavefront can be produced using spatial light modulators (SLMs) [36,37]. Recently, there is a demand for minimizing size of OVB generating elements in order to simplify some sophisticated optical systems, which rely on OVBs. Realizing them as an all fiber system needs fiber compatible vortex generators, which is recent and attractive topic of research [39–43].

The direct generation of optical vortex modes from a laser cavity involves preferential oscillation of Laguerre-Gaussian modes ($LG_{0,l}$) modes within the laser resonator, with the suppression of the lowest order Gaussian mode ($LG_{0,0}$) and the higher radial LG modes ($LG_{p,l}$). Typically it is realized in solid-state laser cavities applying several mode selection techniques. Using aperture in the pump beam allows diffractive optical pumping to excite selectively various LG modes of a laser by changing the inversion profile in the active medium [92]. Another group used wires as a clipping mask inside the cavity to force laser to produce HG modes first [93]. Then by bouncing HG in the cavity to obtain flipped HG and superposition of both gives LG modes. Another technique involves using centrally damaged cavity mirrors [94] or exploiting thermal lensing of the laser medium [95]. Moreover, vortex laser beams can be directly generated through the use of spatial light modulators within the laser cavity. In this system, an appropriate SLM is used as a resonator mirror and tailors the wave front and spatial intensity profile of the laser mode to obtain LG modes a the laser output [96,97]. However, these methods are usually sophisticated and have certain limitation. Such as, the mode degeneracy, the beam handedness selection, relatively low output power to name a few.

In addition to the use of laser cavities, it is also possible generate LG modes by converting Hermite–Gauss modes with the use of cylindrical lenses. This is one of the earliest vortex generation method considered together with the establishment of theoretical foundation for OAM in the early 1990s [71,98]. These works used a couple of cylindrical lenses as mode converters to alter the Gouy phase shift of an incident beam. In principle, any $HG_{m,n}$ modes oriented 45^{o} with respect to the cylindrical axis of the lens can be converted into $LG_{p,l}$ modes with $l = (m - n)$ and $p = \min(m, n)$ [98,99]. Furthermore, the analogy between transverse modes and polarization states extends to a description of modes and their transformation with an equivalent to the Poincare sphere [100] and Jones matrices [101]. Although this astigmatism technique offers a near lossless transformation, they suffer from two main problems. There is requirement of having high quality HG source beams, which need modifications inside the laser cavity. Also, the resulting LG modes may contain additional astigmatism caused by lens imperfections or converter misalignment. Consequently, the obtained LG modes either have a non-circular intensity cross-sectional pattern or cannot remain their high-order, OVBs instead split into multiple single vortices [102,103]. Recently, with the developed technology, the effective combination of optical vortex laser systems and cylindrical lens mode converters enabled the generation of high-order OVBs carrying large number of OAMs [104–106].

As an alternative to making complex refractive optics, diffractive optical elements are readily designed to mimic any refractive element of choice for generation of many complex optical beams including optical votices. From the early 1990s, diffractive optical elements were exploited to convert spatially coherent, flat wavefront beams into beams consisting of OVBs [107]. Here, a diffractive optical element is a modified diffraction grating which contains an edge dislocation at its center. As a consequence, after passing the element, the first order of diffracted light beam has an optical singularity indicating the formation of beam containing OVBs. Designs of such the elements might be realized either as an amplitude or phase grating, both of which, due to the edge dislocation, the resulted phase function has an additional factor of helical phase $\exp(il\varphi)$. In theoretical principle, a phase grating could transform all of the incident energy into the first diffraction order. Practically, it is not always true; a fraction of the energy indeed produces a diffracted profile including additional orders together with the first one. For the amplitude grating, each order is diffracted through a different angle, and consequently it is simple to use a spatial filter to select the first order.

Similarly, numerically computed-holograms can form OVBs carrying any desired number of OAMs from the same initial light beam. By illuminating such holograms with a plane wavefront beam, a first-order diffracted beam with the doughnut intensity and helical phase structure of the wished beam is produced [34]. It is possible to create required holograms by encoding onto photographic film the interference patterns between a plane wave and the beam we want to generate. As mentioned in the previous section, collinearly interfering between a vortex beam and a plane wave creates a spiral fringe pattern in which the number of spiral arms and their rotating direction show the value and sign of the singularity order, respectively. On other hand, when these beams are collimated and tilted to each other, the interference creates a fork grating with a clear defect on fringes indicating a phase singularity. Basing on such unique properties of these interferences, a hologram plate with spiral or the fork-like grating can be produced.

The holographic approach could be also implemented using active spatial light modulators for more efficient conversion of Gaussian beams to optical vortices [35–37]. The most important advantage of SLM is it flexibility in producing any desired phase and amplitude pattern which allows realization of digital holograms. It is remarkable that the SLMs facilitate generation real time dynamic, computer-controlled holograms for converting a fundamental light beam into an OVB with almost any target intensity and phase profiles. The use of computer-generated holograms is a one of the most convenient method in singular optics research. The most common SLM type utilized for this purpose is based on pixilated-liquid-crystals [36]. Fig. 2.8 shows principle schematic of the cross-sectional liquid-crystal-on-silicon SLM device. Moreover, it is possible to control both phase and amplitude of the created OVBs by using phase-only SLMs [37]. In this case, an additional SLM is used for correcting the phase of a holographically generated beam exploiting Gerchberg–Saxton algorithm. Recently, this technique has been successfully implemented by using the Arrizón's algorithm which provides relatively high signal-noise-ratio and requires a phase range of only < 1.17π [38].

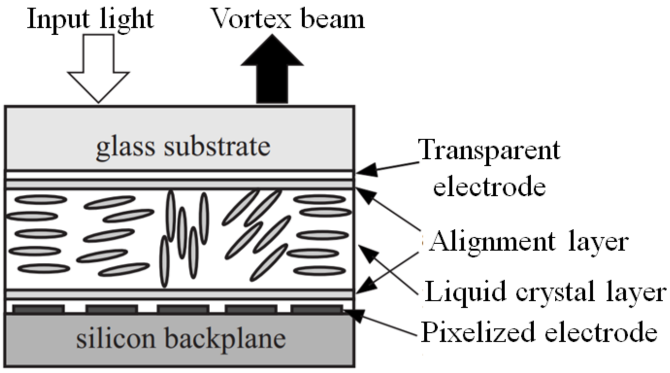

Figure 2.8. Schematic of the cross-section of a liquid-crystal-on-silicon SLM [36].

Advanced high-resolution SLMs sufficiently meet requirements even for application in optical fiber systems in which vortex converters, consequently generated OVBs, and should be of microscopic scale for being compatible with the optical fiber or other optical micro-devices. Those devices offer programmable phase pattern which is able to be changed many times per second for different experiment requirement. Spontaneously, created OVBs show their high quality due to small pixel size down to the diameter of 1.6 μm [108]. However, for some application SLMs are not suitable due to it relatively low laser damage threshold and too large footprint for micro optics integration. Moreover, the high cost of the SLM cell and external control unit is also serious downsides of using SLM technique for OVB generation.

One of the simplest and most reliable approach for OVB generation is conversion of Gaussian beam by phase element named spiral phase plates (SPPs) [27–32]. The main idea behind SPP is to add the spatially distributed phase delay in the input beam. The delay is an azimuthally gradient and realized by increasing element thickness with the azimuthal gradient making helical surface. In practical implementation, for sake of simplification, the helical surface of SSPs can be discredited into many steps as per the element shown in Fig. 2.9.

The design of stair-case-surface shape should match the material refractive index n of the SPP's material to create a 2π integer phase for a specific operating wavelength λ. In particular, a designed SSP has an optical thickness h increasing with azimuthal angle θ: $\Delta h(\theta) = \theta(n - 1)l\lambda/2\pi$. Here, l is the topological charge of the transmitted beam descibed a phase factor of $\exp(il\theta)$. The SSP needs its step height h at $\theta = 2\pi$ being precisely matched with the factor $(n\text{-}1)l\lambda$ which for visible part of electromagnetic spectrum is in a few hundred nanometers range. This makes it fabrication extremely challenging, and requires high thickness accuracy available only in advanced technology. In the initial demonstration reported by Beijersbergen et al. in [27], a SPP with total height step exceeding the theoretical value was immersed in an refractive index-matched and temperature-controlled fluid. As a result, the required index mismatch of the height step at the operating wavelength was minimized.

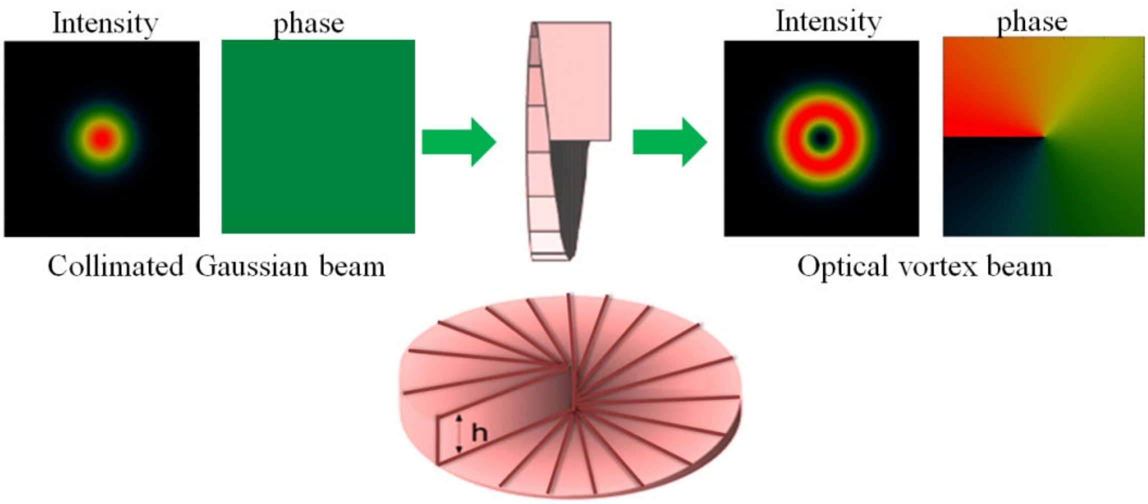

Figure 2.9. Principle scheme of SPPs for a single charge vortex generation. The figure is based on [27].

Nowadays, precise techniques are exploited to produce SPPs directly, for instance, electron beam lithography [29–31] or laser nanopolymerization writing techniques [32]. These fabrication methods enable SSPs having micro-dimensions and exactly desired step height. Despite that discretization of the mask to sufficient number of steps does not degrade much of its optical performance, the advanced lithography allows fabrication of the phase masks with true spiral surface. In case of SSPs with non-integer multiplicity of 2π in phase profile, the intensity pattern of resulted vortex structure is degraded. Such OVBs with partial topological charge are not stable in propagation, but useful for quantum entanglement [109]. The SPP form its proof of principle has limited spectral bandwidth, because its thickness matches only certain design wavelength. Dispersion of refractive index of material used for SPP also narrows the bandwidth and often hinders using the element for using for the beam harmonics (integer multiplicities of the design beams). The limited spectral bandwidth is a serious problem in applications of SPP with femtosecond or supercontinuum laser beams. To obtain good optical quality femtosecond and supercontinnum OVBs, the achromatic vortex lens should be used [28].

Generating OVBs via bulky systems of discrete optical components is troublesome and prone to misalignment. Generated vortex beams often suffer from low purity of spatial profile that maybe a serious problem in technical applications. This leads to further requirements of minimizing sizes of generated OVBs as well as optimizing vortex generator systems. As a consequence, the appearance of all-fiber vortex generators have been considered as an alternative for above mentioned methods [39–43]. Those can address existing problems of bulk optical systems of discrete components such as loss minimization, alignment and stability issues [39,40]. For example, OVBs could be efficiently generated by the use of the fiber helical Bragg grating which is directly written on a few-mode fiber path [41]. For that the helical refractive index modulation can be achieved by rotating fiber during single-side UV exposure using a phase mask. The stability and topological charge of the generated OVBs could be obtained by using fiber structure of a square core and ring refractive index profile [46]. Recently, the most attractive and widely used techniques for optical vortex generation is using mode selective coupler [44]; graded-index few mode fiber (GI-FMF) [40], and developed few-mode long-period gratings [45]. Because OVBs cannot maintain its propagation in regular fiber, there have been recent fiber designs for OVBs generation and transmission but most of them aims at vector vortex beams. There are a few fiber OVB generation methods, but the most common is using a fiber grating in conjunction with a free-space etalon [42,43]. Later studies in this field are aimed at designs with lower loss and more compact structure which allow directly generating rather high-purity OVBs from fibers with associated mode-converter inside it. For instance, all-fiber optical systems using polarization-maintaining and ring-core fibers [47] or chiral periodic structures [48] are able to generate highly-stable optical vortex beams and maintain its propagation under external environmental disturbance. However, these fibers needs specific design along its whole structure which are expensive and practically restricts the distance of OVB transfer.

There is continuous interest in research on OVB generation for fiber optics, utilizing commercially available optical fibers combined with a phase masks at the end. It is a great alternative to bulk setups or other sophisticated vortex fibers thereby became a vibrant topic inn photonics [49,50]. Recently, there have been micro-optical vortex beams generated through compact fiber-based generators [49–51]. Such a generator comprises a phase elements written directly onto the tip of a conventional single mode fiber as shown in Fig. 2.10. However, this approach is expensive since it requires the use of advanced fabrication techniques, for example, a focused ion beam [49], or femto-second 3D direct laser writing [50] or two-photon polymerization [51]. Moreover, due to the mentioned limitations of the SPP related with its geometry, dispersion and low laser damage thresholds, the use of such a fiber-SPP system is limited. Especially, a SPP is fabricated for the use in specific external medium which is inconvenient if we need a same OVB generator to work in different surrounding media.

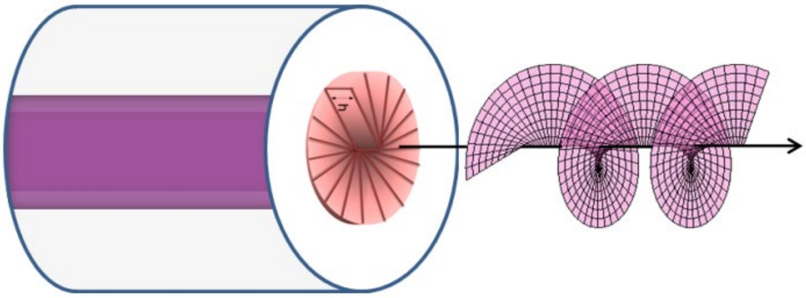

Figure 2.10. Schematic of fiber-based vortex generator with a SPP written onto the tip of a conventional optical fiber using 3D direct laser writing. This figure is based on [51]

Recently we have proposed an alternative cost-effective technique for mass fabrication of nanostructured gradient refractive index vortex masks (nVPMs) [57,62] and compact fiber-vortex probes composed of nVPMs and commercial single mode fibers [63]. The flat-surface masks with arbitrary refractive index profile consists of thousands of individual rods of sub-wavelength diameter [57,62]. A modified stack-and-draw approach have been employed for developing nGRIN masks with effectively continuous phase profiles [52,57,60]. This fiber-based method is well suited for mass production, since in one run thousand vortex masks is achieved. Importantly, these fabricated devices persist its optical properties in external environment with various refractive indices as air and liquids [62,63]. That means we can use only one device to create the same OVBs in different external environments. It was also shown that such nVPMs are compatible with optical fiber to form a compact all-fiber vortex probes for generating either focused or divergent OVBs. These are the main concern of my dissertation which are discussed in detail in following chapters

2.4 Applications of OVBs

It is natural that due to such extraordinary optical properties, OVBs have been a subject of intense study and interest for over three decades. To date, OVBs have been enabling great novelties for numerous scientific research fields - a new insight into the singular optics - and found enormous salient possibilities for technological applications and innovations [6,7]. Here, it is worth mentioning supper-resolution of optical imaging microscopy with STED technique [8,9]. OVBs also significantly contribute to optical trapping and optical manipulation of micro-particles relying on OAM transfer to matter [10–13] which is useful in biomedicine [14] and chemistry [15]. Equally impressive are the promising potential applications in optical communication [16,17] for faster transfer data rates. In quantum information, OAM-carrying beams make data processing faster and with higher security [18–20]. Moreover, helical beams with the size down to micrometers meet up requirements for laser micro-machining of various materials, making nano/micro patterns on metals and semiconductor surfaces [21]. OVBs have also contributed to advanced techniques in the field of astronomy like optical vortex coronagraph [22,23].

2.4.1 Microscopy and imaging

One of the most important application of optical vortices is in microscopy and imaging which is a vibrant research topic [8,9,110–115]. It was demonstrated that the fascinating helical wave front properties of OVBs can increase micro-imaging resolutions of phase-contrast microscopes [8]. Early studies showed several canonical examples of how the OAM beam can be used to image a variety of intrinsic and extrinsic properties encoded, e.g., in phase and amplitude gradients, dislocations or delays [110]. Since then the number of works on this topic has been rapid increasing which results in the fast development of imaging techniques and the creation of advanced microscopes using OVBs. Specifically, in 2006, Stefan Hell and his colleagues invented STED (stimulated emission depletion) microscopy technique which is a remarkable milestone of historical development in this field [9]. This work was awarded the 2014 Nobel Prize in Chemistry. In the typical STED microscopy, an OVB is coupled with an excitation for super-resolution imaging purpose as depicted in Fig 2.11.

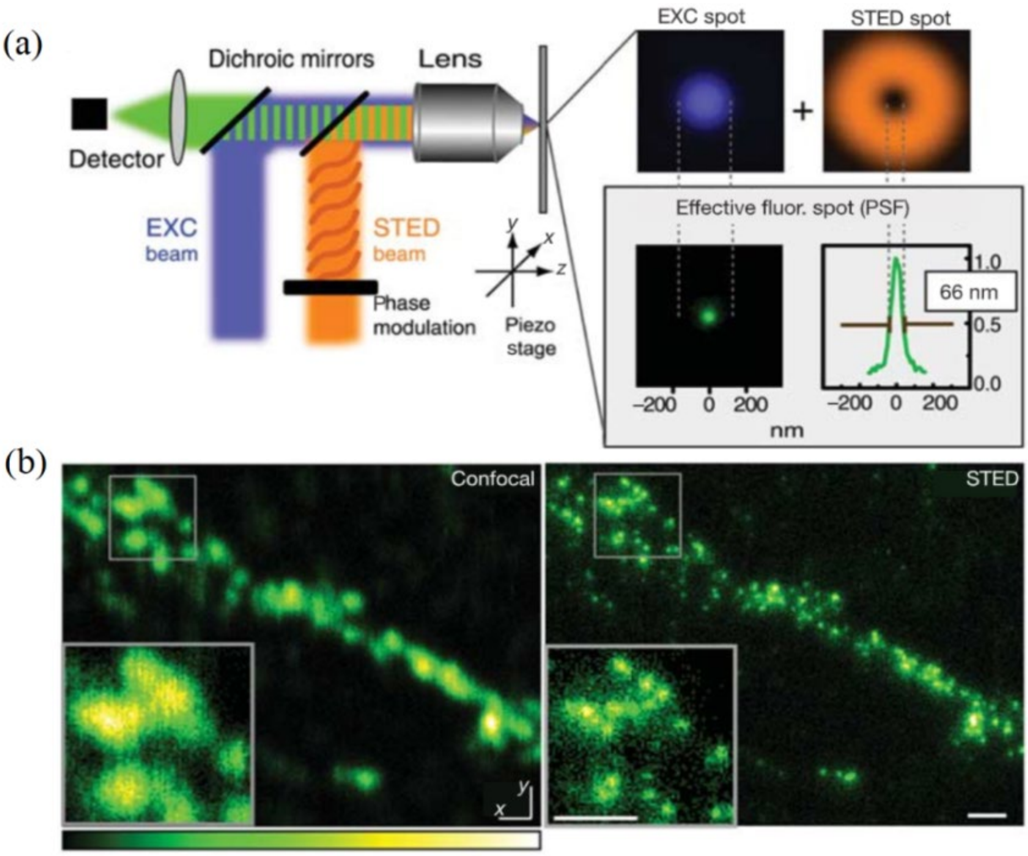

Figure 2.11. (a) Principles of operation of the STED microscopy and (b) Comparison of confocal (left)and STED (right) counterpart images of a labelled preparation reveals a significant increase in resolution by STED [9].

In another study, OVB was used in high-resolution, wide-field fluorescence microscopy technique which uses localized standing-wave surface plasmon polaritons at the OVB's central dark core to improve the 1D lateral resolution [111]. This technique was then developed to an all-optical technique excited by perfect OVBs with fractional topological charge [112]. An optical vortex array with multiple singularities can overcome the diffractive limit of far-field optical microscopy [113]. Such a fractional-charge OVB was also employed to significantly improve resolution of all-optical plasmonic structured illumination microscopy (reaching resolution of sub-100-nm) [114]. Moreover, vector vortex beams with specific polarization profile have important application in microscopy and imaging technology [115].

2.4.2 Optical tweezers

The second group of applications of optical vortices is related with optical trapping and manipulation of objects which is very important for both fundamental research and promising applications of singular optics [6,11,14]. Optical tweezers use tightly focused beams of light to trap microscopic particles at or near the optical axis [116]. The fascinating natural structure of vortex optical fields can be applied as a new optical tools contributing to control over small particles away of the optical axis [6,11,15]. This was first demonstrated by Bazhenov, Soskin and Vasnetsov in 1992 [117]. Three years later, an un-polarized OVB was used to tweezing a small ceramic particle [10]. In this study, authors pointed out that the transfer of OAM from light to matter caused a mechanical force to trap and spin absorptive particles and the direction of spin can be reversed by changing the sign of the singularity of the used vortex beam. Since then, significant progress has been achieved in this field including increasing rotating speeds [118], 1000 fold manipulation distance [12], controlling exact moment of the beginning and stopping of particle rotation [119], trapping and rotating a group of particles [120] as depicted in Fig. 2.12. Very recently, it was shown that the manipulation and detection the rotation speed of particles can be done simultaneously using perfect vortex whose ring radius is independent of its topological charge [121].

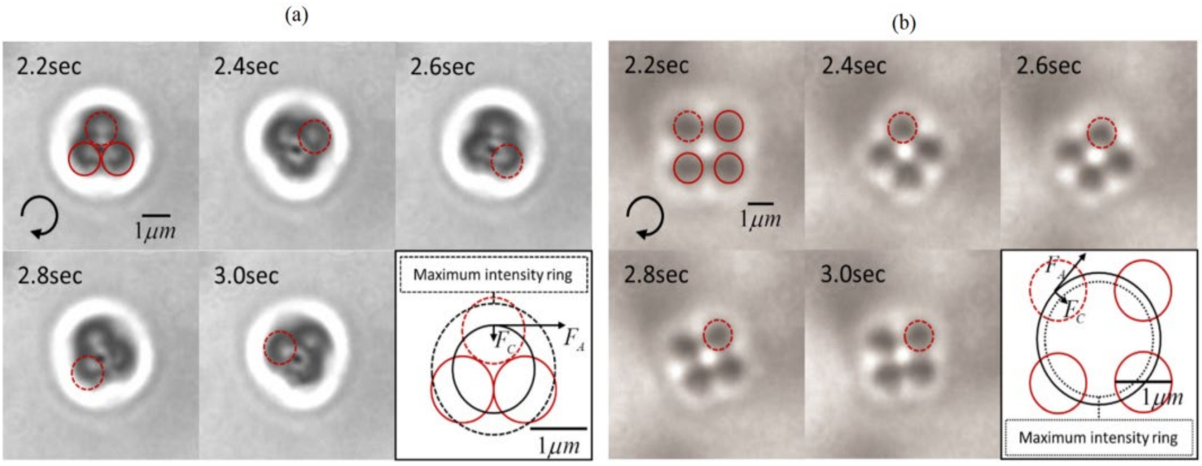

Figure 2.12. (a) Snapshots of recorded movement of a gold particle trimer and (b) a silica particle tetramer in the focused circularly polarized optical vortices [120]. The particles in the red dotted circles rotate clockwise.

Moreover, vortex beams combined with additional modes would add degrees of freedom for the improvement of optical tweezers [122,123]. For instance, some magneto-optical traps were constructed using a combination of LG TEM_{01} mode and TEM_{00} mode beams [122]. Laser-cooled rubidium atoms were trapped in a novel optical trap composing of the doughnut and plugging beams [123]. Depending on the spin angular momentum and OAM components in an optical vortex trap, a particle can be rotated either around its own axis or move around a circular orbit [124]. Counter-propagating vortex beams with changes $l = \pm 1$ allow trapping, binding and rotating of silicon nanowires. In addition, other studies have shown the convenience of using a novel OVB-carrying tweezers for more other purposes such as automated particle guiding, assembly, and sorting [125]. With the control of multi-singular OVBs, many new techniques were designed and applied to trap multiple particles [125–127], including the fractional optical OVB for optical tweezers [128]. Moreover, a femtosecond OVB tweezers which have special nonlinear properties can be used for a particle manipulation [129].

The usefulness of OVB-based optical tweezers was presented in photonics as well as biomedicine and chemistry. For example, proteins or bio-molecules could be trapped, driven and assembled to form a specific structure with such devices [14]. Manipulation of DNA molecules was demonstrated with use of a vortex-carrying tweezer. With tuning the corresponding vortex beam, it is possible to flexibly control the position, rotation, even condensation of the target DNA or other biomolecule for biomolecules assembling engineering purposes [14]. Specifically, OVB-based tweezers have provide great functionalities such as complicated surgery in single cell scale [130].

2.4.3 Optical communication

Optical communication is another important area that exploits the unique optical properties of OVBs [16,17]. Particularly, the OVB provides great possibilities in beam spatial mode-division multiplexing [131,132], extending data-rate transfer [133] of optical communication. The use of OAM multiplexing allows optical communication to break levels of Tbit/s [134,135], much larger than the traditional methods. The propagation of single as well as multiple OVBs in different external conditions with atmosphere, free-space has been investigated to prove the concept and show limits of feasible applications [136–138]. In this way, the capacity of the link and its data rate have been enhanced significantly for free-space communication [139,140] as well as underwater communication [141]. Recently, special fibre designs for vortex-multiplexing transmission has been exploited so that effective long-distance-fibre communication is practically proved [142]. It paves that way to reach Petabit-capacity level communication.

2.4.4 Quantum information

OAM-carrying OVBs have been applied on quantum domain a bit later than other fields but there are still plenty of great applications [18–20]. Individual photons carrying OAM (twisted photons) have presented practical possibilities of exploiting OAM entanglement in quantum information processing [18]. In particular, higher-dimensional orbital-angular-momentum-based quantum key distribution with mutually unbiased bases led to an increased information capacity as well as higher key generation rates per photon up to a dimension of $d = 4$ [143]. As a next step, the developed high-dimensional quantum key distribution cryptography results in the improvement of telecommunication security [144]. Besides that, OAM photonic qubits were generated for quantum memory purposes and this implementation provides an essential capability for future networks [145]. Due to carrying the inherent infinite dimension, the photon's OAM has been employed for benefiting higher-channel capacity communication [146,147]. The multiplexed quantum storage of rare-earth-based optical processor was presented for a highly reliable memory of 51 spatial modes [146]. The OAM has the potential for encoding a photon in a high-dimensional space, enabling the realization of quantum storage through the Raman protocol in a cold atomic ensemble [147]. The combination of high-dimensional OAM entanglement and digital spiral imaging was also successfully used for probing and identifying pure phase objects [148]. In addition, quantum entanglement between spin and orbital angular momentums made quantum communication benefited to aspects of technical control as for quantum teleportation [149]; capacity and speed [150]. Moreover, entanglement beating using vector vortex beams with SAM-OAM coupling states for propagation in free-space was presented recently [151].

2.4.5 Laser micromachining OVBs

Optical micro-machining is one of the newest areas of applications of OVBs [6,21]. Although vortex-based optical machining devices are not as powerful as those using Gaussian beam, they have more advantages in fabrications of special structures [152]. Potential of OVBs shows numerous special patterns on metal surfaces produced directly under either perpendicular OVB illuminations [153] or with varying incidence angles [152] or different states of polarizations [154]. Taking advantages of nano-photonics technology and advanced materials, nano-scale OVBs enable the ease of manufacturing of nano-size structures such as chiral nanoneedles [155] [156], helically nano-structured surface [157], silicon needles [158]. Examples of silicon needle fabrication are presented in Fig. 2.13, in which, the additional illumination allows increasing the height of the needle. Specifically, high-power combined light beams between OVBs and femtosecond laser allow creating sophisticated bulk devices such as micro-pipes having unique properties [159]. Interestingly, the focusing OVBs have recently studied in biomedicine as an optical knife for corneal dissection [160]. This vortex-based approach promised a simple, versatile, and cost-effective way of improving the precision of refractive surgery while reducing bubble formation and pressure-related mechanical side effect.

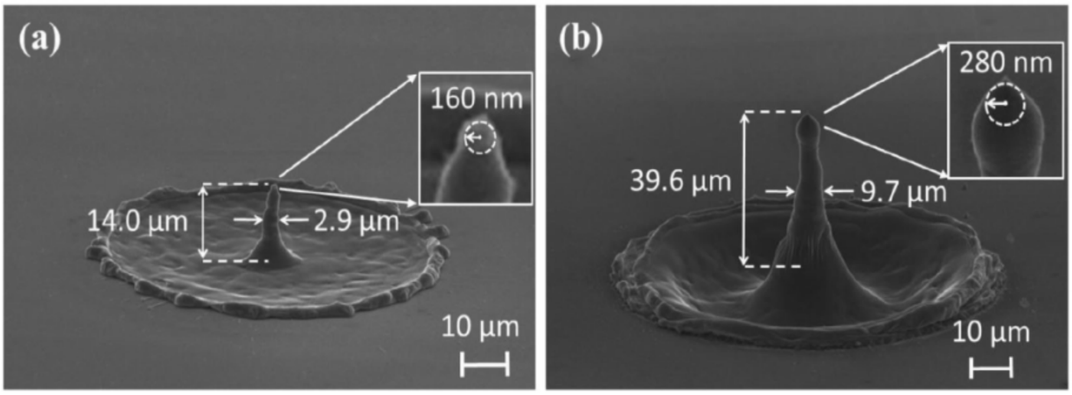

Figure 2.13. (a) Silicon needle fabricated by single shot irradiation of silicon wafer with picosecond vortex pulse with energy of 0.6 mJ. The inset shows the magnified silicon needle tip. (b) Silicon needle fabricated by the subsequent irradiation of additional 11 vortex pulses [158].

2.4.6 Astronomy

Since the discovery of OAM, a significant progress of study on photon orbital angular momentum has been achieved and in 2002 a new developed interferometric method allows a straightforward measurement of the OAM of individual photons in the laboratory [161]. This inspired the introduction of OAM into astronomy. One year later, Martin Harwit quantitatively described astrophysical processes of photon OAM as well as introduced a range of astrophysical application emerged related to photon scattering and vortex generation in the environments surrounding energetic sources, e.g., masers, pulsars, and quasars [162]. One of the greatest astronomical application of OVBs is the optical vortex coronagraph instrument which enables imaging of very faint objects near very bright objects which would normally be obscured by glare. In particular, extrasolar planets near their host star as seen from Earth or space telescopes in Earth's solar system. The optical vortex coronagraph was designed [22] and experimentally demonstrated [23] for the first time by Swartzlander's group during years 2005 - 2006. The operating principle of this instrument can be understood in a simple way that the light of a parent star will be blocked, while keeping the light from nearby but dimmer exoplanets. This coronagraph instrument has significantly contributed to many breakthroughs in astronomical demonstration [163–165]. In particular, a team from NASAs Jet Propulsion Laboratory demonstrated that the integration of a vortex coronagraph into a small telescopes allows directly image planets [165]. This was done by imaging the previously imaged HR 8799 planets with just a 1.5 m portion of the 5 meter Hale Telescope and the result is depicted in Fig. 2.14.

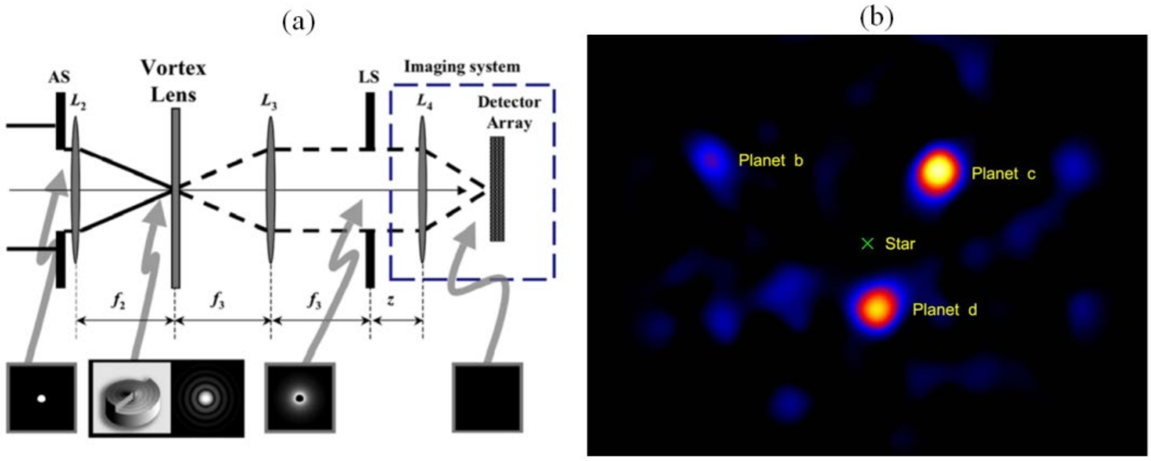

Figure 2.14. (a) Schematic of an optical vortex coronagraph with aperture stop (AS), vortex lens, imaging lenses, Lyot stop (LS), and camera. Numerically generated images depict the expected profiles for an on-axis point source at infinite [163]. (b) Direct image of exoplanets around the star HR8799 using a vortex coronograph on a 1.5m portion of the Hale telescope (integrated with vortex coronagraph) [165].

Along with the development and achievement of these coronagraph devices with use of scalar vortex masks, vectorial vortex masks have been also employed in coronagraphs for accommodating both high dynamic and high angular resolution imaging of faint sources around bright objects [166,167]. Recently, with a reconfigurable multiple vortex phase mask made of a liquid crystal thin film, high contrast imaging technique using multi-vortices enable to dim multiple sources of light. As a result, it gives the possibility to image planets around multi-star systems.

2.4.7 Metrology

In addition to particle manipulation, OAM-matter interaction turned out to be useful in metrology. Here, the OAM of OVBs interacts with mechanical-momentum of measurement objects which allows detecting motions of the object [168–170] motions. In particular, it is possible to measure both translational and rotational displacement using phase singularities in the complex signal generated by a Laguerre-Gauss filter operation [168]. By analyzing the OAM of the light scattered from a spinning object, we can observe the multiplicative enhancement of the frequency shift which allows a remote detection of rotating bodies in both terrestrial and astronomical settings [169]. The lateral motion of an object in an arbitrary direction can be detected by analyzing the change in OAM of a tilted light beam eclipsed by the tested object, without object image reconstruction [170].

OAM-based complex spectrum-based system was a powerful tool to measure object parameters like its relative shape and position, for instance, detection of the opening angle and orientation of a sector-shaped object [171]. In addition, speckle patterns generated by illuminating different rough surfaces with an optical vortex allows surface roughness measurements [172]. With the development in nanophotonics and nanofabrication, deeper researches on OAM-carrying OVBs are required for higher precisions (nano-scale) of metrology techniques.

Until now there have been various unexplored potential applications of OVBs in many fields of science and technology. It seems that there is still space for researches, hopefully resulting in discovery of new spectacular applications.

2.5 Summary

In this chapter, the fundamental theory of optical vortex beams was presented. Their novel optical properties i.e. doughnut-like intensity distribution, phase singularity, topological charge and orbital angular momentum were discussed in detail. Typical OVB verification techniques such as interference configuration, astigmatic transformation, and diffractive optics were also briefly introduced. In Addition, standard approaches for reliable OVB generation on basis of conventional phase components and vortex fiber designs were presented. Finally, I summarized various promising applications based on unique and fascinating OVB fields which would further have more great contribution to science and technology.

Chapter 3. Nanostructured GRIN vortex phase masks

The present chapter concerns mainly the novel concept and realization of nanostructured gradient index vortex phase masks (nVPM) whose dimensions reach tens of micrometers [57,62]. Such a phase component comprises of thousands of parallel nano-rods made of two different types of glasses with high and low refractive indices. Since the components are nano-sized, the operation principle of the binary nVPMs is explained by Maxell-Garnett effective medium theory (EMT) [173] in section 3.2. Those individual rods are spatially arranged following a designed pattern which is determined and optimized using simulated annealing method (SAM) [174,175] as discussed in detail in section 3.3. Then selections of materials for production of of nVPMs are presented in section 3.4. Section 3.5 is devoted to a description of fabrication and development of nVPMs exploiting stack-and-draw technique. This method was conventionally used for fabrication of photonic crystal fiber and initially developed for realization of nano-structrured gradient index microlens done by F. Hudelist [52]. The in-house-developed materials for nVPM fabrication are also introduced in detail.

3.1 Concept of gradient index vortex phase masks

Micro-optical phase elements are an important part of optical systems that perform collimation, focusing, and more-general phase corrections of light beams. The main principle of operation of all passive vortex converters such as geometric phase plates is directly imposing a helical phase structure onto incident waves. The incident waves are usually fundamental light beams: plane wave or Gaussian beam. The most well-known geometric vortex converter is a spiral phase plate (SPP) as aforementioned in the previous chapter. Recently, a new type of passive vortex convertors with flat parallel surfaces named nanostructured GRIN vortex phase mask (nVPM) was presented for the first time by our group [57] in 2017. Research results of our comprehensive studies of such masks are reported in [62]. The conventional SPPs and nVPMs share many similar properties but our masks have several advantages in comparison to the SPP type. Our masks have both flat and parallel facets and its functionality is defined by its internal structure. Those make them not dependent on refractive index of the surrounding media. Cost of mass production is minute in comparison to SPPs. Once the nanostructured fiber is drawn, thousands of elements can be produced from it by cutting the fiber and mask polishing.

In general, the generation of optical vortices based on illuminating geometrical mode converters requires the total azimuthal phase shift to be of multiplicity of 2π: $\Delta\varphi = 2\pi l$, with topological charge l = 1, 2,…being integer values. Such an imposition of spatial phase modulation onto the beams could be achieved by helical variation of one of two parameters: the mask thickness (as conventional SPPs) or its refractive index distribution (as the novel nGRIN VPMs proposed in this dissertation). The main difference between those two types is the origin of phase change as depicted in Fig. 3.1.

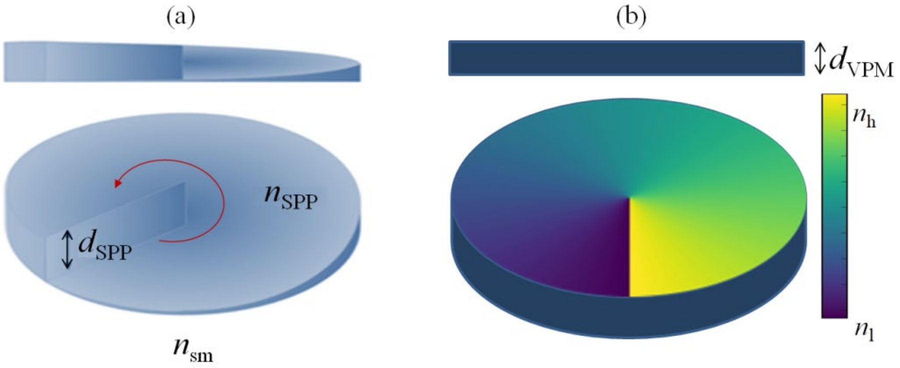

Figure 3.1 Concepts of the SPP with linear change of its thickness (a) and the VPM with linear change of refractive index (b) following azimuthal angle.

In case of SPP type shown in Fig. 3.1(a), the mask that is made of one optical material (constant refractive index n_{SPP} inside whole structure) has one surface of helical shape. Consequently, for a certain operation wavelength λ_0, the output OVB has phase modulation achieved by azimuthal variation of local mask's thickness d_{SPP}. The thickness can be calculated from the below formula:

$$\Delta\varphi = \frac{2\pi d_{\mathrm{SPP}}}{\lambda}(n_{\mathrm{SPP}} - n_{\mathrm{sm}}) = 2\pi l, \tag{3.1}$$

where n_{sm} denotes the refractive index of the medium surrounding the SPP. Typically, the SPPs are operated in the air, for that $n_{\mathrm{sm}} = n_{\mathrm{air}} = 1$. For the SPP designed for given wavelength in case of immersion, condition (3.1) will not be satisfied anymore and we have to make the new SPP. Thus, optical performances of SPPs are strongly affected by surrounding media which restricts the variety of its applications.

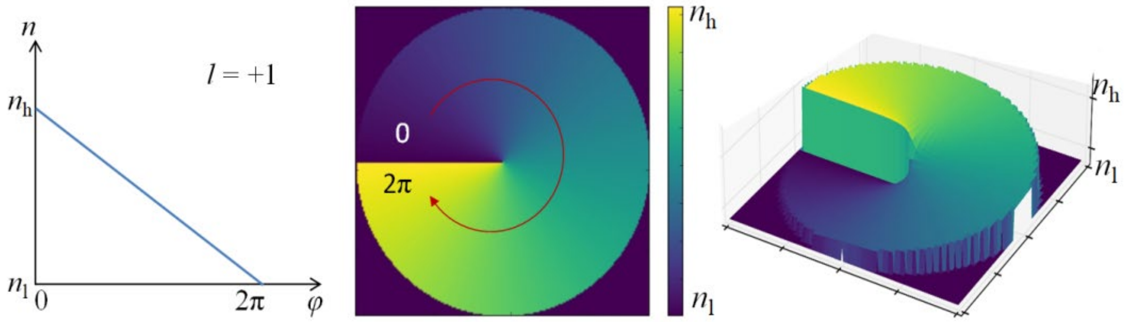

Figure 3.2 Linear refractive index change respect to azimuthal angle of ideal continuous VPMs for topological charge l = +1. This figure is based on [57].

In contrast to SPPs, our continuous GRIN VPM (see Fig. 3.1(b)) relies on the refractive index gradient of the mask. The concept of this GRIN vortex mask is its material refractive index changing linearly with azimuth angle φ as presented in Fig. 3.2. However, it is advantageous because the thickness d_{VPM} of the mask is the same for all points on its surfaces (d_{VPM} = constant). The refractive index distribution is described by the following formula:

$$n(\varphi) = n_{\mathrm{l}} + \frac{\varphi \Delta n}{2\pi}, \tag{3.2}$$

where n_{l} is the lowest refractive index value, Δn denotes the difference between the highest and the lowest refractive index values ($\Delta n = n_{\mathrm{h}} - n_{\mathrm{l}}$). As a result, for a certain input wavelength λ_0, the desired angular phase variation is engendered by azimuthally continuous refractive index gradient, which acquires the total phase shift of multiplicity of 2π:

$$\Delta\varphi_{\mathrm{VPM}} = \frac{2\pi d}{\lambda}(n_{\mathrm{h}} - n_{\mathrm{l}}) = 2\pi l. \tag{3.3}$$

From relation describing phase step (see Eq. 3.3), angular phase modulation created by our VPMs results from refractive index difference of the mask's materials and does not depend on the refractive index of the external media. Therefore, it can be immersed in any transparent external media and the converter's performance will be intact.

Those unique properties broaden flexibility and scope of applications of the mask in comparison to the classic SPP type. In particular, the constant thickness means VPMs have planar surfaces which allow easy integrations with other optical devices or standard optical fibers for a compact and robust optical system. Moreover, as aforementioned, the phase shift value generated by our GRIN VPMs is not influenced by surrounding media. Thereby it can be advantageous to use the same VPMs for applications in which immersion in various media is required.

Due to the current technological limitations, the realization of azimuthal refractive index profile in a continuous solid medium is a big challenge. To overcome this problem, the binary nanostructurization technique was exploited to create phase optical components. It allows obtaining almost the same optical performance as an ideal continuous gradient index mask. In this way, the concept of nanostructured GRIN VPMs (nVPMs) was proposed [57]. Its vortex binary-structure constitute of thousands of spatially arranged rods whose diameters are much smaller than operating wavelengths (nano-scale). The schematic of the nVPM and its corresponding effective refractive index profile is presented in Fig. 3.3. In our design of the mask we used two types of glasses [57,62] which results in binary structure of the mask. Among many properties of the used glasses, the most important one is their refractive index and absorption spectrum. Similar structure could be also obtained using more than two types of glass material for sub-wavelength rods. However, this method would make assembly and fabrication processes significantly more complicated without much gain in quality and optical performance of realized nanostructured components [52,57]. The binary approach is the simplest implementation of the whole fabrication process.

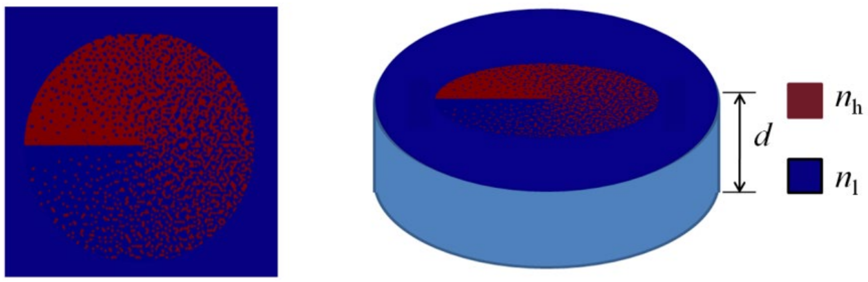

Figure 3.3 The schematic of a nanostructured gradient index vortex phase mask: (a) cross-section and (b) 3D component.

The principle of operation of such a component can be described with Effective medium theory (EMT) [173,176] which is a fundamental approximation for nanostructurization technology which will be discussed in detail in next section. According to this theory when the boundary conditions are fulfilled that nano-rod diameter in drawn structure are sufficiently smaller than operating wavelengths. As a result, the whole structure of nVPMs will act as an effective continuous medium. That means its effective refractive index profile mimics a continuous change with respect to azimuthal angle as shown in Fig. 3.2. In addition, the VPM is a scalar vortex generator and does not affect the polarization of the propagating beam. It is because the VPM is made of isotropic glass and its fabrication process does not produce any internal strain in the structure.

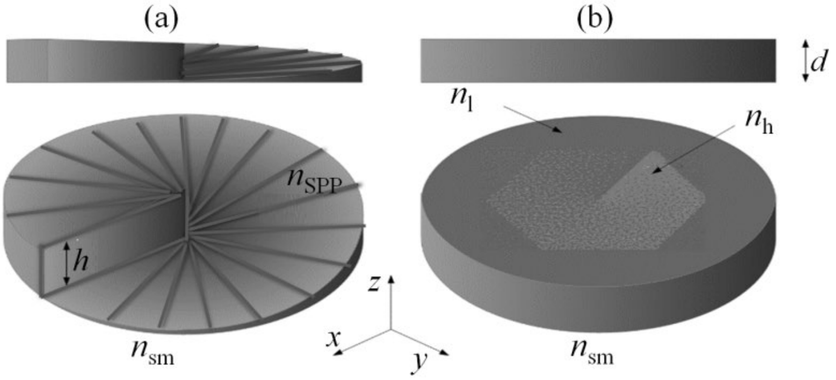

Figure 3.4 Schematic comparisons between realized step-like SPPs (a) and nanostructured gradient index vortex phase masks (b). This figure is based on [61]

In realization, the conventional transmission SPP type as discussed in chapter 2, has discrete, step-like surface profile that limits a proper representation of ideal, continuous profile of helical phase structure (see Fig. 3.4(a)). Especially as from Eq. 3.1, due to the high refractive index contrast between the plate material and air e.g. for typical BK7 glass it equals 0.5 at 1.55 μm [53], the step height of a single charge SPP should be very small c.a. twice the wavelength, which is very difficult to make with high precision. On the other hand, performance of an nVPM depicted in Fig. 3.4(b) is defined by optical properties of constituting two glass materials. The nVPM approach offers an additional degree of freedom for altering material refractive index difference in order to obtain optimized nVPM with desired charge for practically feasible thickness.

3.2 Effective medium theory for binary medium

As mentioned in the previous section our binary nano-structure is described by using an effective medium theory (EMT) [173,176]. In this section, a brief theory looking for effective permittivity $\varepsilon_{\mathrm{eff}}$, consequently effective refractive index n_{eff}, of a binary dielectric medium is introduced. At first let's assume that a binary-structured optical element constructs of numerous small sub-regions made of two different glass materials and each has its own parameters such as refractive index. Its main idea is that under the boundary condition when the size of those sub-regions is sufficiently small than the whole element will act as a continuous effective medium.

In this dissertation, all developed optical microelements are composed of discrete nano-sized diameters rods parallel to each other. Feature sizes (diameter) of such rods are much smaller than the operating wavelength of the transmission light which satisfies the boundary condition of EMT. That means, the light would not see the individual rods, it would instead see the whole structure as a continuous gradient index medium following a mixing rule described by the Maxwell-Garnett formula [52,173,176]. This mixing-formula gives an effective permittivity of the mixed medium of sub-wavelength rods in terms of the permittivity and volume fractions of the individual rods.

Originally the Maxwell-Garnet formula has been derived for a dielectric mixture medium. In an isotropic medium, spherical inclusions having radius *r and* permittivity ε_{i} are distributed with uniformly on average in the host medium of permittivity ε_{h}. For that medium, the relative effective permittivity $\varepsilon_{\mathrm{eff}}$ could be defined by the following equation [173,176]:

$$\langle \mathrm{D} \rangle = \varepsilon_{\mathrm{eff}} \varepsilon_0 \langle E \rangle, \tag{3.4}$$

where ε_0 denotes the vacuum permittivity; $\langle E \rangle$ and $\langle \mathrm{D} \rangle$ describe volume averages of the electric field E and the electric displacement D, respectively.

The volume fraction of inclusions is *f*. The effective permittivity of such a medium can be computed directly with the Maxwell Garnett mixing formula. This approximation given by first order of Taylor expansion can be done with $\varepsilon_{\mathrm{i}} - \varepsilon_{\mathrm{h}} \ll 1$.

$$\varepsilon_{\mathrm{MG}} = \varepsilon_h \frac{\varepsilon_h + \frac{1+2f}{3}(\varepsilon_i - \varepsilon_h)}{\varepsilon_h + \frac{1-f}{3}(\varepsilon_i - \varepsilon_h)} = \varepsilon_h + 3f\varepsilon_h \frac{\varepsilon_i - \varepsilon_h}{\varepsilon_i + 2\varepsilon_h - f(\varepsilon_i - \varepsilon_h)}. \tag{3.5}$$

To derive a generalization formula of effective permittivity for a complex medium, we consider the problem in the case of inclusions being uniformly distributed and similarly oriented ellipsoids. The detailed solution of this problem is described in [176] and it gives the result of conventional generalized Maxwell Garnett mixing formula:

$$\begin{aligned}(\varepsilon_{\mathrm{MG}})_p &= \varepsilon_h \frac{1 + (1 - \nu_p) f \frac{\varepsilon_i - \varepsilon_h}{\varepsilon_h + \nu_p(\varepsilon_i - \varepsilon_h)}}{1 - \nu_p f \frac{\varepsilon_i - \varepsilon_h}{\varepsilon_h + \nu_p(\varepsilon_i - \varepsilon_h)}}, \qquad p = x, y, z \\ &= \varepsilon_h \frac{\varepsilon_h + [\nu_p(1-f) + f](\varepsilon_i - \varepsilon_h)}{\varepsilon_h + \nu_p(1-f)(\varepsilon_i - \varepsilon_h)},\end{aligned} \tag{3.6}$$

where the parameters ν_p $(0 < \nu_p < 1, \nu_x + \nu_y + \nu_z = 1)$ are the ellipsoid depolarization factors whose analytical formula is shown in [173]. The formula in Eq. (3.6) is a general form applied for both isotropic and anisotropic media. It can be easy to derive the Maxwell Garnett mixing formula for only isotropic composites (Eq. 3.5) from the generalized formula Eq. 3.6 by making the substitution ν_p = 1⁄3. In addition, the generalized Maxwell Garnett mixing formula is used more commonly due to its convenience in solving different problems and its nice mathematical properties shown in limitation cases. For instance, it is great that in the limiting case of a medium with $\nu_p = 0$ the formula in Eq. (3.6) gives exact results in which $(\varepsilon_{\mathrm{MG}})_p$ are always numerical values inside the Wiener boundaries [176]. In here the effective permittivity is approximated by the volume average of the permittivity of the inclusions.

$$(\varepsilon_{\mathrm{MG}})_p = f\varepsilon_i + (1-f)\varepsilon_h \approx \langle \varepsilon(\mathbf{r}) \rangle \tag{3.7}$$

In the case when $\nu_x = \nu_y \rightarrow 1/2$ and $\nu_z \rightarrow 0$, the inclusions become infinite circular cylinders. The large medium is now in a form of an infinite cylinder containing many parallel cylindrical inclusions of much smaller radius. This becomes similar to the problem considered in the scope of this dissertation.

Applying this to our nanostructured vortex phase components, the effective permittivity distribution on cross-section of nVPMs would be calculated using the general Maxwell Garnett mixing formula in Eq. (3.6). Since all the rods in the constructed component are parallel and align along the beam propagation direction, so the 2D refractive index profile in the xy plane is invariant along z axis. Additionally, individual glass rods of the binary structure have a refractive index difference smaller than 0.025. Thus, the simplified Maxwell Garnett mixing formula (Eq. 3.5) can be also used. In an assumption of zero absorption of the constituent glasses, the effective refractive index at a certain point in cross-sectional pattern can be calculated by spatial average of across immediate neighboring points. In this way, entire sub-wavelength rod structure, while discrete, will behave as a continuous effective medium. According to the EMT boundary condition, the rods diameter should be smaller than $\lambda/2\pi$ [173]. Some recent experimental works reported that EMT still valid for the condition of the feature size of $\lambda/5$ [52,56]. In an our very recent study, we proved that by controlling temperature during fabrication process to obtain a suitable diffusion effect, the nanostructured components still can work effectively exceeding the EMT boundary condition with the diameter of glass rods of $\lambda/0.658$ [177]. In this work, the individual rods in all considered nVPMs have diameters are much smaller than this value ($\lambda/0.658$).

3.3 Simulated annealing approximations for structured design

As mentioned in previous section, the considered nGRIN VPMs are structured from discrete parallel nano-rods made of two types of glasses having different refractive indices. Those refractive index values correspond to the maximum and minimum values in the gradient structure. Here the binary structures of the nVPMs are not distributed randomly; instead, all the rods should be arranged following a specific distribution such that the whole structure would have an effective refractive index profile imitating the ideal azimuthally continuous gradient refractive index distribution. In other words, the effective refractive index profile of the binary nanostructured components should be the closest one to the designed target. It means the distribution of rods decided the effective refractive index profile of the nVPM, consequently, its optical performance. However, it is not possible to directly calculate the distribution of the rod pattern for the desired refractive index profile. There are thousands of related variables and with computational power of single workstation the result cannot be obtained in realistic time frame. Therefore, in this work, the mixed nanorod distribution of nVPMs will be determined and optimized by the usage of Simulated annealing method (SAM) [174,175,178] which can give a good approximation to the optimal solution of a given cost function. For each problem, the cost function is selected differently for the optimization purpose.

The SAM which belongs to a class of Monte Carlo Algorithms performs well in optimization problems a large number of degrees of freedom [175]. The SAM is a stochastic optimization procedure that may lead to a stationary state (the global minimum). In essence this procedure resembles cooling a crystal down slowly such that defects and other lattice impurities can heal out. As a result, a pure crystalline structure is achieved at low temperature. For a particular physical system, each state (S) of it has a specific energy E described by a Hamiltonian E = H(S). This is called the cost function (energy function) for the optimization problem. The goal of solving this problem is to minimize the cost function which can have local minima in addition to the global minimum. This SAM approximation gives the advantage of finding the global minimum while the local minima are more likely to be avoided. Figure 3.5 presents the schematic describing repeated iterations of SAM for optimization of a physical system. Each proposed configuration change simply flips a randomly chosen distribution of the system into a new state [178].

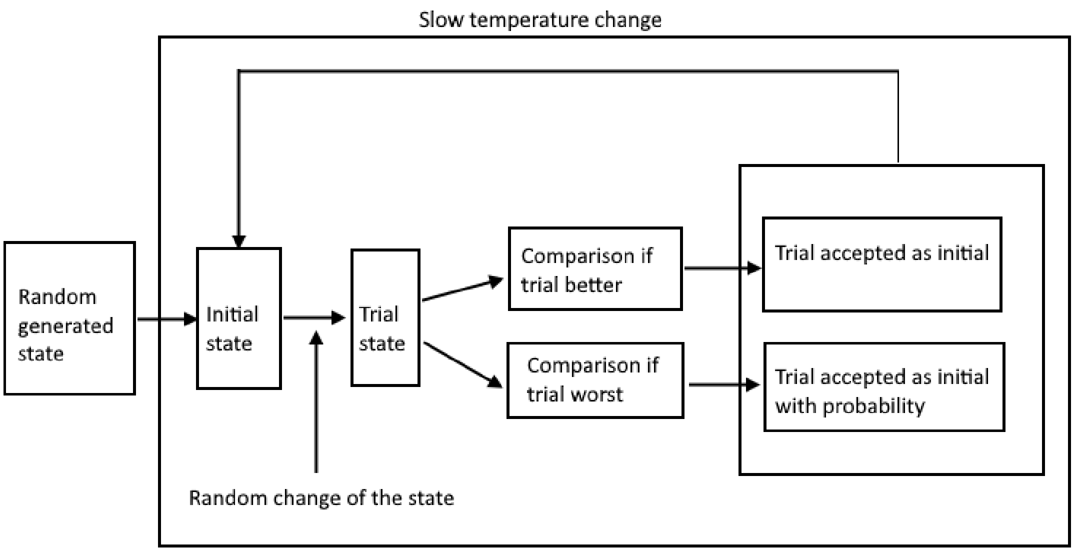

Figure 3.5 Schematic of simulated annealing method for solving optimization problem.

The procedure starts with a random selection of a state (S_0) of the system. Then a random trial state (S_1) is generated for consideration. There are two possibilities for this stochastic process. If $H(S_1) \leq H(S_0)$, the trial state (S_1) is accepted as a subsequent state for next iteration ($S_0 := S_1$). If $H(S_1) > H(S_0)$, the acceptance probability of the new state is determined by Metropolis transition rate [179]:

$$t(S_0 \rightarrow S_1') = \exp\left[-\frac{\Delta H}{kT}\right] = \exp\left[-\frac{H(S_1') - H(S_0)}{kT}\right], \tag{3.8}$$

where parameters k and T introduce Boltzman's constant and temperature, respectively. In the next iteration, the new state (S_1) is considered as the initial one for new iterations and finding new suitable states. In this method, the calculations begin with a random distribution system at high temperature T and end with equilibrium of the system at the low temperature ($T \rightarrow 0$). It is noticed that during the whole procedure, the temperature which allows jumps over energy barriers between various configurations should reduce gradually. Otherwise the state configuration gets stuck and we cannot find the final perfect result. In principle, it is possible to find a global minimum of the cost function for a given finite problem but it may take infinite time. Therefore, a good approximation of the optimal solution provided an efficient cooling protocol is chosen [175].

In the case of our binary nanostructured GRIN VPM, it is comprised of thousands of parallel nano-rods characterized by two different refractive indices as aforementioned. In this way, the nano-rods distribution, consequently, the refractive index within the mask is invariant along z-axis. Therefore, the design and optimization problem here is a problem of only 2D distribution of nano-rods (refractive index) on the cross-section of the mask (XY plane). This problem is solved when the final refractive index distribution of the binary nanostructure similar to the target distribution in which the refractive index changes linearly with respect to the azimuthally angle.

It is noticed that the change of refractive index of individual rods makes certain change to the effective refractive index of the whole structure. Thereby each arrangement of nanorods producing a certain effective refractive index profile is considered as a state during the optimization process. Here effective refractive index of a particular area in the nanostructure $n_{\text{eff}}(x_i, y_j)$ is determined by a spatial average of the individual refractive indices of its neighborhood as in Eq. 3.7. The cost function $C(S)$ is selected in order to measure difference between the effective refractive index profile of the current refractive index distribution of the whole structure and the target distribution which is given as in following formula [178]:

$$C(S) = \sum_{i,j} \left| n_{\text{eff}}(x_i, y_j) - n_{\text{ideal}}(x_i, y_j) \right| \tag{3.11}$$

The optimization procedure starts with an initial state with a random distribution of refractive index in the structure (S_0). A new closed state is generated by randomly changing refractive index of one rod (S_1) and then it is compared to the target distribution. If the state S_1 is accepted, the initial state is substituted by the new state, if not old state remains. The first iteration is completed. This process will be repeated many times in which the accepted state in previous iteration is considered as the initial state in the following iteration. For each temperature, the number of steps is preferably greater than the number of rods in the structure. This ensures refractive index of each nanorod is changed at least one time for the same temperature. When the number of iterations is reached, the temperature will reduce and the whole process is repeated. The first step of the new process will starts with the accepted state from the last step of the previous process. When the temperature T is going to 0, the global minimum of the cost function is achieved. In order to obtain best possible solution, we have to increase the number of steps of temperature T and the number of trial distribution states tested at each temperature. A detail investigation in [178] showed that when increasing the number of temperature steps beyond 140 the cost function remains the same at the lowest value. The number of trial states generated for each temperature process beyond 200000 does not change the cost function at that temperature. In addition, the area over which the refractive index is averaged when compared to the ideal distribution is also in important factor considered for the successful of SAM. It influences how much effective refractive index changes when one rod is changed. A right selection of the area factor gives sufficiently accurate results while allowing rapid optimization of highly complex structures. The authors of ref. [178] also pointed that the lowest possible cost function was obtained for 0.99 length unit of the simulation.

The calculations for the nVPM in this work were performed for averaging area with radius changing from 0.1 to 1. The lowest cost function was obtained for 0.9 unit length refractive index averaging, 150 temperature steps and 20000 random states generated for each temperature step [178].

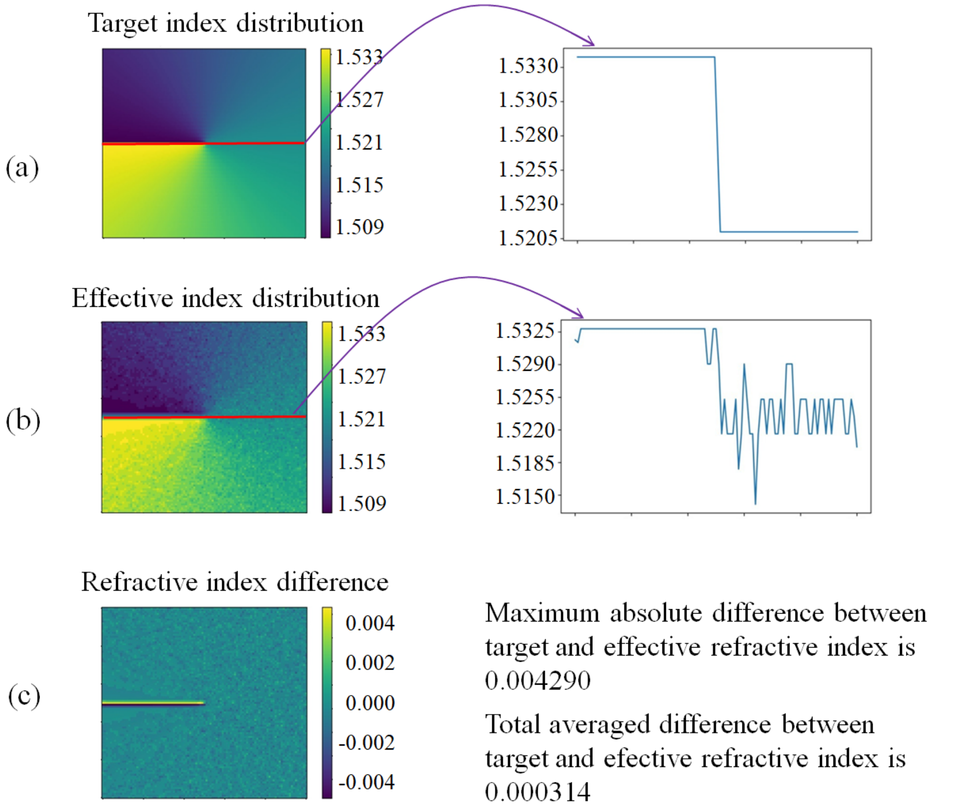

Figure 3.6 An example of calculated results using SAM method: (a) target index distribution; (b) final approximation by SAC method; (c) refractive index difference between (a) and (b).

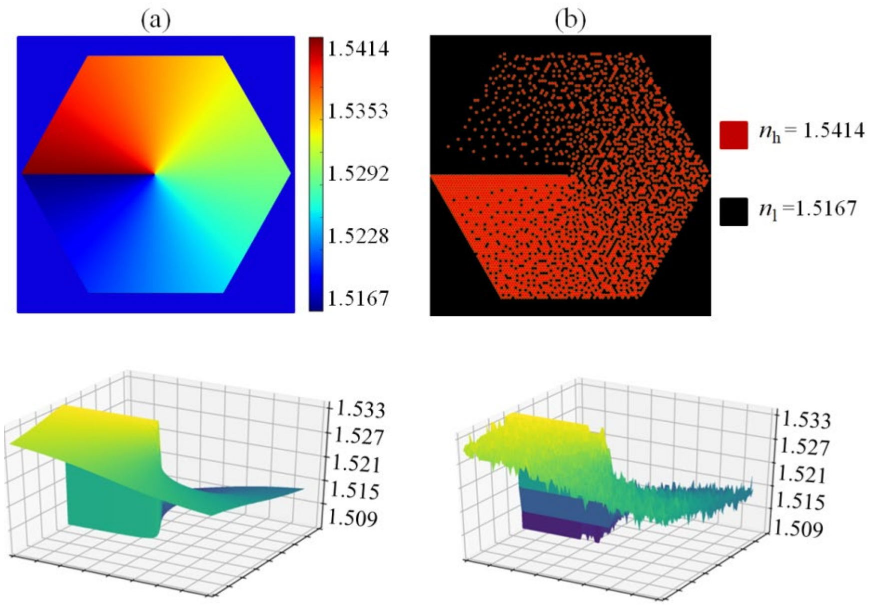

Figure 3.7 An example of final structure of nVPM used for fabrication (b) corresponding to the ideal continuous VPM (a) and their 3D plots of refractive index profile.

Figure 3.6 shows an example of results for nVPM structure's design and optimization using SAM. The first row (a) depicts a map of ideal continuous refractive index distribution and index profile of its horizontally center line. Basing on this target distribution, simulated annealing algorithms allow calculation of the effective refractive index distribution for the optimized nanostructured pattern (b). Importantly, in the output of this calculation, we obtained a refractive index difference map between these distributions and values which calculated from the used cost function (Fig. 3.6(c)). In particular, the maximum absolute difference is the biggest difference in single rod size area between target and final distributions. The total averaged difference value is the sum of differences for each rod sized area divided by the number of rods in effect of our cost function. As discussed above, it maybe takes infinite times to obtain the global minimum solution, so there is no guarantee to find a global minimum in the strict sense. Therefore, to achieve the best approximation, we have to run the SAM calculation many times and consider all of the final results for the selection of the good pattern for fabrication. A good optimized structure should have low values of a total averaged index difference and a maximum absolute difference. Spontaneously, it should also have similar index differences in all points across the structure.

After selecting the final designed binary vortex mask with the best optimization, we reshape it into a hexagonal as depicted in Fig 3.7. In principle any shape of the aperture of the final elements can be obtained with manual assembly. In practice, the hexagonal lattice was selected due to the technical requirement for the fabrication of the mask. In this way, the positions of individual rods in the structured pattern will self-maintained throughout the whole fabrication process.

3.4 Materials

In the practice, the designed pattern of nanostructured GRIN vortex phase masks can be realized by employing a modified stack-and-draw technique. To begin with, the selection of a suitable pair of glass materials is crucial due to two main reasons. Firstly, their refractive index contrast should be constant for all wavelengths in the considered range. Secondly, they have to fulfill the technological requirements of the fabrication process in which their mechanical and thermal properties have to be matched to combine together in thermal process in the drawing tower. The glass used need to have temperate kept in range between curvature and sphere creation to maintain proper viscosity for drawing. Moreover, their viscosities must be similar; otherwise there will be stresses and deformation in structure. Our previous studies on optical glasses used in stack-and-draw fabrication approach [178,180] showed that stable processes can be achieved if the difference for those main glass temperatures is below 50ºC. In addition, thermal expansion coefficient difference $\Delta\alpha$ of those glasses should not exceed the value of 8×10^{-7} K^{-1} [178,180]; otherwise the build-up of stress during cooling will cause cracks and warp of fabricated structures.

Therefore, it is necessary to chose glasses with good rheological properties and relevant expansion as well as thermal coefficients to ensure uniformity of the structure during drawing process and lack of internal tensions after the process accomplished. However, it is difficult to find such a kind of glass pairs from commercially available glasses. For this reason, we have developed a pair of boro-silicate glasses at our facility – Łukasiewicz Research Network – Institute of Microelectronics and Photonics (IMiF). The glass pair was designed and synthesized such that their properties satisfy the above-mentioned conditions. Those two in-house-made boro-silicate glasses are labeled NC21 and NC32 having lower and higher refractive index, respectively. Their chemical compositions are shown in Table 3.1 [178].

Glass label	SiO_2	B_2O_3	Al_2O_3	BaO	Li_2O	Na_2O	K_2O
NC-21	56.83	23.19	0.61	-	6.23	9.52	3.63
NC-32	54	21	0.5	5	5	8.5	3

Table 3.1. Chemical compositions of boro-silica glasses used for nVPM fabrication (mol%)

Table 3.2 shows the thermal-physical (rheological) properties of those fabricated glasses which were measured and reported in [178]. It can be seen that, this boro-silicate glass pair has an expansion coefficient difference of $\Delta\alpha = 0.3\times10^{-7}$ K^{-1} which is well below the given limit value mentioned above.

This small value allows the two soft glasses to be thermally processed together. During the structure drawing process in drawing towers, the glasses are kept inside the furnace with a temperature between the curvature and sphere points for both glasses as measured by the heating microscope. The measurements show that the difference in curvature temperature is very low ΔT_c=20°C and difference in sphere temperature ΔT_{kph} is only 5°C. Those differences are much smaller than for the NC21/NC34 glasses which were used to sucessfully develop nGRIN microlens recently [178]; correspondingly ΔT_c=50°C and ΔT_{kph} = 35°C. As a result, we obtained the uniform glass structure without deformations.

Glass paramaters	**NC-21**	**NC-32**
Refractive index *n* at wavelength of 633 nm	1.5243	1.5495
Thermal expansion coefficient α for 20÷300° C [10^{-7} K^{-1}]	86.6	86.9
Transition temperature $\mathbf{T_g}$ [°C] logη = 13.4	504.7	512.7
Dilatometric softening point **SP** [°C] logη = 11.0	540	547
Characteristic temperatures in Leitz heating microscope **T** [°C]:		
curvature $\mathbf{T_c}$ logη = 9.0	620	640
sphere $\mathbf{T_{kph}}$ logη = 6.0	725	720
hemisphere $\mathbf{T_{hs}}$ logη = 4.0	775	780
spreading $\mathbf{T_{spr}}$ logη = 2.0	860	860

Table 3.2. Physical and thermal parameters of NC-21 and NC32 glasses [180] [178] .

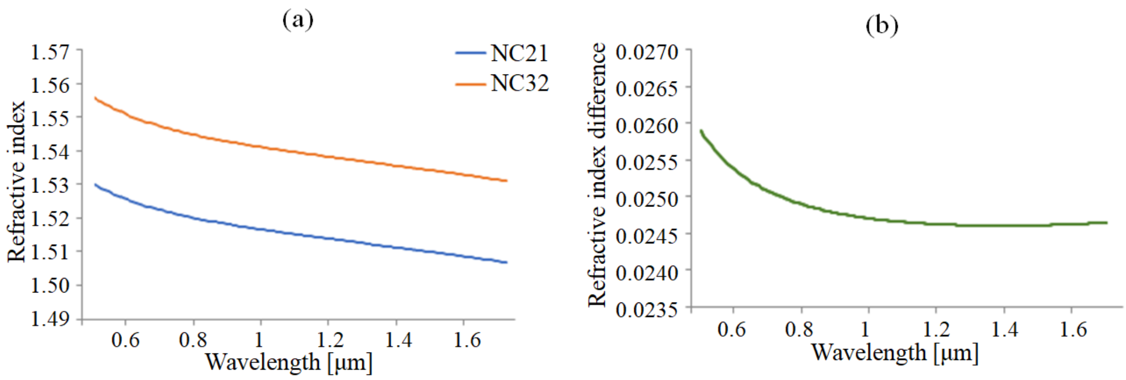

Figure 3.8 Refractive indices of two boro-silicate glasses (a) and their index contrast (b) on the range wavelength from 0.5 to 1.7 µm.

In Fig. 3.5(a), there is the wavelength dependence of refractive index of the two boro-silicate glasses for the wavelength range from 0.5 µm to 1.7 µm. Their refractive index difference is given in Fig 3.5(b). It can be seen that the refractive index different values are almost constant (~0.025) in the near infrared range between 0.8 µm and 1.6 µm. Specifically, at wavelength λ = 0.633 µm, the high refractive index glass has n_h = 1.5495 and the low refractive index glass has n_l = 1.5243. Those values are measured by mean of Michelson interferometer. In addition, both NC21 and NC32 glasses have high transmission in visible and near infrared range between 400 nm and 2100 nm. They also have relatively high laser induced damage threshold ≈1 J/cm^2 in femtosecond regime, typical for borosilicate glass [181]. This leads to the possibility of using this component for high power applications as laser material processing.

3.5 Fabrication

Over the last decade, from the first fabricated nanostructured GRIN element that was reported in [52], different kinds of components have been exploited, for instance, small GRIN micro lenses [52], large-diameter GRIN lens [53], elliptic gradient index microlenses [54,55], nGRIN axicons [56]. Those components made by a cost-effective nanostructurization technique have been exhibiting noticeable optical properties as mentioned in Chapter 1. In this work, the nanostructured vortex phase masks that are fabricated using the same technique will be discussed in detail as following.

In preparation for the fabrication process, beside the designed structure pattern used for assembling, it is necessary to calculate the thickness of the nVPM which is associated twith the topological charge value of generated optical vortex. Following Eq. 3.3, it can be seen that the phase shift realized in the mask strongly depends on the thickness of the masks. To generate a vortex beam with a specific topological charge l at a given wavelength λ_0, the thickness d of nVPMs can be determined as follows:

$$d = \frac{1}{\Delta n}\lambda l. \tag{3.12}$$

From this formula we deduce that for a high value of Δn we can have relatively low value of d which would lead to very thin vortex masks. Due to the technological limitations in cutting and polishing it is a challenging mask fabrication. Our current technique can only polish the nVPMs with thickness being not shorter than 15 µm. In the scope of this work, the used boro-silicate glasses that have small refractive index difference (~0.025). This ensures nVPM thickness in range of tens of micrometers which is feasible for production. Here, with the known refractive indices of the borosilicate glasses pair, we can theoretically calculate the dependence of the mask thickness on the operating wavelength. Fig. 3.9 below shows relations between nVPM thickness and wavelength for 2 specific values of topological charge $l = 1$ and $l = 2$.

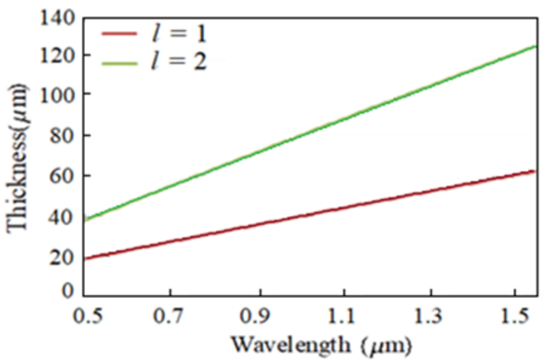

Figure 3.9 Theoretical calculations of the thicknesses of nVPMs for wavelength range 0.5 µm to 1.5 µm.

As aforementioned in section 3.3, the desired effective refractive index profile of nanostructured gradient index vortex phase masks will be achieved by a designed nano-rod pattern. That pattern comprises of thousands of nano-rods made of two boro-silicate glass materials. Such designed nVPMs with suitable predicted thicknesses are realized by using a cost-effective fabrication method, the modified stack-and-draw method [57,62]. This nanostructurization technique allows developing optical elements with truly continuous phase profiles with the diameter of tens of micrometer. By designing the rods arrangement, various refractive index profiles of the elements can be obtained for controlling the propagating light while the optical element surfaces remain completely flat. The unique fabrication capabilities of nanostructuring technique have been confirmed by demonstration of a number of nGRIN elements like nGRIN microlenses [52,65,182], elliptic lenses [54,55], axicons [56].

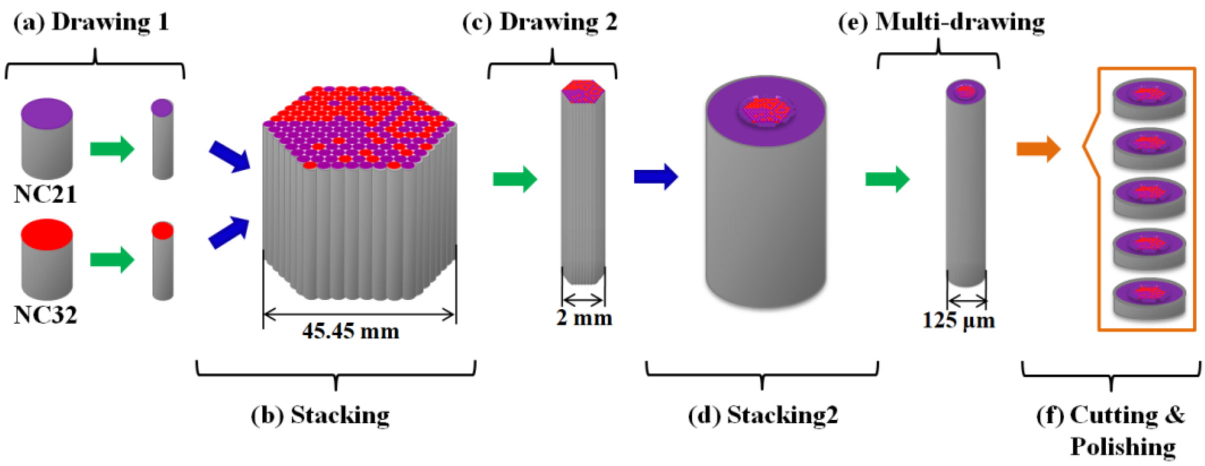

Figure 3.10 Schematic of the fabrication procedure of nVPMs with the use of a modified stack-and-draw technique.

In this section, the whole procedure of the fabrication of nVPMs utilizing modified stack-and-draw approach will be described in detail. This approach is conventionally employed for photonic crystal fiber development. For the fabrication of nanostructured component, the modified approach contains an additional step (last step) as depicted in the schematic in Fig. 3. 6. Firstly, we prepare two types of rods made of two borosilicate glasses with high and low refractive indices but similar rheological and thermal coefficients (Fig. 3.6(a)). Here, they are dawn into rods with small diameter of ~0.45 mm. They are then cut and cleaned carefully to be ready for the next step. The seconds step is manually stacking the initial perform from the two types of glass rods (Fig. 3.6(b)). The positions of individual rods must be exact following the designed pattern of hexagonal shape. As mentioned in previous section, the hexagonal shape is chosen due to the technical requirement for the fabrication of the masks. Moreover, the size of the drawn structure depends on the size of furnace in drawing tower. For drawing soft glasses, the used equipment only allows drawing the preform having the long diagonal of 50 mm. which limits the total number of rods used in stacking process. In this case with 0.45 mm rods, the preform is designed to have 101 rods on the long diagonal. As a result, the total number of rods used for whole vortex structure is 7651 rods. Such stacked preform is then drawn-down in the drawing tower to obtain a uniform hexagonal-cross-sectional rod with a dimension of ~2 mm on the longer diagonal (Fig. 3.6(c)). The temperature inside the furnace is kept between 600÷700°C during the whole drawing process. In the next step shown in Fig. 3.6(d), the drawn preform is put at the center of a glass tube which is made of the low refractive index boro-silicate glass NC21 to form an intermediate preform. The empty space between the drawn initial preform and the tube is filled by low refractive index rods prepared in the first step of the process. The outer glass tube and additional filling rods are for creating a cladding area surrounding the central vortex structure. In the fifth step, the intermediate preform is again drawn-down in the high temperature similar as in previous drawing step (Fig. 3.6(e)). In this step, the diameter of the structure is reduced in multiple thermal processes to the standard 125 µm diameter. Eventually, the final-structured fiber is cut into slices (Fig. 3.6(f)). Each slide is ground down to the desired thicknesses and then polished.

Fig. 3.11 shows sample images taken at different steps during fabrication process. Particularly, Fig. 3.11(a) presents the drawn structure from the first drawing process after stacking which was used to stack the intermediate preform. The image is captured under a high-resolution optical microscope. Figs. 3.11(b-d) are scanning electron microscope (SEM) images which verify the final structure of fabricated nVPM samples. Specifically, Fig. 3.11(b) shows the whole surface of a fabricated component containing the vortex structure at its center. It has an outer diameter of 125 µm which is compatible with the dimension of standard fibers. It is easy to see in Fig. 3.11(c) the magnified vortex structure having the longer diagonal of ~20 µm. In the higher magnification image for a part of the structure (Fig. 3.11(d)), we can see visible individual nano-rods (regions) in which the bright and dark regions represent high and low refractive index glass rods, respectively.

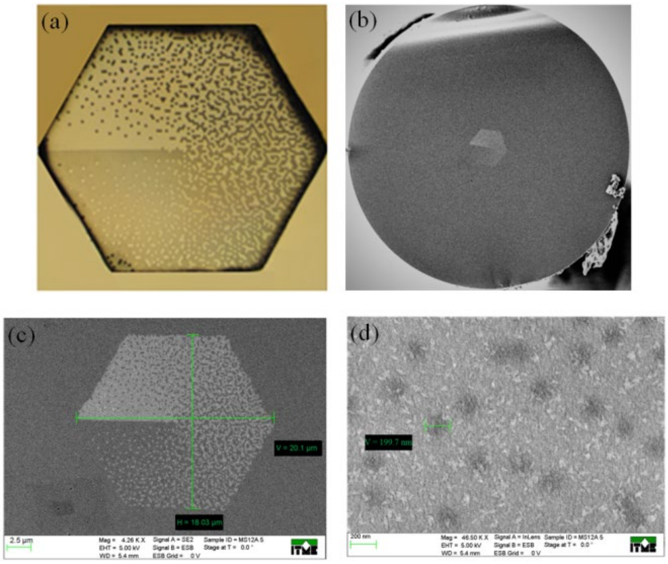

Figure 3.11 Fabricated nanostructured vortex mask: (a) microscope image of the drawn structure after the first-drawing step. (b-d) SEM images of the surface of a whole drawn element containing vortex structure (b); the vortex mask structure (c); and magnified part of vortex structure with visible individual nano-rods. Bright (dark) regions represent high (low) index glass (d).

The nVPM were designed as having the individual rod diameter of around 200 nm. To fulfill strictly EMT condition that the feature should be smaller than $\lambda/2\pi$, for 633 nm wavelength the use of nano-rods with 100 nm diameter is required. However, due to the material diffusion between neighboring rods during the fabrication processes, the EMT conditions are fulfilled for larger rod diameter, as in our case of $\lambda/3$, which is already sufficient to produce the desired continuous gradient index profile as we have shown recently [60]. In this paper, the success of this modified fabrication method was demonstrated for large diameter nanostructured GRIN microlenses. The combination of a nanostructurization and enhanced diffusion allowed for the increase of size of individual nanorods used in microlens structure beyond limits given by EMT. We can control the diffusion process by selecting a proper temperature and remaining drawing parameters. As a result, we obtain locally smooth changes in refractive index and total refractive index distribution close to designed parabolic profile.

3.6 Summary

In this chapter, the nanostructured gradient index vortex phase mask has been presented in detail from concept to realization. It has shown that the nVPM with diameter of 20 µm consists of thousands of spatial arranged sub-wavelength rods made of two different glasses characterized by high and low refractive indices. The glasses are in house made boro-silicate glasses (NC32/NC21) which has refractive index difference of ~0.025 for a long wavelength range from 0.8÷1.6 µm. The masks were fabricated using the modified stack-and-draw technique which allows controlling rods distribution easily, consequently, the refractive index azimuthal profile of the optical component. The rod distribution was determined and optimized by simulated annealing method utilizing a cost function which measures the difference between a target ideal refractive index distribution and the effective refractive index of the current nanorod distribution. The individual rods in the vortex structure have diameter of ~200 nm and with the material diffusion effect, the EMT boundary conditions are satisfied for the optical component. That means the nVPMs would perform as a continuous medium with an effective refractive index changing linearly with respect to azimuthal angle.

Chapter 4. Numerical study on generation of optical vortex beams with nanostructured gradient index vortex phase masks

This chapter is devoted to the theoretical study on the optical performance of nanostructured GRIN VPMs for the quality improvement of generated optical vortices, first reported in [61]. Numerical calculations are conducted to validate potential methods for development of gradient index vortex masks. In previously reported work done by Switkowski et. al [58], it can be seen that nVPMs suffer from the wave-guiding effects which lead to azimuthally non-uniform light intensity distribution in formed vortex beams. Motivation and study methodology of this work are presented in section 4.1. Then, section 4.2 introduces modelling technique used for these investigations. Here the fundamental of Fourier Transform-based Beam Propagation Method (BPM) employed for numerical simulations of beam propagation through the VPMs and then in external media is presented. In section 4.3, a new parameter called quality parameter Q is proposed for ease comparisons of uniformity of vortex intensity distribution. In the next part of research, I would focus on discussions of main results of this work regarding main factors for improving vortex quality in terms of intensity uniformity and phase distribution. Firstly, refractive index contrast by the used of different pair of glass materials is considered in section 4.4. Secondly, section 4.5 is devoted to the discussions on proposed non-linear azimuthal gradient index profiles of the VPM as a method to counteract light guiding effect. Finally, possibilities to use VPMs to generate vortices with high topological charge are investigated in section 4.6.

4.1 Motivation and methodology of the study

In Our previous study reported by Switkowski et al. [58], the proof-of-concept of vortex nanostructured phase mask was introduced. The presented nVPMs enables converting a Gaussian beam into an OVB with desired topological charge at a certain wavelength. The obtained vortices have nonuniform intensity profiles, which are shown in experiments as well as in theoretical calculations. This effect is depicted in Fig. 4.1 for VPM with thickness of 36 microns at wavelength of 890 nm.

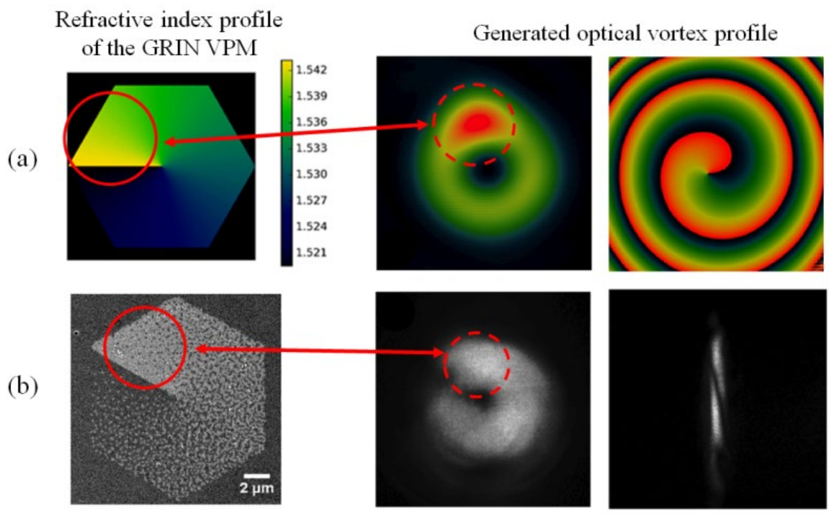

Figure 4.1 OVB generation results at λ_0 = 890 nm reported in [57] show correct phase dislocation structure and clearly light localization in intensity distribution in both numerical simulations (a) and experiments (b). Simulated images are captured at distance of 500 μm behind the end of VPMs.

Although the OVB exhibit correct helical structure of the phase and doughnut-like shape, its intensity distribution is azimuthally non-uniform. The radial non-uniformity shows clearly the high intensity is localizing at the high refractive index area. In other words, the output OVB created by the use of the fabricated nVPM has a light localization. This phenomenon is associated with waveguide effects inside thick phase components in which the light would propagate over a long distance.

This phenomenon could limit the possibility of practical applications of the nanostructured gradient index vortex phase masks, in particular in application with requirement of high uniformity of the beam intensity such as micro-machining for bulky or even surface structures [16]. Therefore, this part of my dissertation will present extensive numerical analysis to improve optical performance of various designed gradient index vortex phase masks. Specifically, I will focus on possible methods to improve quality of OVBs, mostly to improve the beam intensity distribution. There are few main factors could influence the OVBs created by the GRIN VPMs such as refractive index contrast of two glasses, refractive index profile, desired value of the topological charge of the mask.

Firstly, the influence of refractive index contrast in VPMs with topological charge l=1 is investigated. From Eq. 3.3 as per previous chapter, it can be seen the strong relation between value of refractive index difference of two glass materials constituting an nVPM and its thickness needed for realization of desired charge of the OVB. Thus, structures with various refractive index contrasts are considered as the first approach for improving the formed vortex quality. Our fabricated nVPMs are made of two different types of glass nano-rods and hence this technique offers an additional degree of freedom for seeking base-glass materials for different index contrast. Thus, it is promising that one can design a GRIN VPM with a suitable index contrast for generation of optical vortex having high-uniform intensity distribution. In principle, to avoid the waveguide effect, the fabricated nVPMs must be fabricated with thicknesses as short as possible which means the selected pair of glasses should have high refractive index contrast. On the other hand, the achievable shortest mask thickness is also a concern. This is because a component shorter than 18 μm is technologically challenging due to requirements on thickness accuracy.

Secondly, the variation of azimuthal refractive index profile of the component of charge l=1 is studied. As mentioned in the previous chapter, nVPMs are fabricated using a modified stack-and-draw technique in which the mask is constructed of thousand nano-rods made of two type of glass with high and low refractive indices. Thus, via internal index nanostructure with specific arrangement of those nanorods in a hexagonal lattice, an arbitrary refractive index distribution can be obtained. Our possibility of realization of arbitrary refractive index profiles can be used for improvement of the OVB intensity profiles. With that advantage, we carried out theoretical analysis of beam propagation for various curves of refractive index gradient of the nVPM.

Moreover, ability to use nGRIN VPMs to generate vortices with high topological charge by means of different number of 2π wrapped, phase steps and thickness values was simulated. It is known that the high-charge OVBs are very sensitive and difficult to generate which is also a challenge for the realization method using nanostructurization. On the one hand, as aforementioned in Chapter 3, it is possible to use thicker segments of the VPM with single charge to generate OVBs of higher charge values rather than the fundamental one. For that the thicknesses of these VPMs correspond to multiple thickness of the single-charge VPM. On the other hand, those OVBs can be achieved by the use of VPMs consisting of multiple identical segments with total phase variation of 2π in each segment. Both methods with longer thickness and with multiple 2π-index-period could generate optical vortices which provides different quality of intensity distribution.

4.2 Fourier transform beam propagation method for numerical study

In order to study the optical beams shaping by the designed nGRIN VPMs, the beam propagation through the mask and then propagating in the air are modeled. The schematic of modeling arrangement in order to evaluate the performance of OVB is presented in Fig. 4.2. It can be seen that the beam will propagate firstly through an inhomogeneous medium (VPM) and then in a homogeneous medium (air). For that purpose, I used an appropriate software employing the Fourier transform beam propagation method (FTBPM) [183] which has been written previously by a member of our group [178]. FTBPM approach shows the advantages in computation speed and memory requirements, especially prominent in case of large structure simulations, over finite-difference time-domain method.

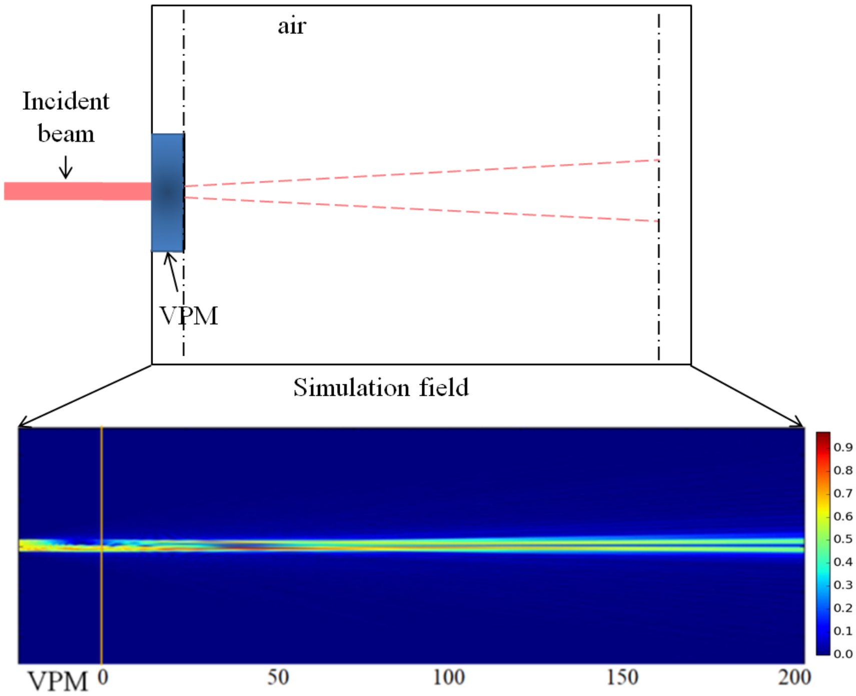

Figure 4.2 Schematic of numerical simulations of beam propagation through the VPMs

For an easy understanding, I firstly consider how FTBPM is applied for the beam propagation in a homogeneous medium and then in an inhomogeneous medium. Here the method is based on the numerical solution of the scalar Helmholtz equation [183] as the following expression:

$$\frac{\partial^2 u}{\partial^2 x^2}+\frac{\partial^2 u}{\partial^2 y^2}+\frac{\partial^2 u}{\partial^2 z^2}+k_0^2 n^2 u=0, \tag{4.1}$$

where k_0 is wave-number in vacuum. The medium has refractive index $n(x,y)$. Here the considerations are carried out for a monochromatic wave, so it is possible to write a field component in a form of $u(x,y,z)\exp(i\omega t)$.

In free space which is an isotropic medium, the refractive index $n(x,y) = n_0$. To study the beam propagation we have used an approach based on the angular spectrum technique which involves expanding a complex wave field into a summation of infinite number of plane waves. Its mathematical origins lie in the field of Fourier optics and results in solutions of Eq. (4.1) described in the form of Fourier integral:

$$u(x,y,z)=\iint_{-\infty}^{\infty} U(v_x,v_y,z)\exp[i2\pi(v_x x+v_y y)]dv_x v_y. \tag{4.2}$$

The term $U(v_x,v_y,z)\exp[i2\pi(v_x x+v_y y)$ can be understood as a plane wave with the spatial frequencies v_x and v_y. Now Eq. (4.1) becomes the equation for $U(v_x,v_y,z)$

$$\frac{\partial^2 U}{\partial^2 x^2}+(k_0^2 n_0^2-4\pi^2(v_x^2+v_y^2))^2 U(v_x,v_y,z)=0. \tag{4.3}$$

For simplification, let us put:

$$\beta^2=k_0^2 n_0^2-4\pi^2(v_x^2+v_y^2). \tag{4.4}$$

A family of solution to Eq. (4.3) can have the below form as presented in [183]

$$U(\nu_x, \nu_y, z) = U(\nu_x, \nu_y, z_0)\exp[-i\beta(z - z_0)] \quad (4.5)$$

Assuming that the field (x,y,z) is known at z = z_0 and hence using the Fourier transform, it is possible to determine the spectrum $U(\nu_x, \nu_y, z_0)$ using following formula

$$U(\nu_x, \nu_y, z_0) = \mathcal{F}\left(u(\nu_x, \nu_y, z_0)\right) = \iint_{-\infty}^{\infty} u(\nu_x, \nu_y, z)\exp[i2\pi(\nu_x x + \nu_y y)]d\nu_x \nu_y \quad (4.6)$$

The expression of $U(\nu_x, \nu_y, z)$ in Eq. (4.5) allows calculating its value at any *z*. Therefore, one can achieve $u(x, y, z)$ using the inverse Fourier transform (4.2) with the detail discussion given in [183]

$$u(x, y, z) = \mathcal{F}^{-1}\{\mathcal{F}(u(x, y, z_0))\exp[-i\beta(z - z_0)]\}, \quad (4.7)$$

Now we consider the monochromatic beam propagation in inhomogeneous medium whose refractive index at a certain point (x,y) is n(x,y). For our gradient index phase mask, the refractive index distribution changes linearly with respect to the azimuthal angle. Therefore, the phase correction must be applied and the complex field $u(x, y, z)$ should be rewritten with the use of averaged refractive index $\bar{n}$ in the cross-section of the computational volume as below [4]

$$u(x, y, z) = P(x, y, z)exp(-ik_0\bar{n}z). \quad (4.8)$$

From Eqs. (4.1) and (4.8), we obtained the equation for $P(x, y, z)$:

$$\frac{\partial^2 P}{\partial x^2} + \frac{\partial^2 P}{\partial y^2} + \frac{\partial^2 P}{\partial z^2} - 2ik_0\bar{n}\frac{\partial P}{\partial z} + k_0^2(n^2 - \bar{n}^2)P = 0. \quad (4.9)$$

Using the definition of nabla operator

$$\nabla^2 = \frac{\partial^2}{\partial x^2} + \frac{\partial^2}{\partial y^2} + \frac{\partial^2}{\partial z^2},$$

we obtain a simplified form of Eq. (4.9):

$$\nabla^2 P - 2ik_0\bar{n}\frac{\partial P}{\partial z} + k_0^2(n^2 - \bar{n}^2)P = 0. \quad (4.10)$$

Since the nanostructured component made of two different glasses with relatively low value of refractive index difference, it is possible to apply the approximation: $(n^2 - \bar{n}^2) \approx 2\bar{n}(n - \bar{n})$. As a result, from Eq. (4.10) we attain:

$$\frac{\partial P}{\partial z} = -i\frac{1}{2k_0\bar{n}}\nabla^2 P - ik_0(n - \bar{n})P. \quad (4.11)$$

It can be seen that the first term of the Eq. (4.11) corresponds to a free space propagation in the medium with a refractive index $n_0 = \bar{n}$. It is easy to obtain the formal integration of Eq. (4.11):

$$P(x, y, z + a) = \exp\left(-ia\frac{1}{2k_0\bar{n}}\nabla^2 - iak_0(n - \bar{n})P(x, y, z)\right), \quad (4.12)$$

where *a* is a constant representing distance increment on the z direction. In the case of constant *a* being small enough, we could apply Barker-Hausdor theorem [4] and approximate

$$exp(A + B) \approx exp(A)exp(B). \quad (4.13)$$

And Eq. (4.12) becomes:

$$P(x, y, z + a) = \exp\left(-ia\frac{1}{2k_0\bar{n}}\nabla^2\right)\exp\left(-iak_0(n - \bar{n})\right)P(x, y, z). \quad (4.14)$$

In this equation, the first term $\exp\left(-ia\frac{1}{2k_0\bar{n}}\nabla^2\right)$ introduces the free space propagation in the medium. The second term $\exp\left(-iak_0(n - \bar{n})\right)$ which is associated to the inhomogeneous properties of the medium is a phase correction.

Assuming that $P(x, y, z)$ for a certain z is known. Thus, in order to calculate $P(x, y, z + a)$ with small distance *a*, we firstly calculate the free-space propagation of distance *a* and then combine it with the term for phase correction. At first, the calculation of free-space propagation of the small distance *a* in the homogenous medium with a constant refractive index $n_0 = \bar{n}$ would be done by using Eq. (4.7) as below

$$P_{fs}(x, y, z + a) = \mathcal{F}^{-1}\{\mathcal{F}(u(x, y, z)) \exp(-i\beta a)\}. \quad (4.15)$$

Next we apply the phase correction corresponding to the medium inhomogeneity to get the final result:

$$P(x, y, z + a) = \exp(-iak_0(n - \bar{n}))\, P_{fs}(x, y, z + a) \quad (4.16)$$

In principle, this procedure is utilized for numerical calculation of a complex field (x, y, z) in subsequent planes perpendicular to Z axis when the initial field for $z = z_0$ is known. As a result, we obtain the beam propagation along Z axis. Fourier transform is realized as discrete Fourier transform (DFT) using fast Fourier transform (FFT) algorithm. Minimum lateral resolution of the simulation is determined by the sampling theorem [184]. It is sufficient when lateral steps Δx and Δy satisfy the condition:

$$\Delta x \leq \frac{\lambda_0}{2n_{max}}, \Delta y \leq \frac{\lambda_0}{2n_{max}} \quad (4.17)$$

where n_{max} is a maximum refractive index in the medium and λ_0 is the vacuum wavelength. Distance a has to satisfy the condition

$$a = \frac{\lambda_0}{2\pi|n - \bar{n}|}. \quad (4.18)$$

4.3 Quality parameter of optical vortex beams

As mention above, the aim of this work is to optimize possible parameters of the GRIN VPM in order to improve quality of generated OVBs, particularly, the uniformity of intensity distribution. For that purpose, besides the observation of the intensity distribution, we propose a quality parameter Q to easily evaluate the quality of OVBs (the mentioned uniformity).

The Q factor is calculated from the normalized light intensity distribution using Matlab. Fig. 4.2 represents an example of 4 main steps of calculation process to look for the quality parameter value Q of a tested vortex intensity pattern. Firstly, the tested vortex intensity distribution is normalized to 1. In the second step, the center of the vortex is determined manually (Fig. 4.3(a)). Next, the intensity distribution is converted from Cartesian (x,y) to polar coordinates (r,θ) as in Fig, 4.3(b). Meanwhile, the intensity pattern is divided into N equal-azimuthal segments of the angle value of θ_n. In the next step, for each angle segment θ_n the maximum intensity $\max(I_\theta)$ have to be found and plot in the frame of intensity and angles (see Fig. 4.3(c)). Finally, the Q parameter is calculated as a root mean square error (RMSE) using the formula:

$$Q = \sqrt{\frac{\sum_{n=1}^{N}\left(1 - \max(I_{\theta_n})\right)^2}{N}}$$

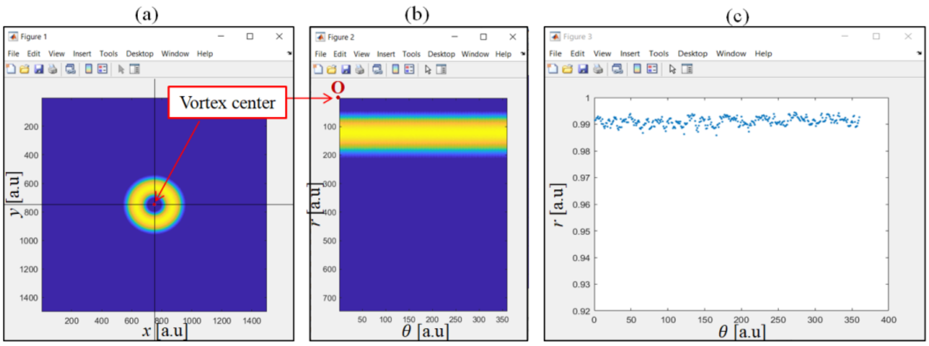

Figure 4.3 Procedure of vortex quality parameter (RMSE) calculation: (a) determining the centre point of the OVB; (b) converting the intensity pattern from Cartesian to Polar coordinates; (c) calculating the maximum intensity for each angle segment.

The specific values of Q parameter will indicate how uniformity of a vortex beam is by means that the smaller Q, the better uniform distribution. In Fig. 4.4, I introduce an example of a comparison of several intensity distribution patterns. It is straightforward that, when the Q parameter increases, the uniformity of intensity distribution falls.

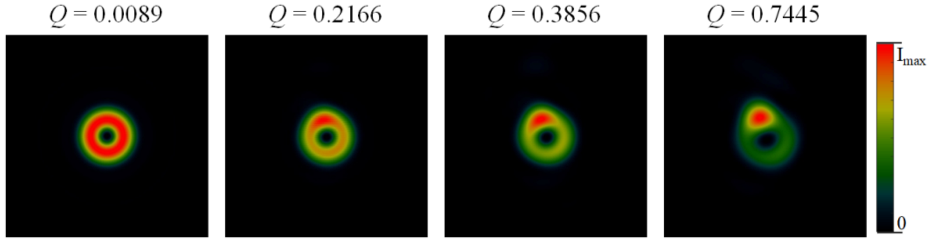

Figure 4.4 Example of using vortex quality parameter in comparison of quality of intensity distribution profiles of several generated OVBs.

4.4 Influence of refractive index contrast of nGRIN VPM on the vortex beam quality

As above mentioned, the nanostructured gradient index VPMs have been designed and fabricated with the use of two different glass materials. Thus the refractive index contrast, consequently the thickness of the nVPM, is defined by such a pair of glasses. Since the realization of the nVPM requires an appropriate pair of glasses, the selection of glass materials is very limited. Therefore, in this work numerical simulations are conducted for three refractive index contrast values corresponding to three available glass pairs which have been successful designed and synthesized at Łukasiewicz Institute of Microelectronics and Photonics, Poland [56,185,186]. The refractive index curves of such glasses materials are presented in Fig. 4.5.

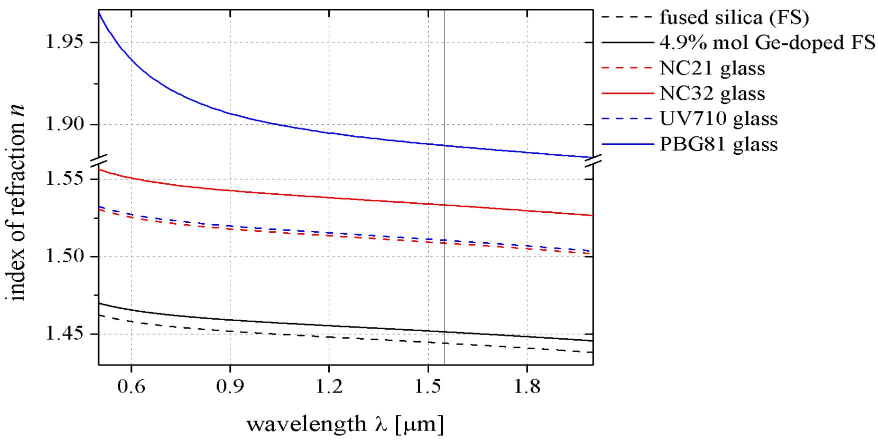

Figure 4.5 Dispersion properties of the three investigated glass pairs: UP (UV710 and PBG81); NC (NC21 and NC32); FS (fuse silica and Ge-doped silica glass) [61].

The requirement of compatibility of thermo-physical properties of each glass pair was experimentally proved. Those three pairs of glass materials have different refractive index contrast curves. As follows from Eq. (3.3) in Chapter 3, this leads to differences in thicknesses of nVPM structures for generations of OVBs with the same topological charge value $l = 1$. The basic properties of each VPM structure are introduced in detail below.

Here the first investigated pair of glasses which is labelled "UP" is two in-house made soft glass materials including lead-bismuth-gallate glass PBG81 and thermally matched silicate glass UV710. PBG81 plays a role of high refractive index material (n_0=1.887 at 1.55 μm) and UV710 has a lower refractive index of n_1=1.511 at 1.55 μm. It can be seen that their refractive index contrast is relatively high ($\Delta n \approx 0.376$). In order to generate OVBs charge $l = 1$, the total phase modulation should be 2π. Consequently, according with Eq. (3.3) in Chapter 3, the UP nanostructured VPM has a very short thickness $d \approx 4$ µm. This is much challenging for realization due to the technical limitations as discussed in Section 4.1.

Secondly, the next considered glass pair which is labelled "NC" is two in-house made boro-silicate glasses named NC21 and NC32. The refractive indices of NC21 and NC32 are of $n_0 = 1.5088$ and $n_1 = 1.5334$ at 1.55 µm, respectively. Their index contrast is $\Delta n \approx 0.025$. Consequently, to generate OVBs with charge $l = 1$, the NC VPM structure should have a thickness $d \approx 60$ µm which is feasible for fabrication.

The third studied pair of glasses which is labelled "FS" is made of silica-based glass materials. They includes a fuse silica glass with refractive index $n_0 = 1.444$ at 1.55 µm and 4.9 % mol Ge-doped silica with higher refractive index of $n_1 = 1.451$ at 1.55 µm. It can be seen that they have a very low refractive index contrast of $\Delta n \approx 0.007$. Therefore, the nVPM structure made of those glasses have a very long thickness $d \approx 230$ µm to generate OVBs charge $l = 1$. In this instance the waveguide effect will be most prominent.

It is assumed that all the computational simulations in this work are conducted with use of planar beam and with Gaussian intensity distribution which is limited by circular aperture with diameter of 20 µm at wavelength of 1.55 µm as the input source. All investigated nVPMs were 50 µm in diameter (the longer diagonal). For simplification, the structures FS, NC and UP are treated as continuous gradient structures whose refractive index profiles change continuously with azimuthal angle from n_{low} to n_{high}. We model the light beam propagation along z-axis through the VPM structures whose thicknesses d are calculated basing on Eq. (3.2). The simulation field has dimension of (x,y,z) = 600×600×500 µm. The step increment along x and y axes are the same value of 0.1 µm. Along the propagation axis (z-axis), the simulation steps are different for different media i.e. numerical calculations inside the structure have step of 0.1 µm, but it is longer when the beam propagates in air (0.5 µm).

In this section, the refractive index distributions of FS, NC and UP structures for generation of OVBs with topological charge $l = 1$ is studied. The thickness d of each structure is calculated as mentioned ($d_{UP} = 4$ µm, $d_{NC} = 60$ µm, and $d_{FS} = 230$ µm). All generated OVBs profiles are obtained at the same distance of 200 µm, from the end facet of the VPM structure. The captured results are canvassed into suitable size images for evaluations of output's properties as shown in Fig. 4.6.

It can be seen that the best result is shown for UP structure which is also confirmed by the lowest value of quality parameter $Q = 0.1527$ as shown in Fig. 4.6(a). Among all considered structures, this designed VPM has the highest refractive index contrast and the smallest thickness. With a very short thickness (4µm), the waveguide effect is minimized. As a result, the doughnut-like intensity pattern is almost uniform. The singularity is in exact center of the vortex and phase structure represents single spiral.

Figure 4.6(b) shows results obtained for NC structure which is thicker (60 µm) and designed for OVB with topological charge l=1. It is clearly seen that there is a localization of the light in the intensity pattern which reflects formation of high intensity spot related to high refractive index area. This is a consequence of waveguiding effect when the light propagates over a long distance inside the VPM. In this case, the intensity pattern shows a bright ring with the quality parameter $Q = 0.7372$ confirming visible non-uniformity. Despite that, the phase distribution is still perfect with single spiral arm and the zero-intensity region illustrating the singularity of phase structure aligns with the center of the pattern.

In the last case of FS structure depicted in Fig. 4.6(c), it is hardly to see doughnut shape although the phase structure is relatively well preserved. In particular, due to the very thick VPM (230 µm), the generated OVB presents very strong light localization which is caused by the waveguide effect occurring in high refractive index area. Additionally, this also leads to the shift of the phase singularity position with a distance of around 10 µm from the center of the structure towards the high intensity spot. This performance of FS structure disqualifies it for practical applications and hence development of VPMs according to FS design is not planed. Moreover, from above analysis it can be seen visually and deduced from quality parameter *Q,* the intensity profile of UP structured VPM is relatively uniform and could be accepted for most of applications.

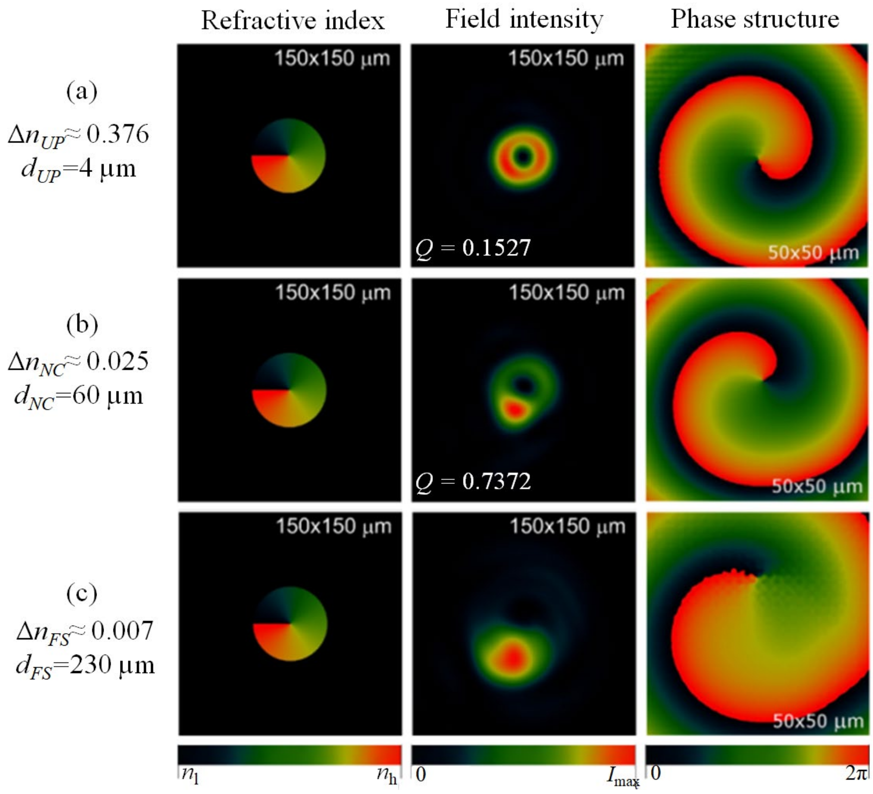

Figure 4.6 Numerically calculated intensity profiles of OVBs for proposed structures UP, NC and FS with refractive index distributions and corresponding generated OVBs' properties [61].

We conducted additional simulations to check the trend for even much higher refractive index contrast. Beside the fact that assumed in simulation glass parameters does not exists and polishing such a thin structure is not feasible, we expect OVBs to look ideal. Our simulation showed that minimal value of the contrast to obtain ideal OVB must by very high. We used NC21 glass material as a low refractive index glass (n_0 = 1.5088 at 1.55 µm) and another, hypothetical with refractive index shifted by Δn = 15.5. Consequently, the thickness of the artificial structure is of 0.1 µm which is extremally thin and waveguide effect disappears. The results of the simulation are presented in Fig. 4.7. We obtained perfect uniformity of intensity profile as well as perfect phase structure. The quality parameter *Q* is near zero.

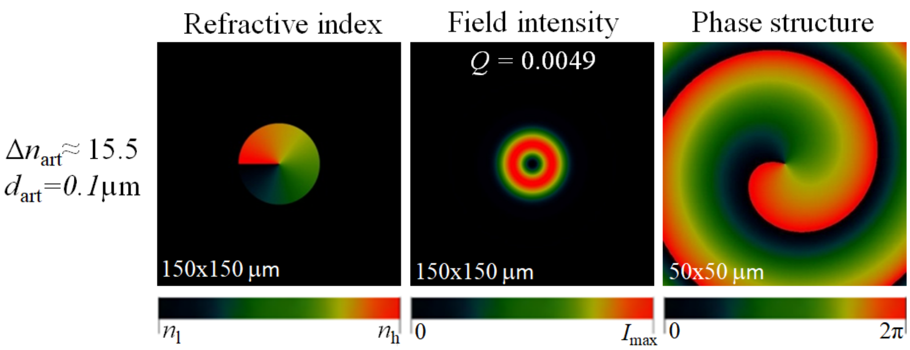

Figure 4.7 Simulated OVB generated by using a GRIN VPM with a very high refractive index contrast.

Those above analyses bring us an essential insight on the influence of the waveguide effect taking place inside bulky structure of nGRIN VPMs. The thicker the mask the influence of waveguide effect is stronger. That means for thicker masks the light is highly localized in the high refractive index area. As a result, although the phase structure of generated OVBs is still correct, their intensity distributions show the azimuthal non-uniformity and the phase singularity point tend to shift to the light localization region. Therefore, to obtain better OVBs, the thickness of the VPM should be reduced and, the refractive index contrast of two glass materials must be increased. However, from technical point of view, the mask production is much challenging in case of thickness of the order of single micrometres. In the final step of the fabrication process, we grinded and polished 1-mm-segments of nVPM structures to reduce their thicknesses to obtain thin nVPM components for the purpose of this thesis [57]. In those mechanical processes, it is difficult to obtain accurate thickness with thickness error lower than fraction of micrometer. Alternatively, it can be considered alternative approach, such as chemical etching [187].

4.5 Influence of nonlinear azimuthal refractive index distribution of nGRIN VPM on the vortex beam quality

As discussed in previous section, the generation of high-quality OVBs of fundamental topological charge could be achieved with very thin nGRIN VPMs. However, it is also mentioned previously that the realization of such very thin mask is challenging in the modified stack-and-draw fabrication method. On the other hand, all investigated structures so far were with linear azimuthal refractive index gradient. In other words, we only considered various refractive index contrasts Δn of two glass materials and keep the linear variation of refractive index distributions. Thus in this section, a proposed an alternative solution to explore the effect of azimuthal nonlinear refractive index profile to improve the quality of the vortex formation. That means different curves of index variation $n(\theta)$ following the azimuthal angle θ are applied to discussed NC and UP structures. The dependence of $n(\theta)$ on θ is expressed as below modelled formula:

$$n(\theta) = n_{low} + \Delta n \left(\frac{\theta}{2\pi}\right)^{1/g} \tag{4.19}$$

where the azimuthal angle θ receives values in the range [0, 2π]. Index g denotes the shape power index. Chosen g values with corresponding $n(\theta)$ profiles are presented in Fig. 4.8.

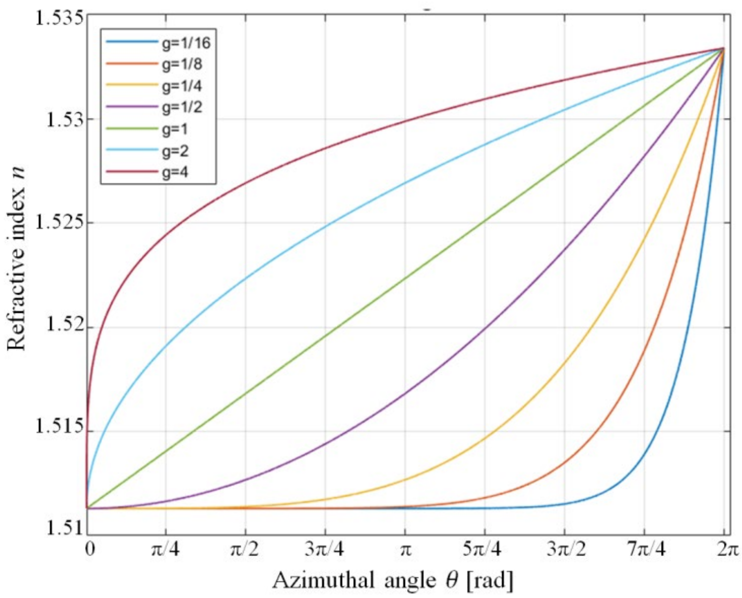

Figure 4.8 Various plotted curves present various dependences of refractive indices on azimuthal angle θ for NC structured VPM with thickness of 60 μm.

In detail, for large g values, i.e. g = 4, the area of high refractive index in the designed structure is extended. On the contrary, for fractional value, i.e. g = 1/16, the high refractive index area is minimized. And when g = 1, we have previously discussed linear gradient.

Numerical simulations for NC and UP structures use the same parameters as those in the previous section, but the only difference is the azimuthal non-linear index profile. A family of power functions with different shape index g are considered. All generated beams are visualized at distance of 200 μm from the end facet of the VPMs.

Firstly, I would discuss the results obtained for nonlinear NC structured VPM which are presented in Fig. 4.9. It can be seen that the shape power index g strongly influences on optical performance of these NC structures. In other words, the intensity distribution in the cross-sectional bright ring pattern of the generated vortices clearly depends on values of g. In particular, for $g>1$, it increases the light localization in a single spot, consequently, the doughnut-like intensity becomes highly non-uniform. The results became worse for the shape power index value above g=4 for which the beam is no longer doughnut-like shaped. And there is strong shift of position of phase singularity point. Similar effect occurs for values of the shape power index below g =1/8. The good results of generated OVBs is obtained for the shape power index in range of 1/4÷1 in which the intensity is distributed more uniformly in the light ring but localization spot is still clearly visible. On the other hand, most of considered structures provides correct phase distribution with a clear phase singularity, except for the cases of g =1/8 and 1/16. In those cases, we do not get the phase singularity; instead, constant phase areas appear and locate at the center of the phase structure. That means the output beams of those structured VPMs are not optical vortices any more.

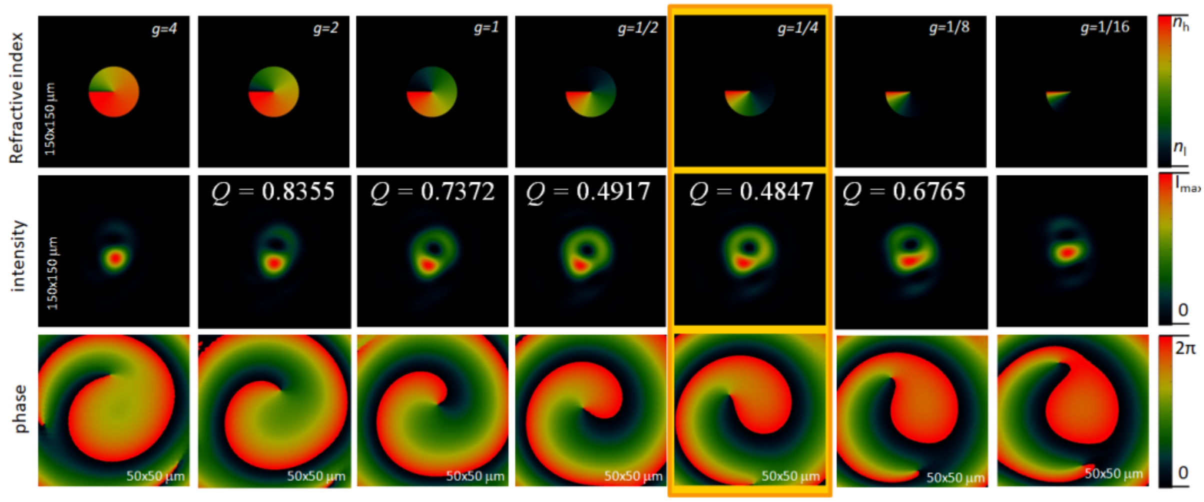

Figure 4.9 Simulated field intensity and phase of OVBs charge 1 generated with corresponding NC structures of different refractive index profiles which is determined by shape power index $\boldsymbol{g}$ [61].

Noticeably, for proposed nonlinear function with g = 1/4, the intensity improvement is achieved as shown in highlighted frame in Fig. 4.9. The result is confirmed by the lowest value of quality parameter Q = 0.4847. However, uniform donut shape is still impossible to be obtained even when we consider a full set of monotonic azimuthal profiles of refractive index described by the power functions in Eq. 4.19. This is because that the waveguide effect caused by nonuniform refractive index distribution in thick masks.

In addition, numerical simulations are also performed for UP structures with different refractive index profiles corresponding to different phase power index values g. As aforementioned, this gradient index structure is very thin (thickness of 4 μm) due to the high refractive index contrast of $\Delta n \approx 0.376$ at 1.55 μm. In this set of numerical model, only the refractive index profiles of UP structures are changed while their other parameters are remained as used in the previous section. Figure 4.10 below presents simulated results of performance of such designed structured masks.

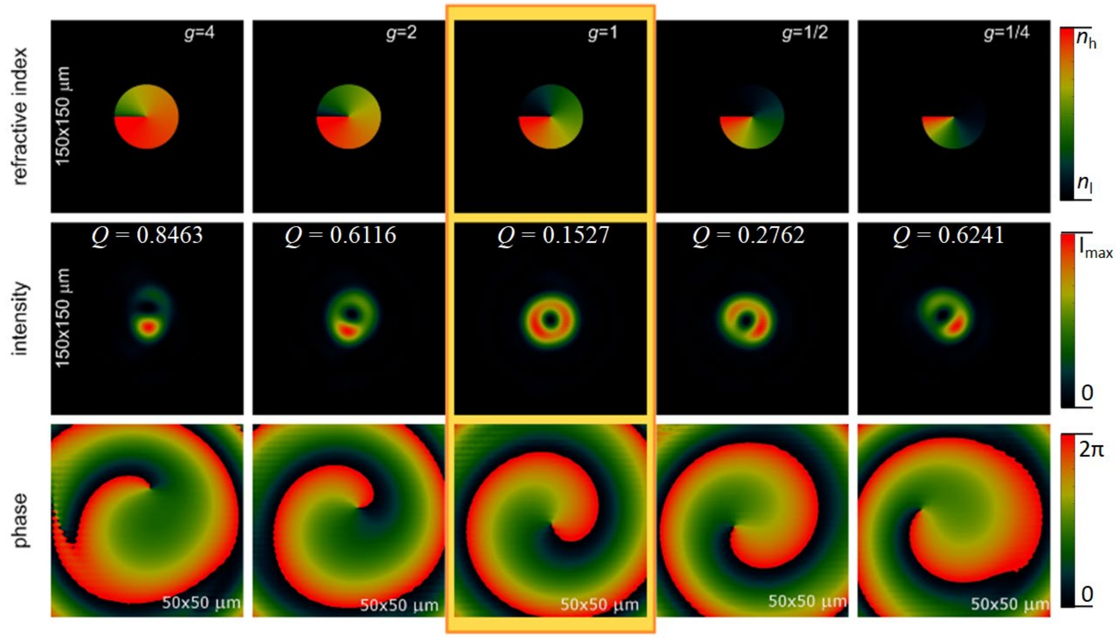

Figure 4.10 Simulated field intensity and phase of OVBs charge 1 generated with corresponding UP structures of different refractive index profiles which is determined by shape power index ***g*** [61].

The results show that the best performing OVB is achieved for the UP component having linear change of azimuthal refractive index distribution $g = 1$ (highlighted in Fig. 4.10). It produces correct helical phased structure and almost uniform intensity distribution on the beam cross-sectional pattern which is confirmed by the lowest value of quality parameter Q=0.1527. In this structure, the waveguiding effect is minimal so there is no lack of expected improvement with use the nonlinear profile of the refractive index. For all g values phase structures are correct and distorted only for two extreme values of g. In other words, any modifications of refractive index profile inside the UP structured VPM do not help to improve quality of formed OVBs, which, instead, emphasize localization region in the intensity profile.

In this section, the impact of nonlinear monotonic azimuthal refractive index distribution of nVPM structures on intensity improvement has been analyzed. The investigation results show that the quality of generated OVBs in terms of highly uniform intensity and correct phase structure could be improved only in the case of thick structure with moderate index contrasts, e.g. NC structure. This method allows minimizing the waveguide effect which is the cause of light localization spot in cross-sectional intensity pattern. The phase structure is still maintained correctly. As a result, the generated microscopic-size OVBs reach an acceptable quality. As we consider the structures and materials which are suitable for fabrication, we are limited in thickness and in refractive index contrast, while azimuthal distribution of refractive index can be formed freely. Therefore, in realization, the best option for generation of single charge OVB is to use NC structured VPMs with a thickness of 60 µm and a nonlinear monotonic azimuthal refractive index distribution ($g = 1/4$) and moderate refractive index contrast of $\Delta n \approx 0.025$.

For a considerable extend, numerical calculations are also conducted for an nonlinear high contrast structure with a feasible thickness of 15 µm. This designed VPM would have a moderate refractive index contrast of $\Delta n = 0.103$ which could be possibly obtained for a soft-glass pair. Here we used the presented NC21 glass as a low refractive index glass ($n_0 = 1.5088$ at 1.55 µm) and assumed high index of refraction $n_0 = 1.6118$ at 1.55 µm. A series of various g values as in case for the NC structure are utilized for simulations. The results are shown in Fig. 4.11.

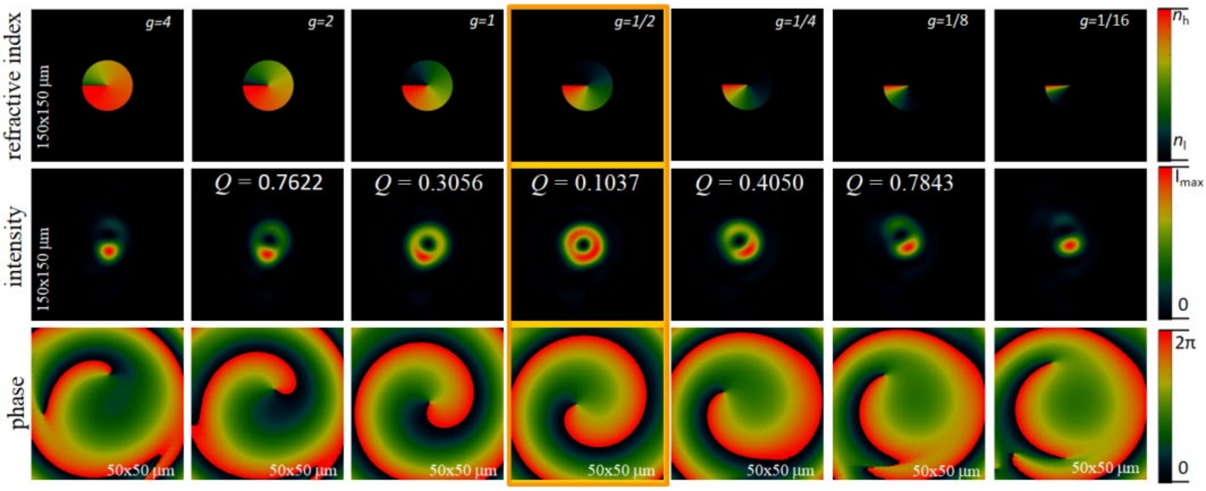

Figure 4.11 High refractive index contrast structures with thickness of 15 µm to for selected values of power index ***g***.

As a result, the optimum OVB is obtained for the shape power index of g=1/2 due to minimization of waveguide effects. The intensity distribution in the beam cross-section is almost perfectly uniform with a correct phase structure. Its calculated quality parameter reaches the smallest value Q = 0.1037. This improved version even has better Q factor than for the OVB generated by the optimum UP structured VPM (a very small thickness of 4 µm.

4.6 Generation of high-charge vortices with nanostructured GRIN VPMs

In two previous sections, we have been focused on modifications of nGRIN VPMs for the generation of OVBs with topological charge l = 1 thereby total phase variation is up to 2π. The masks for higher topological charges should have multiple of 2π. In principle, this can be achieved with use of nGRIN VPMs with two methods. The first method is dividing the mask into multiple number of identical angular zones, with the phase change of 2π in each zone [188] while the materials and thickness of the mask remains the same. In the second method, the component's thickness can be increased by multiple of its thickness needed for topological charge l = 1 as per Eq. 3.3 in Chapter 3. The relation of topological charge values of generated OVBs and the number of 2π-phase zones of the VPM are introduced in Fig. 4.12. The plots depict required index profiles (here with constant gradient) to create single and multiple 2π-phase-gradient-zone VPMs for formation of OVBs.

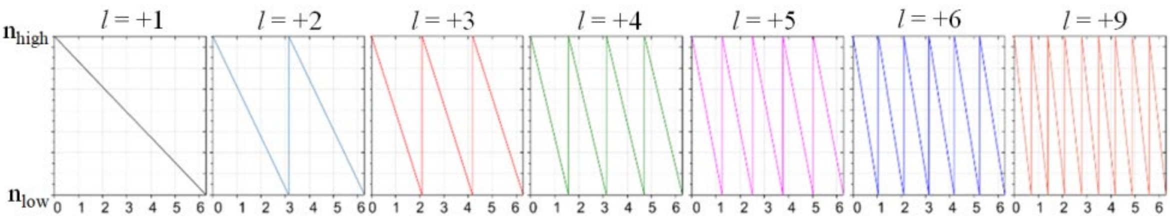

Figure 4.12 Azimuthal linear-index profiles of designed VPMs with 1, 2, 3, 4, 5, 6 and 9 2π-phase zones distributed uniformly clockwise for generation of corresponding OVBs at wavelength of 1.55 µm.

However, both methods do not perform well in case of thick VPMs. For instance, the generation of OVBs with charge l = 2 using NC structure have been un-successful when applying both of those methods. As aforementioned, this NC-glass VPM for generation of OVBs with charge 1 is quite thick (60 µm). The output beam obtained from a 60-µm-thick VPM with two 2π-phase-gradient zones is depicted in Fig. 4.13(b) while results for the twice thick NC structure (120 μm) is shown in Fig. 4.13(c). By looking at the phase maps, it is clearly seen that both output beams emerged from those structure are not optical vortices in LG mode sense. Moreover, the obtained beam intensity profile in the first method has more than one intensity localization due to waveguiding effect inside small angular 2π-phase-gradient zones of the thick component. In the second method of 120-μm-thick VPM, the doughnut-like intensity profile is barely visible due to much stronger waveguiding effect associated with beam propagation in this very thick component.

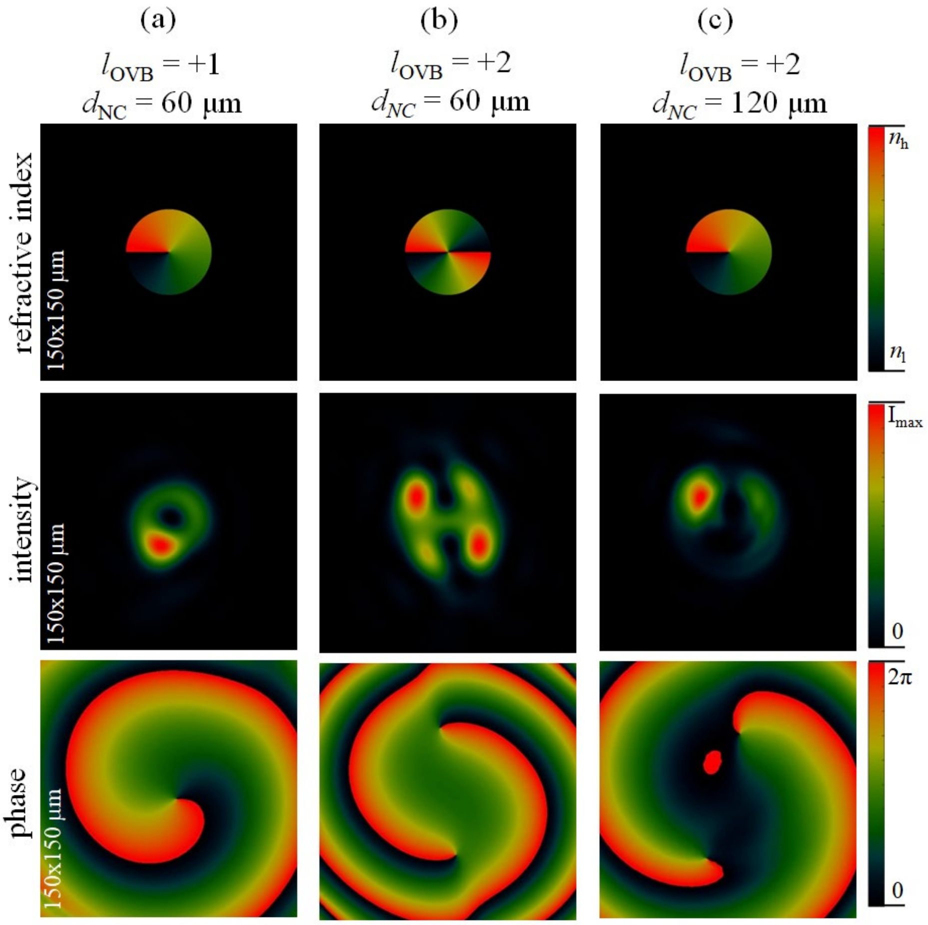

Figure 4.13 Double-charge OVBs generated using the VPMs with either a thickness of 120 μm (b) – a double value of the VPMs of single charge (a) or two 2π-phase-change zones in a 60-μm component(c).

In the next set of numerical simulations we present results of considerations of higher topological charge of UP structures with linear refractive index profile, thickness of 4 μm and diameter of 50 μm. For the first approach, those masks have refractive index profile with 1, 2, 3, 4, 5, 6 and 9 2π-phase zones distributed uniformly clockwise, which should generate the optical vortex with the charge l = +1, +2, +3, +4, +5, +6 and +9, respectively. The simulated results are presented in Fig. 4.14. It can be seen that by using VPMs with refractive index profile including 1, 2 and 3 2π-phase-gradient-index zones, we obtained OVBs with reasonably uniform intensity patterns and clear phase structures which indicates their topological charge values of l=+1, +2, +3, respectively. This is confirmed by the low values of Q parameter. However, it also can be seen that there are a number of light localization spots in the cross-sectional intensity patterns which are equal to the topological charge values of vortex beams. Additionally, the singularity of a higher-order OVB is divided to l displaced singularities visible as additional dark regions. Probably the darkest spitted region is for charge 1 because numbers of new dark spots coincides with vortex charge. This phenomenon was also observed by other research groups in case of standard phase masks [189].

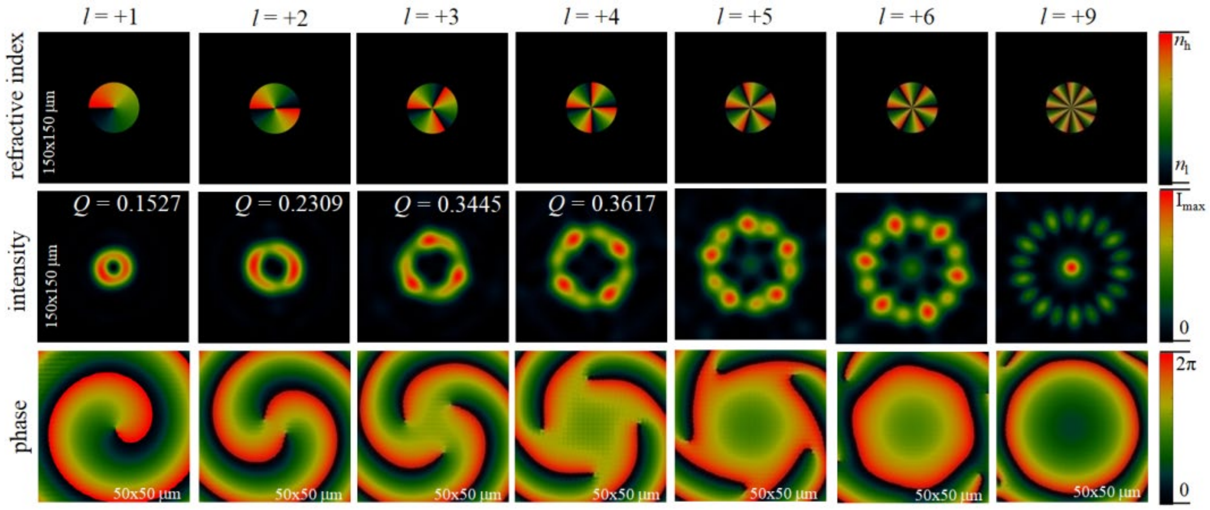

Figure 4.14 Simulated results for high topological charge OVB generations using the UP-structured VPMs with refractive index profiles of single and multiple 2π-phase zones. All the masks have thickness of 4 µm and diameter of 50 µm [61].

In other cases, the output beams generated using UP-glass VPM with more than four 2π-phase zones in it are not l charged vortex beams. Although their intensity cross-sections show kind of doughnut-like shape resemblance, but in each case, there is an additional light localizations at it perimeter as well as in the center. Their phase structures are complex with flat phase in the center surrounded by vortex-like phase distribution in peripheral areas. This phenomenon is caused by the small size of the angular 2π-phase gradient index zones structured inside the VPMs and higher sensitivity of high-charge vortices to the mask imperfections. In fact, these vortices can be destabilized breaking up into constituent single charge vortices. With increase of charge the size of individual 2π-phase gradient index zone becomes small enough that beam locally interacts simultaneously with multiple gradient structure. As a result, the averaging effect related to EMT [173] begins to play a dominant role in the centre of the beam generated by the VPM. This leads to the lost of phase singularity and the appearance of a central constant phase area in the phase of the generated beam. For a VPM with higher number of 2π-phase gradient index zones, this effect is dominant for larger part of local medium and results in location of intensity peak in the centre of the beam.

Subsequently, the second longer UP structured segments of thicknesses being multiplication of the base thickness of fundamental-charged VPM is considered. This aims at verification of usefulness for high-order OVBs formation by means of nVPMs. The optical performances of UP structures with various thicknesses from 4 to 32 µm (corresponding to charge l = +1 to +8, respectively) are presented in Fig. 4.15. It can be seen that the output beams emerging from all investigated UP structures is maintaining doughnut-like shape without the central light spots. However, the non-uniformity in the out beam cross-sections is stronger for the OVBs generated from thicker VPMs as predicted earlier. This effect confirmed the influence of waveguide effect and it maybe also a reason for the shift in XY plane of central constant phase spots. Similar to previous approach applied for UP structures in this section, the appearance of constant phase spots at the center of the beam for thicker VPMs can be explained as high-order singularity being split into fundamental ones that shift away from the beam center.

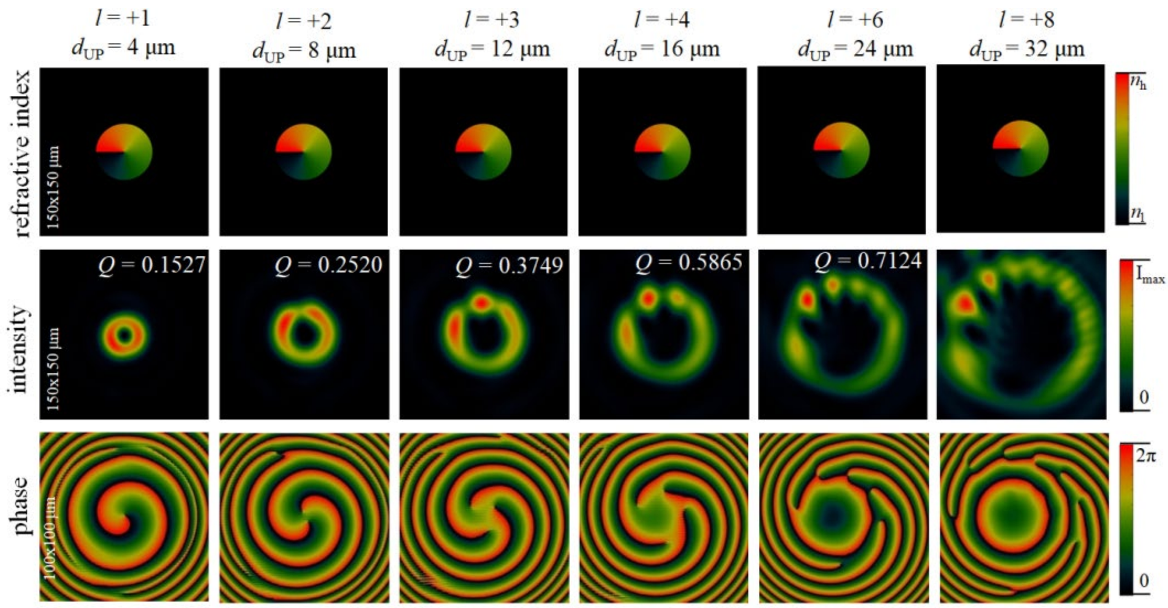

Figure 4.15 Numerical verification of formation of OVBs with topological charge of l=+1, +2, +3, +4, +5, +6, and +8 by the use of UP structures with various corresponding thicknesses. Their refractive index profiles linearly change with respect to azimuthal angles from 0 to 2π [61].

4.7 Summary

In this chapter the numerical studies on optical performance of nanostructured GRIN VPMs for OVB generations were performed. Simulations reveal that the non-uniform intensity profile of the generated OVBs is caused by waveguide effects which could be minimized by engineering of refractive index profiles. In fact, as the gradient masks can be fabricated by using various pairs of low and high index glasses, which can result in different mask thickness. The results demonstrated that the best approach to minimize the waveguiding effect is to fabricate mask employing glasses which provides highest possible refractive index contrast. In that case the thickness of the mask would be minimized so the wave-guide effect could be negligible. We found that practically feasible vortex mask with charge l = 1 can be created using in-house synthesized thermally matched pair of lead-bismuth-gallate glass PBG81 and silicate glass UV710. Since refractive index difference between the glasses is very high $\Delta n_{UP} \approx 0.376$, a phase mask with linear azimuthal gradient index profile which corresponds to 2π phase shift can be achieved in a plate of 4 µm thick at the operating wavelength of 1.55 µm.

However, fabrication of such a thin component is technologically challenging due to requirements on thickness accuracy. For this reason we found a compromise in case of VPMs with technically achievable thickness of 60 µm. Furthermore, the beam intensity profile can be improved by non-linear azimuthal gradient index profile. Different shape power index values of proposed nonlinear refractive index profile of the components were considered and the significant improvement in uniformity of vortex beam intensity distribution (and proper singular phase) was achieved by using nonlinear azimuthal gradient index function with the shape power index g =1/4. As a result a 60-µm-thick, well performing nVPM can be obtained in case of using in-house made pair of thermally matched borosilicate glasses. Specifically, glass NC21 and NC32 ($\Delta n_{NC} \approx 0.025$) with compatible designed rod-arrangement was used. The numerical simulations showed that although, the wave-guide effect cannot be totally eliminated, it can be minimized leading to acceptable intensity patterns of the generated vortex beam.

Finally, possibilities to use GRIN VPMs to generate vortices with higher topological charge values were investigated. The results showed that the masks consisting of multiple identical segments with total phase variation of 2π in each segment were able to generate a vortex beam with charge up to $l = 3$ for UP structures with relatively uniform beam intensity profiles. However, generation of charge vortices with higher charged than 3 was unsuccessful as light propagation resulted in loss of phase singularity and formation of structures with nonzero light intensity in the center. Furthermore, longer UP structured segments with thicknesses having multiplication of the base-thickness of the fundamental-charged VPM was analyzed. The results depicted that high-charge OVBs with correct doughnut shape without intensity spot in the center were achieved for the considered cases.

Chapter 5. Optical characterizations of single VPMs in free space and liquid media

In this chapter, the optical performance of single nanostructured gradient index vortex phase masks (nVPMs) in various external media is investigated theoretically and experimentally. The initial verifications of performance of nVPMs in free space is a continuation of the previous work done by K. Switkowski et al. [57]. To a considerable extent, the deeper study on behaviors of our nVPMs was carried out and had been reported in the article [62]. Our flat-surface microscopic-size components whose structure contains spatially distributed nano-rods made of two thermally matched glasses with high and low refractive indices were, as mentioned previously, fabricated by the modified stack-and-draw technique. The measured optical properties of the generated vortices with azimuthally phase distribution are presented. In section 5.1, a brief description of geometrical properties of the selective fabricated nVPM samples is introduced. Then the following section shows the numerical simulation results for light propagation through modeled GRIN vortex masks of those selected samples. Finally, experimental results are presented to verify the optical performance of such fabricated nVPMs. It should be noticed that all tests were conducted firstly in the air and then in different liquid media, specially, water and ethanol. Both numerical and experimental studies agree and show that performance of the nVPM is unaffected by the refractive index of the surrounding environment making it an excellent candidate for micro-fluidic applications.

5.1 Study method and geometrical properties of investigated nVPMs

The first investigation of optical performance of fabricated nanostructured VPMs was reported by K. Switkowski and his colleges [57]. The report shows that by using a VPM sample having a long thickness of 36 µm, single charge OVBs at a wavelength of 890 nm was successfully generated in the air but its intensity distribution is non-uniform with a light localization. To a considerable extent, the deeper study was conducted for VPMs with thinner thickness and different external media had been reported in the article [62].

As stated in previous chapter, the influence of waveguide effect on beam profile is stronger for longer VPMs. Thus, inhere the thinner masks operating at red light emitted by He-Ne laser (633nm) are characterized. The numerical simulations and experiments are performed for VPMs with the same designed structure but varied thicknesses to verify the conversion from fundamental light beam into optical vortices with different topological charges. Two VPMs with thickness values of 25 µm and 50 µm are chosen, according to the theoretical predictions, in order to observe OVBs with topological charges $l = 1$ and $l = 2$ at wavelength of 633 nm, respectively.

Furthermore, the helical phase variation following the azimuthal angle is resulted directly from the azimuthal modulation of refractive index inside the nVPM. That means the mask performance is unaffected by the refractive index of the surrounding environment. Thus, it is expected that the same components can be used in different media. For a verification, all tests for 25-µm-thick nVPMs are conducted firstly in the air and then in two other liquids – water and ethanol.

In this work, the selected VPM samples are fabricated with the use of the modified stack-and-draw technique described in detail in Chapter 3. This method allows developing binary nanostructured components with truly continuous phase profiles with the diameter of tens of micrometer. Here, the whole diameter of investigated micro-optical component is 125 µm and the central vortex phase structure is of ~20 µm as shown in Fig. 5.1. The flat-surface component structure contains total 7561 circular rods with the diameter of ~200 nm which are spatially arranged in a hexagonal lattice following the designed pattern. Those rods are made of two thermally matched glasses with high and low refractive indices and their index contrast is of Δn = 0.25 at a wavelength of 633 nm.

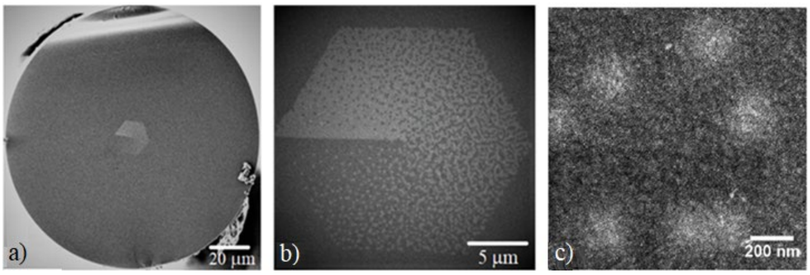

Figure 5.1 Fabricated nVPMs. Scanning Electron Microscope (SEM) images of the whole components (a); vortex structure (b); magnified part of vortex structure with visible individual nano-rods made of high refractive index glass (bright regions) and the low refractive index ones (dark regions) [62].

5.2 Numerical investigations of the optical performance

In order to numerically study the optical properties of OVBs generated by designed nanostructured GRIN VPMs, the Fast Fourier Transform Beam Propagation Method (FFT-BPM) has been employed. The implementation of the FFT-BPM had been explained in detail in chapter 4. The simulations were performed for both ideal continuous GRIN VPM as well as the corresponding binary nanostructured pattern (depicted in Fig. 5.2) in which the input parameters for both vortex masks are the same with those of the fabricated structures as mentioned above.

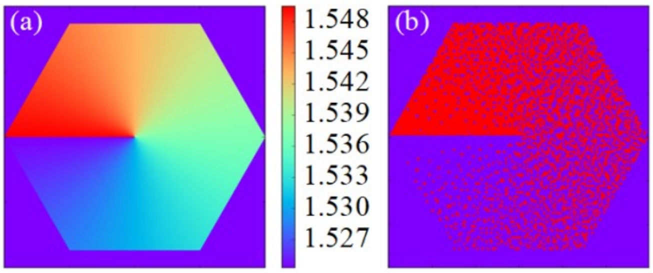

Figure 5.2 Designed gradient index VPMs with ideal continuous index distribution (a) and corresponding binary nanostructured pattern used for fabrication (b). This figure based on [62].

Here it is assumed that all computer calculations were performed for plane input wave at wavelength of 633nm propagating through the VPMs and then the output beam travels over a distance of 200 µm along its optical axis in free space or in water and ethanol liquids. All field intensity and phase cross sectional profiles in XY plane of simulated OVBs will be visualized at the end of simulation area.

The first simulation set is for determination of the most suitable incident beam size in order to obtain the most uniform intensity distribution of OVBs. For that purpose, we numerically checked for several incident beam diameters, specifically 12, 15, 18, 20, 23 and 30 µm. In this work, we conduct simulations only for the ideal continuous VPM with the structure diameter of 20 µm and the thickness of 25 µm. In theoretical calculation, we should obtain OVBs with fundamental topological charge (l=1) at the wavelength of 633 nm. The simulated results are shown in Fig. 5.3. From simulation results it can be seen that the generated vortex beam with the most uniform characteristic is converted through the VPM from a planar beam of 18 µm diameter. This is also indicated by the smallest quality factor (Q = 0.3098) among these simulated cases. Therefore, the beam with diameter of 18 µm will be used for all conducted simulations and experiments in this chapter.

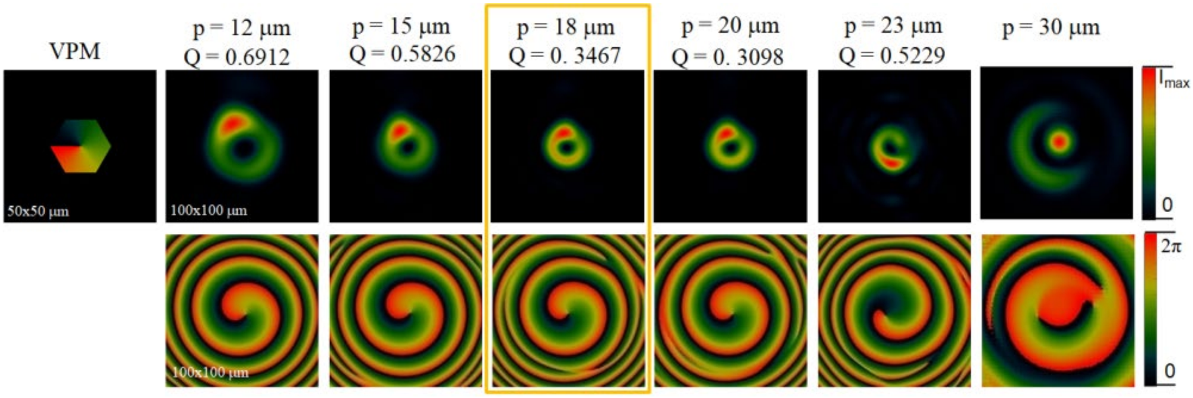

Figure 5.3 Numerical results for testing the influence of size of incident-beam on the field intensity and phase structure of OVBs generated by designed ideal continuous GRIN VPM charge 1.

The next set of simulations was carried out for comparison of optical performance of designed continuous refractive index VPMs and its corresponding binary nanostructured VPMs. Both components have thicknesses of 25 μm and diameter of 20 μm. The input planar beams are of 633 nm with a size of 18 μm diameter as mentioned. All results are visualized at 200 μm distance behind the masks. The attained numerical calculations for VPMs in free space are performed in Fig. 5.4.

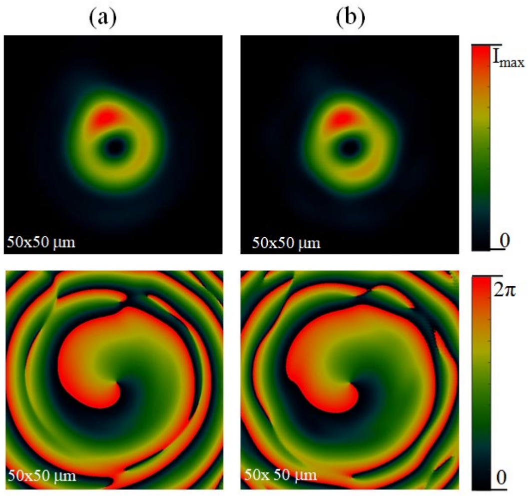

Figure 5.4. Results of numerically simulations for continuous refractive index mask (a) and binary structure (b) in free-space: simulated field intensity (first row) and phase structure (second row) of the generated OVBs with topological charge $l = 1$.

The simulations showed that both obtained OVBs have doughnut-like intensity structure and single arm spiral phase pattern. That shows our designed components with a thickness of 25 μm can generate optical vortex of topological charge $l = 1$ in air. In addition, simulated results for binary nanostructured masks are very similar to the ideal one. That means there is no degradation of the optical performance of the nanostructured VPM with respect to ideal continuous VPM. The obtained results confirm that the nanostructured mask acts as continuous phase mask. Internal binary structure fulfills requirements of EMT. However, it is visible that the light intensity distribution is azimuthally non-uniform. This non-uniformity reflects the influence of relatively long beam propagation through the mask as numerical analyses discussed in Chapter 4. This waveguide effect leads to the tendency of light beam to be guided predominantly in the higher refractive index area of the VPM structure. However, the intensity distribution of the expected OVBs in this case are predicted to be more uniform than the case reported in [57]. It is understandable because the thickness of components used here are smaller, thereby the waveguide effect is weaker as discussed previously

In addition, we also simulated the generation of OVBs using continuous refractive index VPMs in two different external media: water (n_w = 1.333) and in ethanol ($n_{ethanol}$ = 1.360). The same input parameters for both types of masks as the former case were used. The results of those simulations are very similar to the case of air (see Fig. 5.5). This means predicted optical performance of GRIN VPMs for generation of optical vortices with topological charge l = 1 is not affected when the masks is immersed in water or in ethanol. Results prove the main advantage of GRIN vortex masks and can be extrapolated to any transparent liquids.

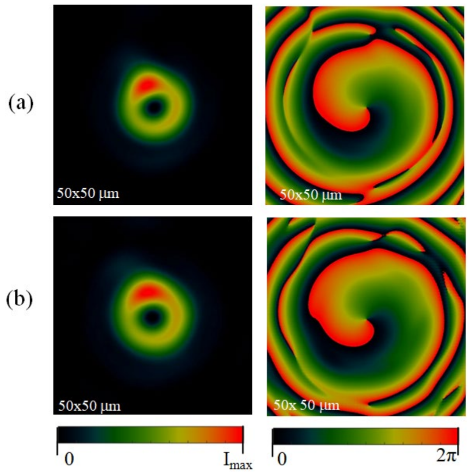

Figure 5.5 Simulated intensity and phase profiles of OVBs using the same designed continuous index VPM in different external media: water (a) and ethanol (b).

The last numerical simulations were perform in order to study optical performance of GRIN VPMs for generations of OVBs with charge l = 2 in air. These masks are twice thicker (50 µm) than the above VPMs (25 µm), but the rest parameters of these structures are the same e.g. 20 µm in diameter. Figure 5.6 depicts field intensity and phase profiles of the vortices in the case of ideal continuous refractive index component and its corresponding binary nanostructured one. It can be seen that the field intensity profiles have larger dark center areas in comparison to previously shown single-charge beams. The phase patterns have two arms in the spiral, which indicate creating of double-charge OVBs.

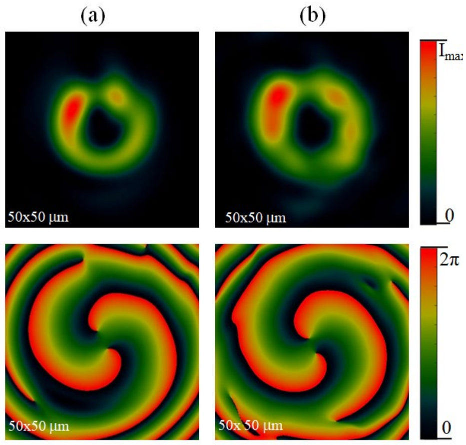

Figure 5.6 Numerically simulation results for continuous mask (a) and binary structure (b): simulated field intensity (first row) and phase structure (second row) of the generated OVBs with topological charge l=2.

Those results confirmed that the generation of an optical vortex with topological charge l = 2 at a specific wavelength λ_0 requires a GRIN VPM component with a thickness being twice greater than the one used for the generation of a single charge vortex beam l = 1. This agrees with theoretical calculation from Eq. 3.12.

However, it is noticed that the optical performance of OVB generation using the GRIN VPMs is worse for the case of higher topological charge l = 2. One of the reasons for this is that the required masks are much thicker, so the waveguide effect is stronger. Secondly, in general the higher order of the vortex beam the more susceptible for any imperfection which makes the stability of higher order OVBs is worse than for the beams with charge l = 1.

5.3 Experimental verifications

For the experiments, two parallel-facet nVPMs with diameter of ~20 µm and thickness of 25 µm and 54 µm thickness were selected for generation of vortex beams with topological charge l = 1 and l = 2, respectively. Our fabricated masks were glued to an edge of the microscope cover-slip glass (20 × 20 × 0.5 mm) by using optical UV-curable adhesive (see Fig. 5.7). The masks were mounted in a glass cuvette shown glass box in Fig. 5.7(c). The cuvette allows masks to be immersed for studies of their optical performance in different liquids such as water and ethanol.

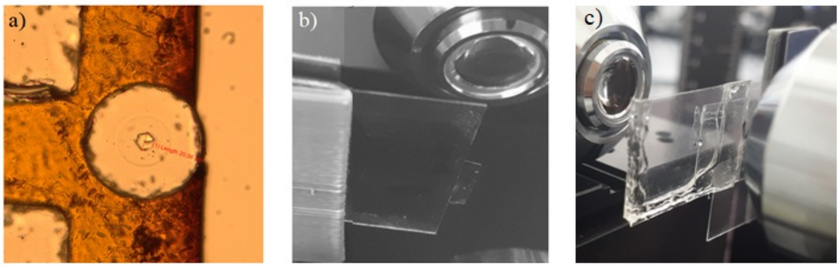

Figure 5.7 Image of an investigated VPM in microscopy (a). VPM samples mounted for experiments performance in air (b) and in water (c) [62].

In order to experimentally characterize the optical performance of fabricated nanostructured vortex phase mask samples described in section 5.1, the set-up depicted in Fig. 5.8 was used. The setup is used for observing intensity distribution, phase dislocation of the generated OVBs or measuring their topological charge with the use of astigmatic transformation technique [190] or Mach-zehnder interferometer configuration [79]. Each of aforementioned optical setup needs to be rearranged. In experiment the Gaussian beam impinging the mask must have proper diameter (~18 µm) as shown previously in numerical calculations.

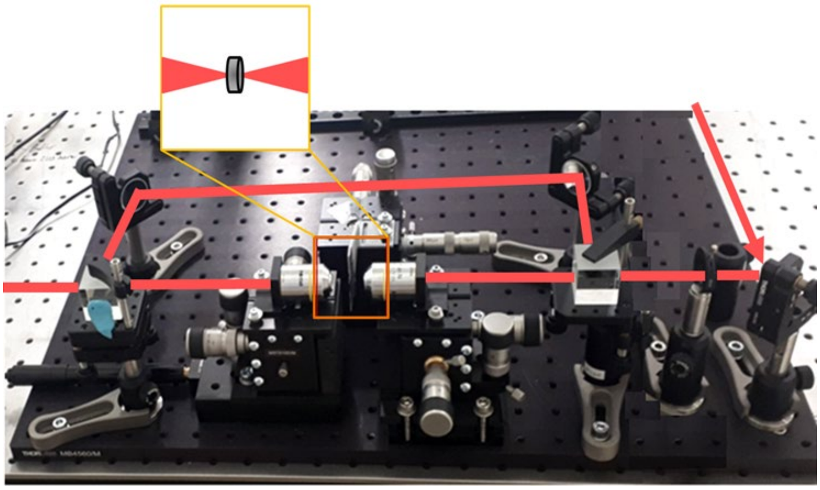

Figure 5.8 Experimental setup for characterizing optical properties of selective fabricated VPM samples

In the constituted set-up, a He-Ne laser source emitting the light with relatively high coherent length and stable central wavelength of 632.8 nm, is used to perform measurements. The prepared VPM sample was clamped to a three axis precision translation stage (Thorlabs, Nanomax) for sample alignment. Its surface planes are determined by scanning with the imaging system along the optical axis. All measurements have been taken with the same set of a microscope objectives and a CCD camera. Specially, a pair of microscope objective lenses with ×10 magnification and NA = 0.25 were used. One is for focusing collimated He-Ne laser, which impinging on surface of the component and another is for imaging and collimating the transmitted beam. The resulting beam was projected onto the camera with set same pixel gain and exposure in all experiments. In the case of the 632.8 nm laser, we used a Thorlabs CMOS camera offering a full-frame resolution of 1280 x 1024 pixels. The camera and objective lenses were mounted on computer controlled 2D translation staged to ensure the fixed distance between elements in the imaging setup.

Firstly, in order to observe the intensity distribution of the generated vortex beam, the set-up was operated following the scheme depicted in Fig. 5.9. In which, the collimated light coming out from the laser was focused with the first microscope objective into a small spot at the center of the sample mask. The transmitted divergent beam after propagating through the nVPM was collimated and projected on camera by the second identical objective and its cross-section intensity profile was recorded.

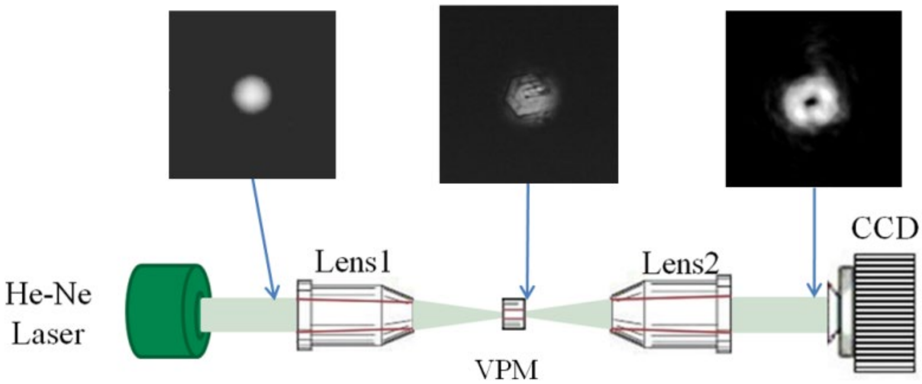

Figure 5.9 Schematic of experimental setup for observing cross-sectional intensity distribution of the OVBs generated by fabricated VPMs.

Next, for diagnostic of topological phase structure of obtained optical vortices, few different techniques have been applied. They include astigmatic vortex transformation to Hermitte-Gaussian (HG) modes by cylindrical lens [190] and formation of interference patterns between vortex beam and the Gaussian reference beam realized in Mach-Zehnder interferometer configuration [79]. In the former approach, a cylindrical lens was placed directly in front of the camera as shown in Fig. 5.10(a). Consequently, the cylindrically symmetric vortex is transformed into a pattern of elongated dark and bright stripes in the focal plane. In the later case, the interference measurement with an operation scheme illustrated in Fig. 5.10(b). Interferences of vortex beam with reference spherical waves result in spiral intensity patterns and fork-like pattern which allows confirming the singularity and topological charge value of the generated OVBs. The detail of these techniques was discussed in section 2.2, Chapter 2.

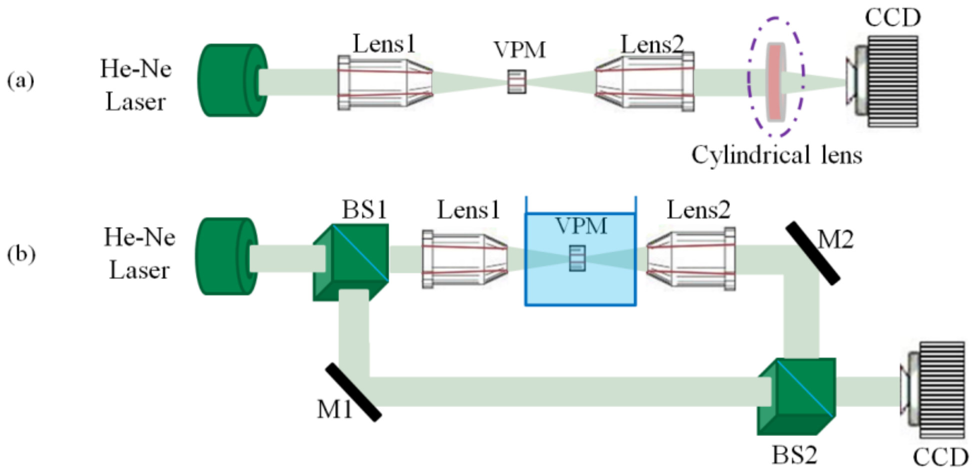

Figure 5.10 Experimental schemes for study of phase characteristic and topological phase structure of obtained optical vortices.

Following discussions are devoted to analysis results of optical characterizations for 25-µm-thick nVPM in air and liquid media which, according to the theoretical calculations, is expected to convert the incident light into a single charge OVBs (l = 1) at 632.8 nm wavelength of the input beam.

Figure 5.11(a) depicts the experimentally observed annular character in light intensity distribution of OVB obtained in free space. Its dark central region well indicates existence of phase singularity of the beam. This is also seen on graphs in Fig. 5.11(b, c) which show horizontal and vertical intensity profiles of the vortex cross-section, respectively.

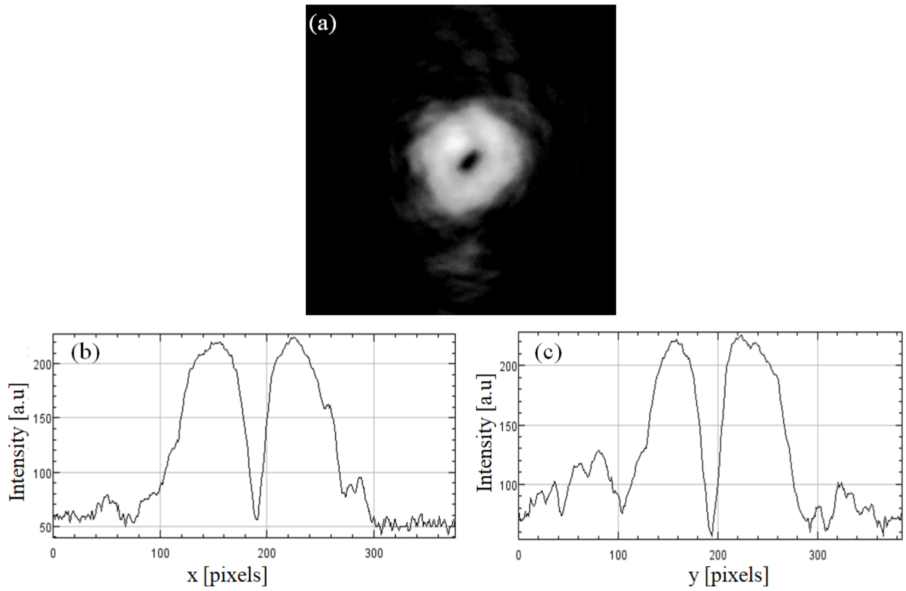

Figure 5.11 Cross-sectional intensity pattern of the OVB generated in the air (a) and its horizontal and vertical profiles (b, c) show the singularity at center of the beam. Measured intensity contrast ratio of the vortex is > 15:2.

The intensity distribution on the ring-shape is visibly azimuthally non-uniform, in which the light localizes in one location. This non-uniformity reflects the predominant guiding of light in the higher refractive index area inside the structure of the phase mask as numerical simulations discussed previously.

The astigmatic transformation pattern obtained on the surface of sensor of the CCD camera after OVB propagating through a cylindrical lens allows determining the beam topological charge. There are two distinct bright extended bands separated by a dark stripe indicating the single topological charge $l = 1$ (Fig. 5.12(a)).

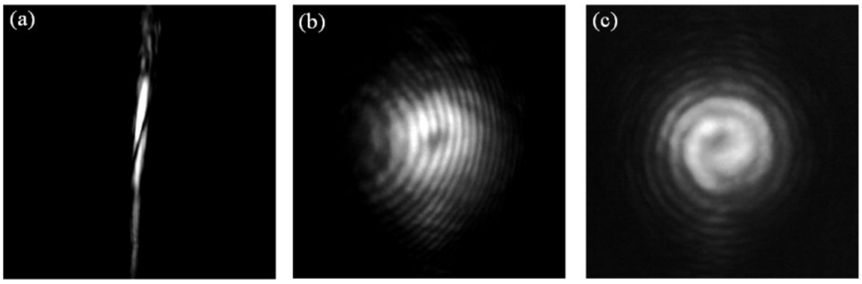

Figure 5.12 Astigmatic transformation structure using a cylindrical lens (a); interferograms of resulted OVB by using collimated (b) and spherical (c) reference beam. The presence of the fringe with bifurcation at the singularity of the fork-like pattern as well as single spiral arm indicates single charge ($l = 1$).

The result is firmly confirmed by intererograms shown in Fig. 5.12(b) and (c) achieved in Mach-Zehnder interferometric measurements involving collinear and non-collinear reference beams, respectively. Indeed, in the fork-like structure, there is one extra fringe coming out from the central zero intensity region substantiating the axial singularity as well as single topological characteristic of the OVB. Moreover, a relevant result is seen in the spiral pattern – a single spiral arm. All these points proved the formation of a single-charge OVB at wavelength 632.8 nm propagating in air for the use of 25-μm-thick nVPM. These experimental results are in good agreement of previously described computer simulations. Moreover, it is also noticed that in practice, the optical performance of the fabricated binary nanostructured GRIN VPMs is better than those shown in simulation. This could be explained by the sharp refractive index differences on the borders between various nano-regions presenting in numerical simulations. In the fabricated structures, melted glass diffuses from one to others and refractive index profiles of borders between two glasses is smoothed out [177].

Altering the polarization state of incident beam did not show any observable differences in any of patterns showed here since our nVPM is a scalar vortex generator. The formation of optical vortex beams is due to the azimuthal modulation of refractive index in the nVPM which results in the phase variation following the azimuthal angle. That means the mask would replicate polarization of incident beam. The internal nanostructure of nVPM is irregular and much smaller than wavelength, therefore it doesn't influence on polarization of the propagating beam. Moreover, we also note that local birefringence variation can be observed in the case of gradient index components as it was reported in the case of ion-exchange based gradient index lenses [191]. A similar effect may take place in gradient index components developed by means of nanostructurization. The nVPM drawing process does introduce only marginal stress, which locally generates small birefringence in comparison to other phase mask production methods. Moreover, this effect is negligible since nanorods are made of thermally matched pair of glasses, and fiber drawing process is carried out in optimized thermal conditions to reduce local stress, as we have previously shown for silica-based nanostructured gradient index microlenses [192]. Low residual birefringence of the drawn fiber and the fact that the mask is very thin makes optical properties of the final nVPM structure polarization insensitive.

The most interesting property of nVPMs is its lack of optical performance degradation when it is immersed in liquid media. So far this was not proved experimentally. Therefore in the scope of this thesis, optical measurements performed for the nVPM immersed in water liquid medium will be discussed and reported in [62]. The fabricated component having thickness of 25 μm, used in previous experiments, was placed into a glass cuvette containing pure water as in Fig. 5.7(c). The same techniques as above would be utilized to characterize the optical behavior of the mask. As a consequence, the experimental results are depicted in Fig. 5.13 and it shows that putting the mask in water does not affect its optical performance. In detail, the intensity pattern of vortex cross-section is presented in Fig. 5.13(a) which has characteristic doughnut-like shape manifesting the presence of the phase singularity in the centre of the transmitted beam. The figure is accompanied by graphs showing intensity distribution along x and y directions of the generated cross-sectional beam (Fig. 5.13(b, c)).

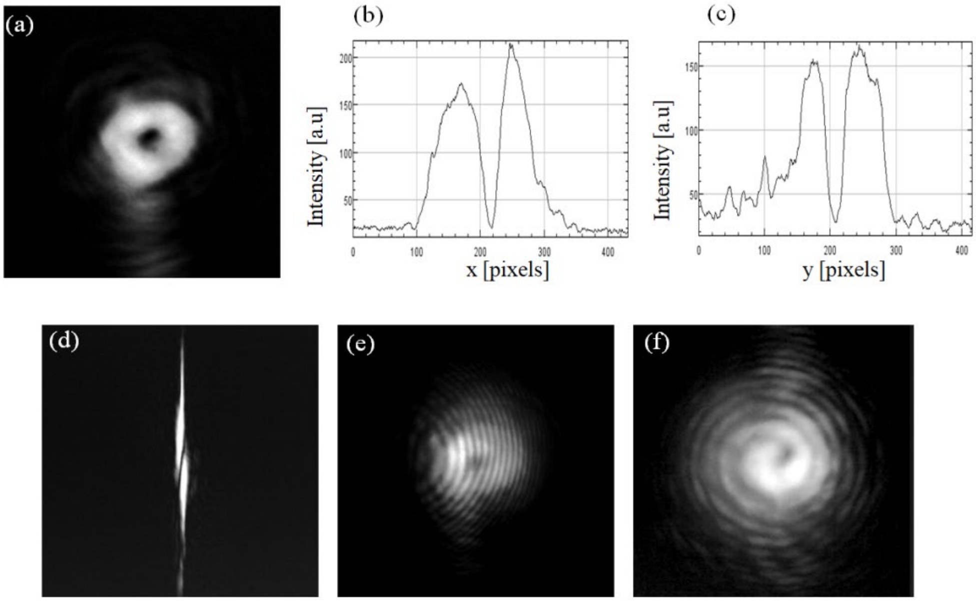

Figure 5.13 – Experimental optical characterizations of the OVB generated using the 25-μm-thick nVPM immersed in water: (a) annular intensity distribution; (b, c) its horizontal and vertical intensity profiles; (d) the astigmatic transformation pattern of the OVB; (e, f) fork and spiral interferogram structures. Measured intensity contrast ratio of the vortex is > 10:3.

Figures 5.13(d), (e) and (f) show an astigmatic transformation patterns obtained after the formed OVB is transmitted through a cylindrical lens as well as observed interferometric patterns. The results demonstrate the value l = 1 of vortex topological charge. Therefore, it can be concluded that the fabricated VPM persists its optical characteristics in water. In other words, once designed and fabricated nanostructured masks work well as a vortex converter in air as well as in water and the properties of generated OVBs do not changed.

To a considerable extent of impressive evidences involving the preservation of optical properties of our flat-surface nVPMs in other liquid media, we used ethanol. The experiment was conducted with the same mask and experimental techniques. Measured results are presented in Fig. 5.14. We obtained very similar performance, even though the surrounding medium of the component has higher refractive index (n = 1.3604 at 633 nm). There is also a doughnut-like intensity distribution with a visible dark central region in the intensity pattern as well as it horizontal and vertical profiles. It suggests the existence of phase singularity of the output vortex. Additionally, its single charge l = 1 is ascertained due to the presence of one dark elongated strip in the astigmatic transformation pattern; the presence of only one extra fringe and single spiral arm in the corresponding interferograms.

The experimental performances for the nVPMs in all of three media reveal the non-uniform light intensity. This is difficult to avoid due to the waveguide effects taking place when the light beams propagating through such a thick GRIN component. However, it is visible that the resulting images from measurements for the same investigated mask obtained in liquid media are less diffused than those in the air. This issue is associated with the scattering from the roughness of the mask's surface. Because of technological limitations, the certain roughness was exerted during mechanically polishing step. When the mask was put in the liquid media with higher refractive indices the air, difference in refractive indices between interfaces is much smaller thereby inhomogeneity is less visible. Consequently, light scattering from the rough surface of the flat component in liquids is much smaller than that in the air.

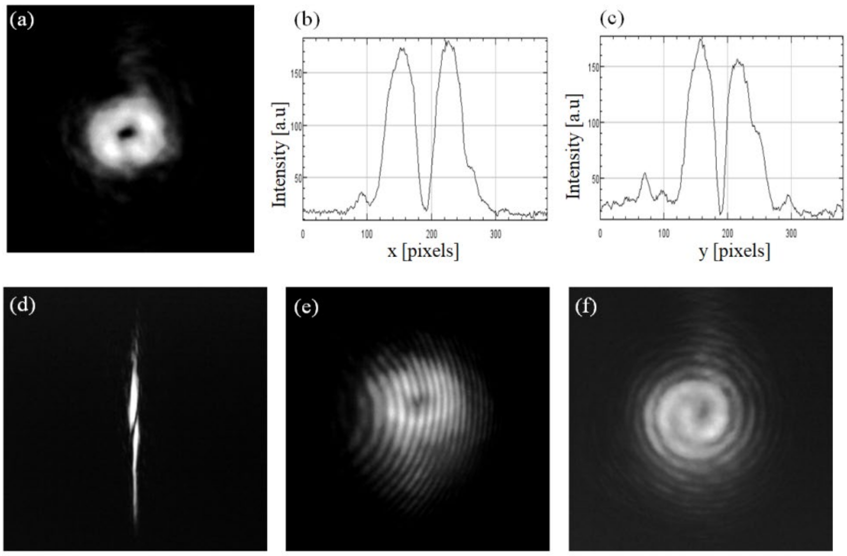

Figure 5.14 – Experimental characterizations of the OVB resulted from propagation of Gaussian beam through the 25-μm-thick nVPM immersed in ethanol: (a) annular intensity distribution; (b, c) its horizontal and vertical intensity profiles; (d) the astigmatic transformation pattern of the OVB; (e, f) fork and spiral interferogram structures. Measured intensity contrast in the vortex > 15:1.

Hereinafter, further experimentally studies have been carried out for generations of higher charge OVBs in the air using nVPM samples with the same structure [62]. For that purpose, we had investigated another mask with almost twice longer thickness (54 μm). With the same input source (central wavelength of 632.8 nm), this component should form an OVB with the topological charge l = 2. The same experimental steps that were utilized for previous study on 25- μm-thick VPMs had been applied in these measurements. Consequently, it results in patterns of intensity profiles, astigmatic transformation structure and integerograms introduced in Fig. 5.15.

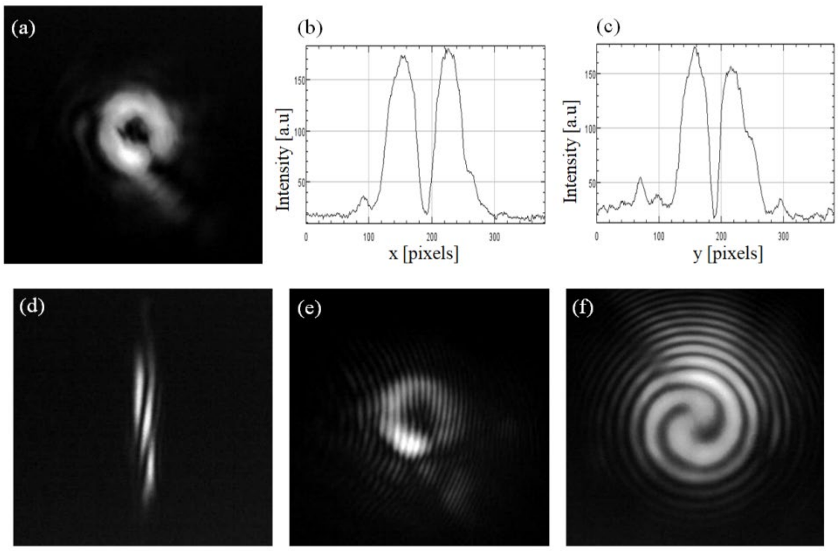

Figure 5.15 – Light intensity patterns of the cross-sectional OVB profiles obtained be propagation of the gaussian beam through the 54-μm-thick nVPM of and its horizontal and vertical distributions (a, b, c). Patterns formed by cylindrical lens and modified Mach-Zehnder interferometer setup illustrate the double topological charge of the OVB (d, e, f). Measured intensity contrast ratio of the vortex is > 15:1

Figures 5.15(a-c) show the annular intensity characteristic with a visible phase dislocation at the center of vortex cross-section. However, the central dark area of the cross-sectional intensity distribution is now wider which suggests higher topological charge. In fact, in the structure imparted by the cylindrical lens due to the astigmatic transformation of the vortex in Fig.5.16(d), there are two disparate dark stripes determining double charge vortex (l = 2). This is also agreed by the fork and spiral intensity interferometric patterns attained from Mach-Zehnder experiments – two additional fork-finges and double spiral arms. The obtained experimental results agree with previously presented results of numerical calculations. This confirms that the nVPM operating at wavelength of 632.8 nm allows generation of an OVB with topological charge l = 2.

Due to the technical limitations in accuracy of cutting and polishing final mask sample, the thickness of the nVPM used here was 54 µm a slightly longer than the theoretically calculated (50 µm). This difference in thickness of 4 µm and together with coexisting influence of wave-guiding effect, as discussed before, contributed to the non uniform intensity distribution.

5.4 Summary

To sum up, in this chapter, the optical performance of two selected nanostructured gradient index vortex phase masks (VPMs) with thicknesses of 25 and 54 µm in various external media was verified experimentally. In particular, intensity distribution, existence of phase singularity and topological charge were determined experimentally.

Obtained results showed agreement with simulated results for designed GRIN VPMs and fabricated nanostructured GRIN VPMs. That means the binary nanostruturization technique is one of the most feasible method for fabrication of vortex masks. Only visible drawback is the non-uniformity of the vortex intensity profiles. This associates with light wave-guiding effects thick GRIN phase structures. This issue can be minimized when glass materials with high refractive index contrast are used in fabrication process thereby, allows the VPMs to have lesser thicknesses as discussed in Chapter 4.

However, in comparison to the converters realized by other techniques, our micro-optical VPMs have remarkable unique properties. Due to flat-parallel surfaces, they can be easily and efficiently integrated into compact fiber optics systems. In contrast to other methods it is cost effective, once drawn a few meters of the fiber can be used to mass production plenty of discrete mask elements. Additionally, it is also demonstrated that the same fabricated vortex structured fiber could be used to produce various vortex phase masks for generations of OVBs with different topological charges by cutting VPMs into slices of suitable thickness. More importantly, both numerical and experimental studies demonstrated that the mask performance is unaffected by the refractive index of the surrounding environment making it an excellent candidate for microfluidic applications.

Chapter 6. Fiber-based vortex converter microprobe

The novel nanostructured GRIN VPM, discussed in details in the previously chapters, has flat surfaces making its optical performance unaffected by surrounding transparent media which is in contrast to conventional SPPs. The usage of VPMs allows converting flat wavefront incident light into helically phased beams with diameter of tens of micrometer which is insensitive of the working environment. However, those considered single optical VPM s are of microscopic spatial dimensions, so the mask itself is rather difficult to operate. Therefore, integration of the nVPM with a single-mode optical fiber path to form a fiber-based vortex converter microprobe was proposed such that it can be manipulated easily and reliably. The concept, fabrication and characterization of such a new type of the novel optical microprobe was presented for the first time in [63]. The system comprises of a single mode fiber (SMF) path, coreless fiber spacer element and the novel nanostructured VPM. The main idea of this chapter is focused on such the vortex converter system development and its verification, not on the phase mask itself. In the present chapter, I will discuss more detail in terms of practical integrations, numerical simulations and experimental verifications of the optical performance of the integrated converter system in the air as well as immersed in water. Through that, in overall it proofs the compatibility of our nVPM elements with optical fiber technology. In particular, the concept of the fiber-based vortex converter microprobe and its creation process is described in details in section 6.1. Process of integration of the nVPM and the spacer with the fiber needs very high precision active alignment procedures performed under the microscope. In the next section, I present a proof-of-concept of the novel compact fiber-vortex converter microprobe with numerical simulation analysis of the generated OVBs. Eventually, the experimental verification discussion of the results obtained fiber-based vortex converter in various external media is presented in section 6.3.

6.1 Optical fiber-based vortex converter microprobe: Concept and integration technique

A novel fiber-based vortex converter microprobe, whose concept is presented in Fig. 6.1, would be directly integrated from separate components. They include a nanostructured vortex phase mask, a spacer and a single mode optical fiber (SMF) compatible with the operating light source.

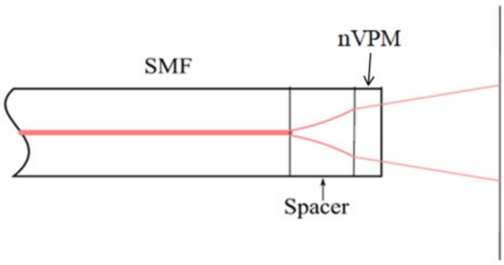

Figure 6.1 Schematic of fiber-based vortex converter microprobe composing of a SMF, a spacer and a VPM.

All fabricated nVPM samples used in this work are circular with an outer diameter of 125 µm and their central the hexagonal nano-structures have the longer diagonal of 20 ± 0.5 µm. Due to small diameter of the SMF fiber mode and relatively large area of the mask, there was a need for use of an additional core-less-fiber element, spacer, which will expand the beam on the all mask area. The thickness of the spacer is carefully calculated and they should be in microscopic spatial dimensions, typically around of 60÷100 µm. In this way, we obtained uniform illumination of the whole area of the mask, without overfilling the hexagonal aperture. In the case of overfilling, we would have a spurious diffraction pattern of the hexagonal structure observed in the vortex beam. From the other hand, the insufficient filling would not provide good quality vortex beam. The exact value of the thickness of the spacer depends on the core size of the light delivery fiber as well as VPM structures. It would be estimated by numerical simulations reported in the next section.

In the preparation step, the nVPM samples contained in glass holders, after the final stage (cutting, grinding and polishing) of fabrication described in Chapter 3, were checked under a microscopy in terms of structure diameter and thickness (illustrated in Fig. 6.2(a-b)). Polished micro-optical components having required thickness were selected according to theoretical calculations as mentioned in section 3.5 in Chapter 3. Next, the selected vortex masks were taken out from the glass holders by precise tweezers. Then they were glued on the optical transparent glass plate with the usage of water based adhesive (Fig. 6.2(c)). This task requires high precisions and much patient since all nanostructured components here have microscopic size of 125 μm in outer diameter and less than 100 μm thickness.

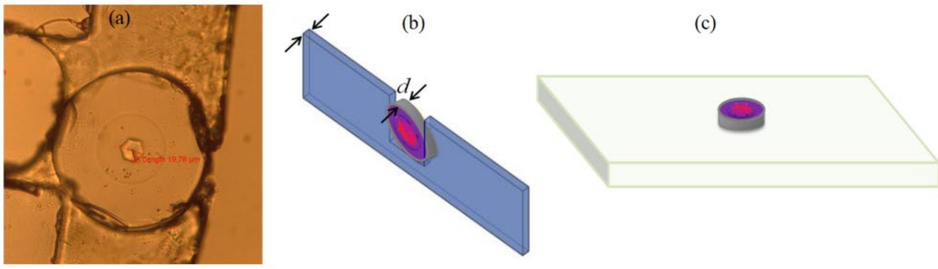

Figure 6.2 Fabricated VPM samples contained in glass holder after the fabrication process (a-b) and the selected sample glued on glass plate for integration (c).

The above procedure of nVPMs preparations before integrations was also applied for the spacers. The spacer was developed in-house using a borosilicate glass labeled NC21 which is the same lower refractive index glass used for nanostructure VPMs. An optical high-quality NC21-glass rod was drawn down to a rod with a diameter of 125 μm in a fiber-drawing tower. The drawn coreless fiber was then cut into short pieces of 1 mm length, and the bunch of samples are polished using fiber polishing machine (Automet 250 Grinder-Polisher, Buehler) until achieving the required length.

Process of integration of the nVPM and the spacer with the fiber needs very high precision active alignment procedures performed under the microscope. Any small misalignments between core and nVPM result in deformation of the output beam and deterioration of vortex generation. Therefore we have built a microscope-based station for fiber microprobe assembly and worked out a full procedure for assembly single-mode fiber with ultrathin micro-optical components. Figure 6.3 shows a practical setup for integration process. Importantly, to ensure proper alignment of the final probe, it is crucial to clamp both the micro-element and the optical fiber. This reliable and temporary clamping must be kept during hardening of an optical adhesive.

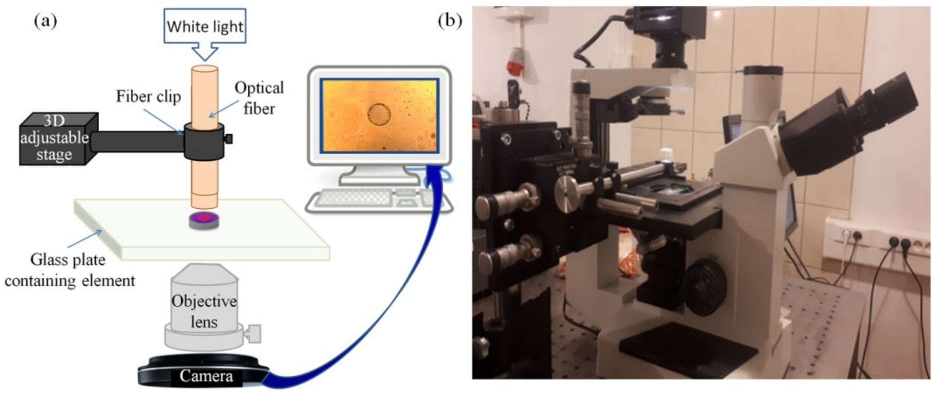

Figure 6.3 Assembly schematics (a) and practical setup (b) of integration process of the fiber-based vortex converter microprobe.

The system contains an inverted microscope (Science IVM 401, Bresser) which allows observing component from bottom side. The glass plate with the micro-optical components was placed into the inverted microscope. Above it, the selected single-mode optical fiber (depending on the operating wavelengths) is clamped to the custom-made holder connected to the precise 3-axis translation stage (Nanomax, Thorlabs), perpendicular to the microscope objective. The tip of optical fiber is dipped in UV-curable optical adhesive (NOA65, Norland). After curing adhesive has refractive index of 1.524, and has flat transmission spectrum curve near 100% in a wavelength range from 400 nm up to 1600 nm.

The optical fiber is positioned above the spacer component in such a way that their centers are aligned. The fiber was then pressed down slowly until attaining a good contact between two surfaces. A UV 100 W Mercury lamp is used for around 8 minutes for the final curing. During curing any movement will cause misalignment. After this fixing step, water was poured on glass plate over the integrated system for dissolving the water soluble glue used in the initial mounting spacer to microscope glass slide. The same techniques, is applied to assembling the nanostructured VPM to the integrated spacer-fiber so that a compact SMF-spacer-nVPM system was formed as an example in Fig. 6.4.

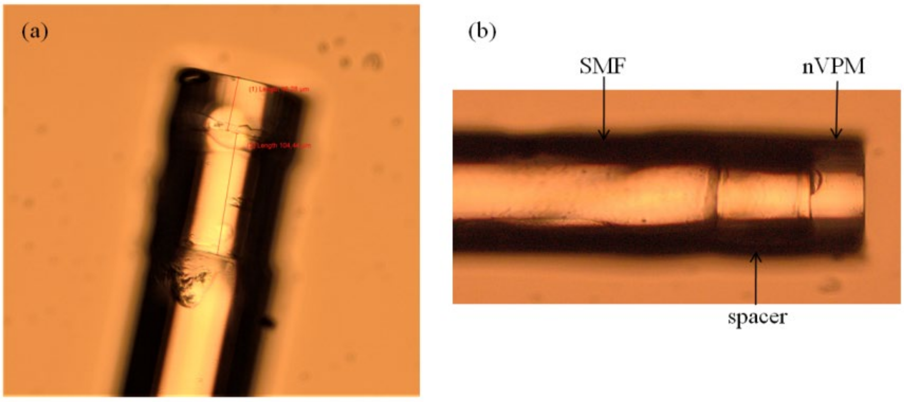

Figure 6.4 Examples of fiber-based vortex converter microprobe sample images under microscope.

6.2 Numerical investigations of the performance of the fiber-based vortex converter microprobe

The optical performance of the designed SMF-spacer-VPM systems have been verified numerically using the Fast Fourier transform Beam propagation method (FFT BPM) described in chapter 4.

The first set of computer simulations was conducted to investigate the properties of the bare optical delivery fiber and the result is represented in Fig. 6.5. For simulation fiber path having a core diameter of 4.3 μm and a length of 600 μm was assumed. Its core and cladding have refractive indices of n_{core}= 1.462 and $n_{cladding}$= 1.457, respectively. The input beam with a wavelength of 633 nm and diameter (defined at $1/e^2$ cut-off) of 4.3 μm was used in simulation. In order to ensure the effective work of the algorithm realizing FFT PBM, the simulation field along the optical axis (z-axis) was divided to 1 μm steps and to 0.1 μm steps in x and y perpendicular plane.

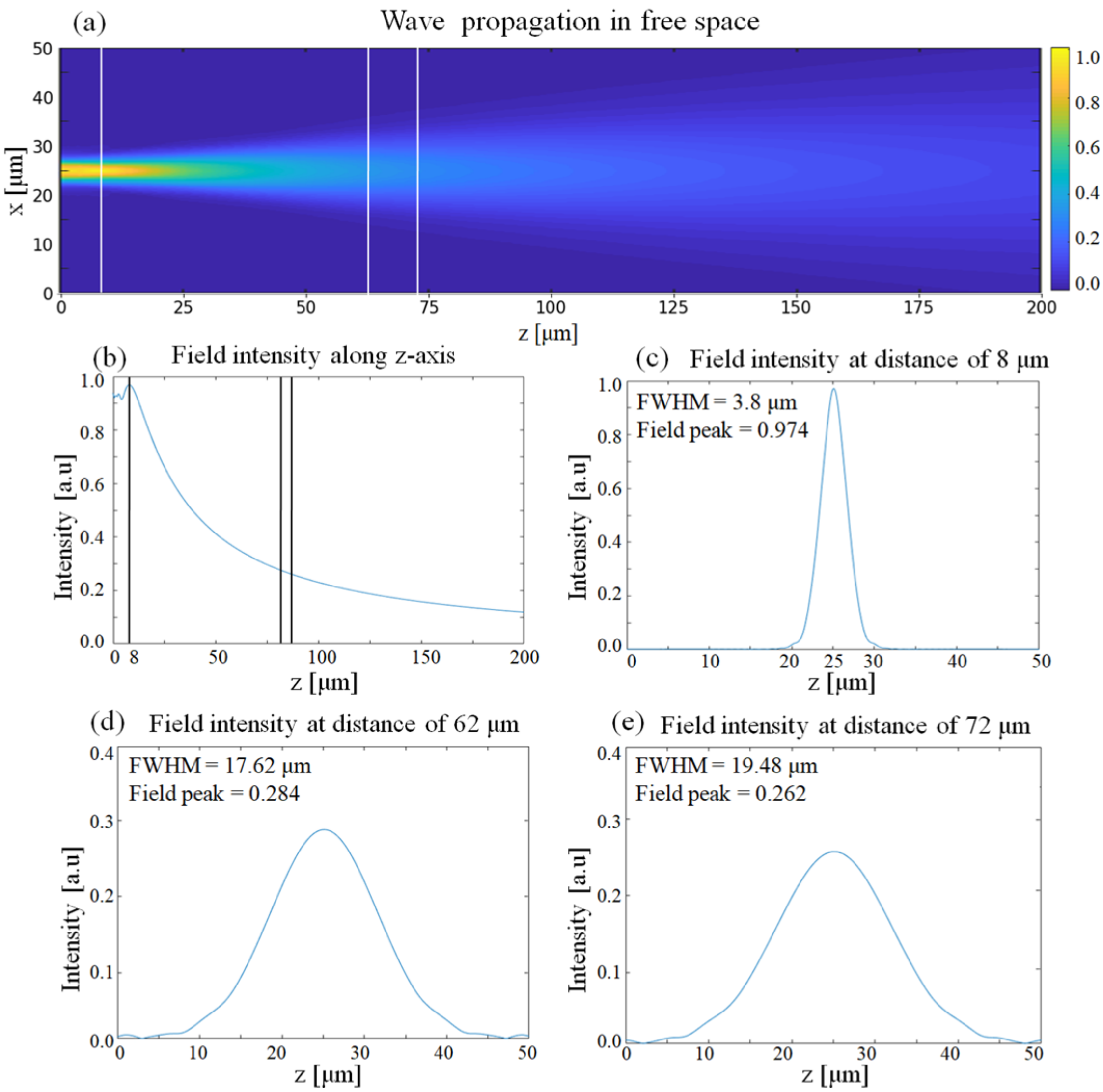

Figure 6.5 (a) Modeled beam intensity profiles emerging from the end of the SMF fiber in air. (b) Intensity profile of the beam propagating along the optical axis. (c-e). Intensity profiles of beam cross sections along z axis at distance form the fiber end at 8, 62, 72 μm, respectively.

The numerical calculations showed that the output beam waist at 8 μm from the end of the fiber is 3.8 μm FWHM. The size of the beam increases along the propagation axis. It can be seen from the Fig 6.5(a) that at the plane directly out of fiber, the beam spot is very small (~ 4 μm). In case of direct mounting nVPM to the end of the optical fiber, most of the energy illuminates only its minute area. As discussed in the previous Chapter about the beam size for illuminating the vortex structure, to generate good quality OVBs, the illuminating beam diameter should match the shorter diagonal of the VPM structure (~ 18 μm).

For the purpose of keeping proper distance between the VPM and fiber end, a piece of coreless fiber (spacer) was utilized. So the next simulations were performed for light propagating through a compact system of the mentioned fiber and 200 um spacer. As mentioned in the previous section, the spacer here is made of borosilicate NC21 glass having refractive index n_{NC21}=1.5243 at the operating wavelength of 633 nm. Other input parameters for the optical fiber are the same as per the previous simulation series. The conducted simulation results are presented in Fig. 6.6. It shows that the required length of spacer for expanding the light from fiber to attain a light spot with FWHM of ~ 18 μm should be around 85 μm.

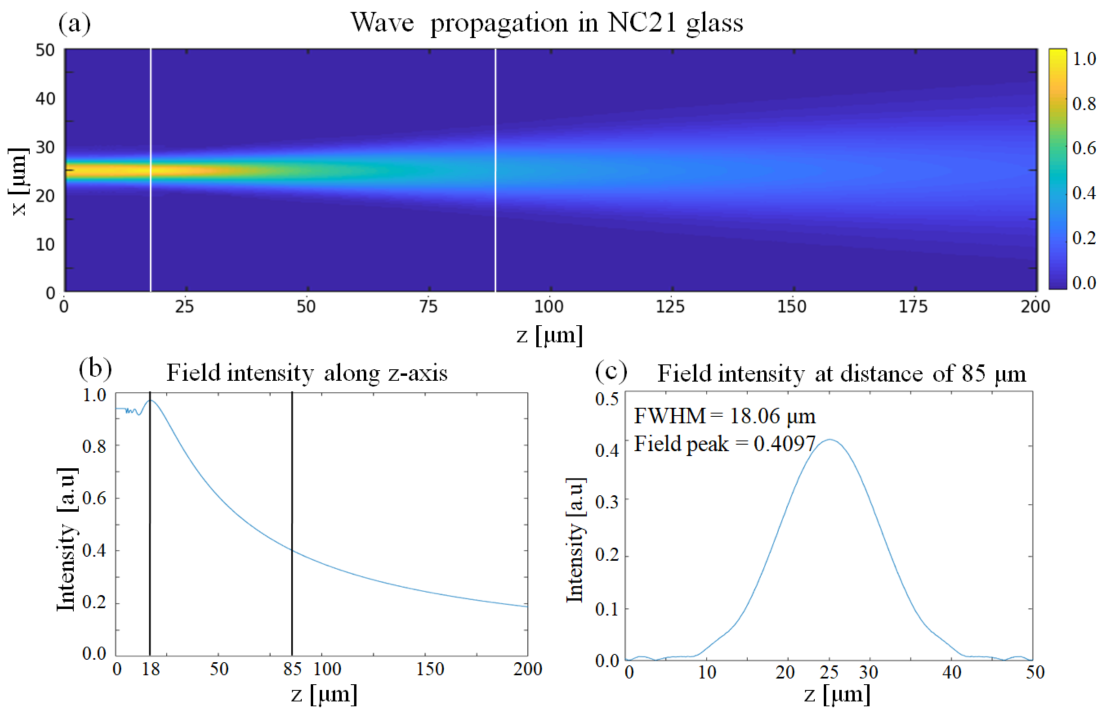

Figure 6.6 (a) Modeling beam propagation emerging from the end of the SMF in NC21-glass material (n=1.5243 at the wavelength of 633 nm). (b) Intensity of the beam propagating along the optical axis. (c) Field intensity along the diameter of beam cross section at working distance of 85 µm.

Base on the above simulation calculations, we have subsequently carried out the numerical investigations for a selected compact fiber-based vortex converter system (see Fig. 6.7). The design comprises of 600-µm-long fiber, 85-µm-thick NC21-glass spacer and a GRIN VPM. The VPM has diameter of 20 µm and thickness of 25 µm which, as followed explanations in Chapter 3, allows the generation of OVB with topological charge l = 1. Here the simulations were performed for both ideal continuous and actually realized binary nanostructured VPMs for a comparison. The binary nVPM was designed the same as the one studied in Chapter 5, which, according to EMT, reproduces the effective index distribution as the ideal continuous GRIN vortex phase mask. The spatially arranged nano-regions in the structure are made of two boro-silicate glasses, NC32 (n_{high} = 1.549 at λ_0 = 633 nm) and NC21 (n_{low} = 1.524 at λ_0 = 633 nm) as mentioned previously. Figure 6.7 depicts the scheme of simulations of the beam propagation through the fiber optics realization of the OVB generator. The presented results are for a plane located at 300 µm from end facet of the generator with assumed free space propagation.

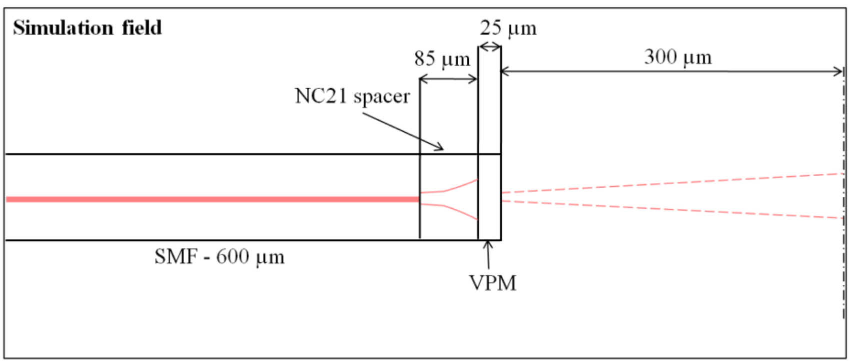

Figure 6.7 FFT BPM simulation scheme for the beam propagation through 600-µm-long optical fiber, 85-µm-thick spacer, 25-µm-thick nVPM and distance of 300 µm in free space.

Results of the simulation presented in Figure 6.8 shows intensity profiles and phase structure of the beam for the ideal continuous refractive index profile as well as the binary nanostructured designed VPM. All numerical modeling results confirm the formation of optical vortices in air in both cases of VPMs realizations. Indeed, the phase singularity characteristic is indicated by the doughnut-like intensity pattern with a clear dark central region. In both cases single arm on spiral phase structures indicates topological charge l = 1. Therefore, it is numerically proved that the designed fiber-based vortex converter microprobe should generate single-charge optical vortex beams.

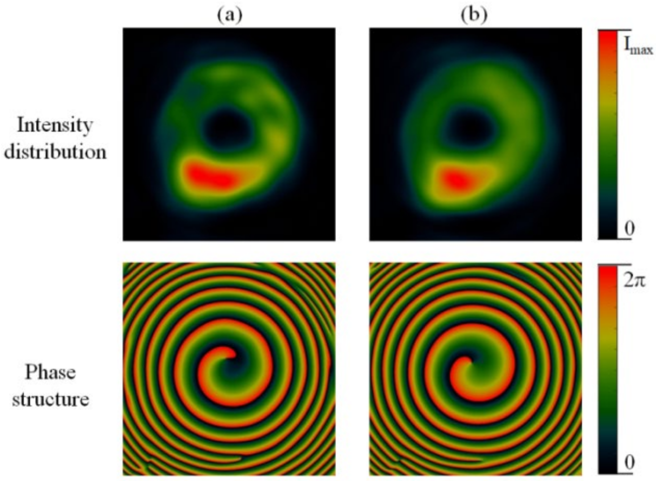

Figure 6.8 – Numerically simulated field and phase structure of the beam transmitted by fiber based micro-optical probe with an ideal continuous index (a) and binary designed VPMs (b) visualized in air at a distance of 300 μm behind the masks. The spacer and VPMs have thickness of 85 μm and 25 μm, respectively.

It should be noted that these numerical simulations also show non-uniformity of the intensity profile – some light localization. The wave-guide effect occurs because light propagates for relatively long distance inside GRIN mask as discussed in details in Chapter 4. To prove that the chosen spacer thickness is optimal, additional simulations were performed for the spacers with the thicknesses of 0, 40, and 120 μm while other parameters of the fiber-based vortex converter microprobe are kept the same. The simulations were conducted for ideal continuous VPMs, which simplifies simulations without sacrificing any meaningful details in results as can be seen in case of previous simulation. The results shown in Fig. 6.9 confirm that optimal thickness of the spacer equals of 85 μm.

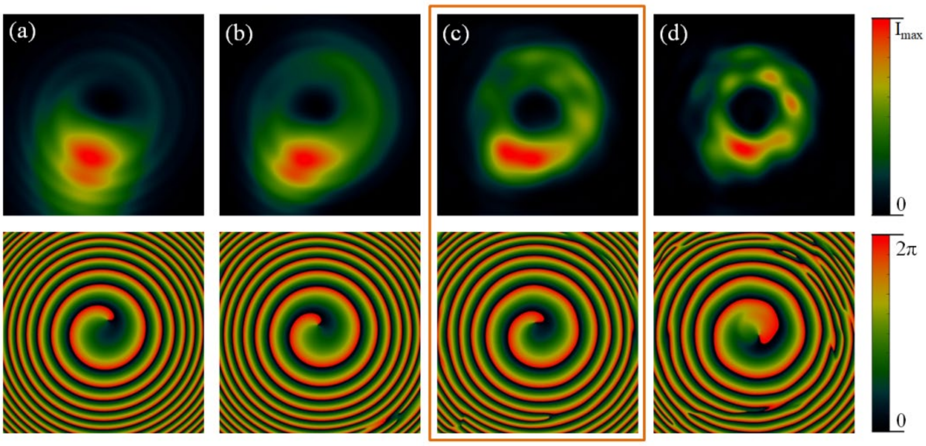

Figure 6.9 Numerically calculated field intensity (top row) and phase structure (bottom row) of the obtained OVBs using the designed fiber-based vortex converter. The results in a, b, c, d are visualized at 300 μm behind the nVPM, corresponding to four converter system with different thickness of the spacers - 0, 40, and 85 μm, respectively [63].

In practice, as in the discussion related to technological fabrication in Chapter 5, our facility has limitations in the accurate polishing of thin optical components for an exact thickness. The thickness errors are in range below of single micrometers. That means the actually integrated vortex-fiber probes do not consist all components having exact thicknesses as in the designed cases simulated above although they are well aligned integrations. Among integrated fiber-based vortex converter probes, we selected the best one which have the closest thickness values of the nVPM to the above theoretical calculations. The selected integrated probe consists of 80-cm-long SMF, 84-μm-thick NC21-glass spacer and 28-μm-thick nVPM. In numerical study, only thicknesses of the spacer and nVPM are varied to match with the actually selected probe while other input parameters are kept the same as per other previous numerical calculations. In addition, numerical simulations were performed for the fiber-based vortex converter microprobe immersed in air and water. The results presented in Fig. 6.10 and Fig. 6.11 are obtained at distance of 300 μm after the output end of the VPMs.

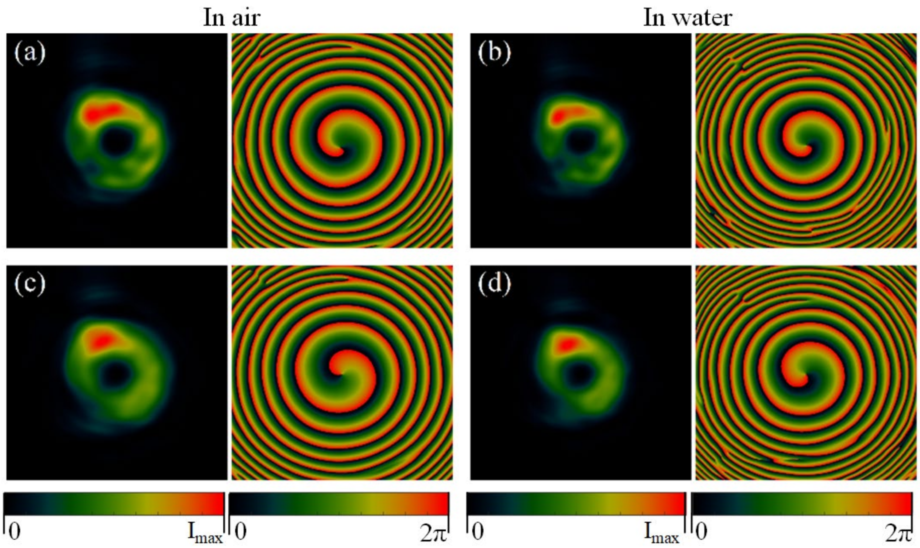

Figure 6.10 – Numerically simulated beam intensity and its phase structure for the beam transmitted through fiber-based micro-optical vortex converter with an ideal continuous index (a, b) and binary designed VPMs (c, d) visualized at distance of 300 μm from the converted end facet. The NC21 spacer and VPMs have thickness of 84 μm and 28 μm, respectively. Plots (a,c) present OVBs created in air (b, d) in water [63].

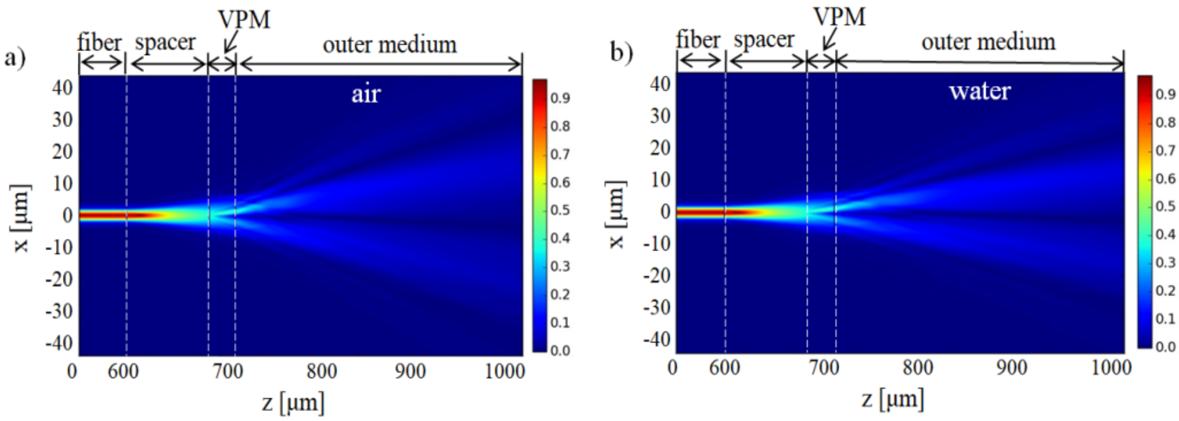

Figure 6.11 Modeled intensity of light propagation in the xz plane through the whole integrated fiber-spacer-vortex system up to 300 μm distance from the converter in air (a) and water (b) [63].

It can be seen that both designed probes with ideal continuous refractive index VPM and binary nVPM produce doughnut-like intensity patterns with a clear dark central region. The phase structures of these generated OVBs have single arms indicating the topological charge l =1. Moreover, the simulated OVBs generated by binary nano-structured VPM (in the top row of Fig. 6.10) is of similar in quality to the one generated by an ideal continuous VPM (in the bottom row of Fig. 6.10).Therefore, these simulation results predict that the selected fiber-based microprobe with the 28-μm-thick VPMs can converts the fundamental (Gaussian) beam into charge l = 1 OVBs at the wavelength of 633nm. In addition, Figure 6.10 also reveals lack of significant differences in results either in case of air or in water that means the optical performance of the designed microprobes are not affected by water. The optical performance of the probe is also confirmed by simulations of the beam intensity in the longitudinal plane of light propagation through the whole fiber-spacer-vortex system and then in 300 μm distance in air and water (see Fig. 6.11).

It is worth noticing that the numerical studies of OVB generation in previous chapters were performed for the plane wavefront of the beam at the input of the mask while here due to the usage of the optical fiber; the planar input beam is converted to the Gaussian beam. Fundamental mode (Gaussian) emerging from the fiber became a source for illumination of the VPMs. In a careful comparison with the vortex beams converted from a planar wave shown in Chapter 5, we can state nVPMs perform exactly the same for the Gaussian as well as planar wavefront beam.

6.3 Experimental verifications

In this section, I discuss the experimental study on optical characterization of the selected fiber-based vortex converter microprobe which includes an 84-μm-thick spacer and 28-μm-thick vortex mask integrated at the end of an 80-cm SMF ((SM600, Thorlabs)). The He-Ne laser with the central wavelength of 632.8 nm as for majority of the simulations was also used in experimental part. The utilized optical fiber provides an optical mode field diameter of 4.3 μm measured at this operating wavelength. The actual experimentally verified vortex mask and the investigated fiber-based vortex converter microprobe are shown in Fig. 6.12.

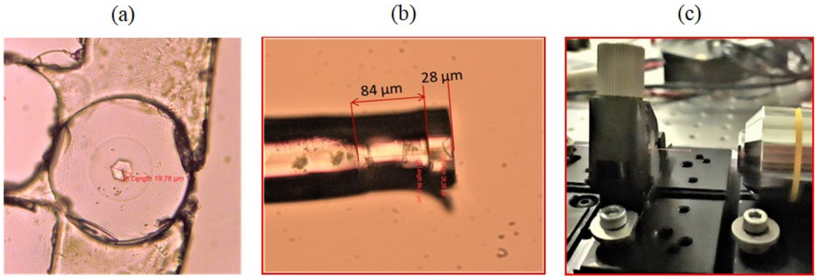

Figure 6.12 Fabricated nVPM image under microscope (a). Integrated fiber-based vortex converter images under microscope (b) and in experimental setup for its optical performance verification (c).

The optical performance of the integrated fiber-based vortex converter microprobe was characterized using three different experimental schemes are depicted in Fig. 6.13. They are employed for study the intensity distribution, phase structure and topological charge of the generated OVBs. In these experiments, the collimated red light emitted from He-Ne laser is coupled into the optical fiber to excite its fundamental mode. This was done with the usage of a high-magnification microscope objective Lens 1 (magnification 40, NA = 0.65). The fiber-based vortex converter probe is attached with a three axes high precision translation stage (Thorlabs, Nanomax) allowing precise manipulation of the fiber tip. The output beam after the VPM is collimated by a microscope objective Lens 2 (×10, NA = 0.25) and then depending on the property studied – the additional modification of the set-up were required. In all of the measurements, a CCD camera with a resolution of 1280 × 1024 pixels (Thorlabs, DCU224M) was used to record obtained results for later analyses.

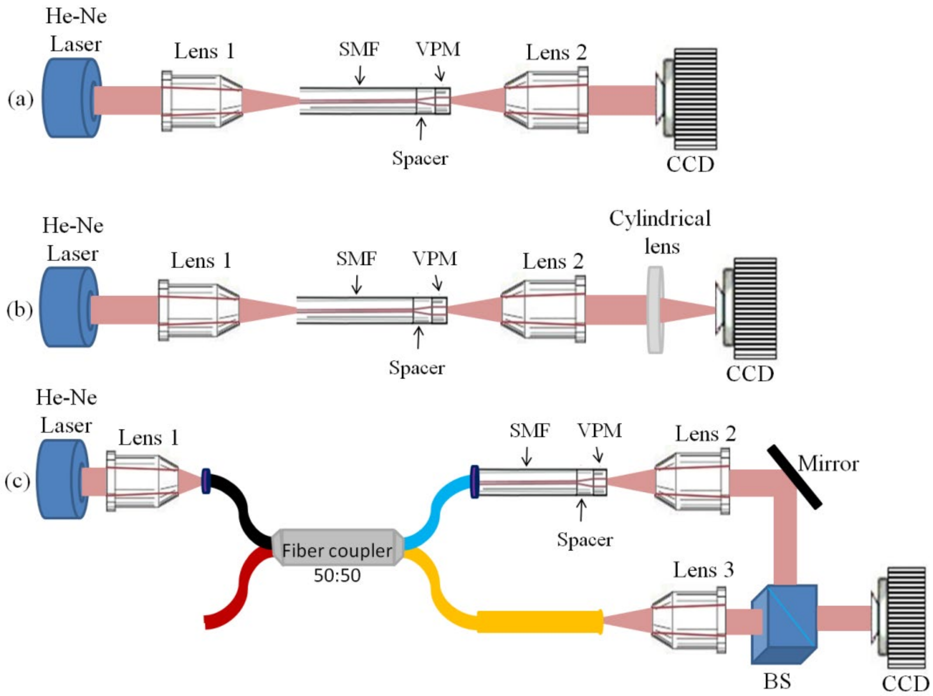

Figure 6.13 Experimental schemes for studying optical properties of OVBs generated by the fiber-based vortex converter microprobe: intensity distribution (a), phase structure and topological charge by astigmatic transformation technique (b) and by Mach-Zhender interferometer configuration (c).

In the first setup (Fig. 6.13(a)), the output collimated beam is directly recorded by the camera. The output surface of the converter (also output surface of nVPM) is positioned at around focal plane of Lens 2 while the camera is put at a distance of ~ 20 cm behind the objective lens. Then the distance between Lens 2 and the integrated converter end would be slightly adjusted to fill the whole imaging sensor of the camera.

The next setups depicted in Fig. 6.13(b) and (c) are used for study the phase properties and topological charge of the generated OVBs. The former one uses the astigmatic transformation technique to convert the vortex beam (Laguerre-Gauss modes) into Hermite-Gaussian modes. This is realized by means of addition of a cylindrical lens with a focal length of f = 15 cm. Here, the camera would record the transformed pattern of the formed OVBs at the focal plane of the cylindrical lens. The measurement setup in virtue of the schematic in Fig. 6.13(c) which is a Mach-zehnder interferometer provides interference between the vortex and the Gaussian reference beam. In here, the incident beam is equally divided into two parts with the use of a 50:50 fiber coupler (fiber tap). One of its output is coupled into the fiber-based vortex converter probe for OVB generations. The other one is collimated by Lens3 (×10, NA = 0.25) which is the reference beam in the interferometer. As a result, spiral and fork-like interferograms are obtained. The details of these detection approaches were discussed in Chapter 2.

The following part of this section will be devoted to analyses of the experimental results obtained with above mention measurement techniques. Now, I would start with the optical characterization of the selected fiber-spacer-vortex converter sample in a free space. The experimental results are represented in Fig. 6.14. Figure 6.14(a,b) depict intensity profile of the beam cross-section and its horizontal as well as vertical intensity profiles obtained from experimental setup in Fig. 6.13(a). It shows a visible doughnut-like shape intensity pattern with a clear dark central region indicating the singularity of the converted beam.

Other images in Fig. 6.14 present results for studying phase structure and topological charge of the converted OVBs. Initially, with a quick check by astigmatic transformation of the generated OVB (see Fig. 6.15(c)), we obtained only one dark stripe located between two distinct bright elongated regions on the pattern. It indicates the generation of OVB with a fundamental topological charge (l = 1). This is confirmed by interferograms obtained from Mach-Zehnder interferometer (see Fig. 6.14(d)). The fork-like pattern has one additional fringe coming out from the central zero-intensity region as depicted in Fig. 6.15(e), indicating the axial singularity as well as topological charge l = 1. Equivalently, the collinear interference measurement results in a spiral structure with single arm which agrees with the above results. Our experimental results are well matched with the numerical prediction as discussed above and proved that the integrated fiber-based vortex converter system allows converting Gaussian beam at 633 nm wavelength into an OVB with topological charge l = 1in air.

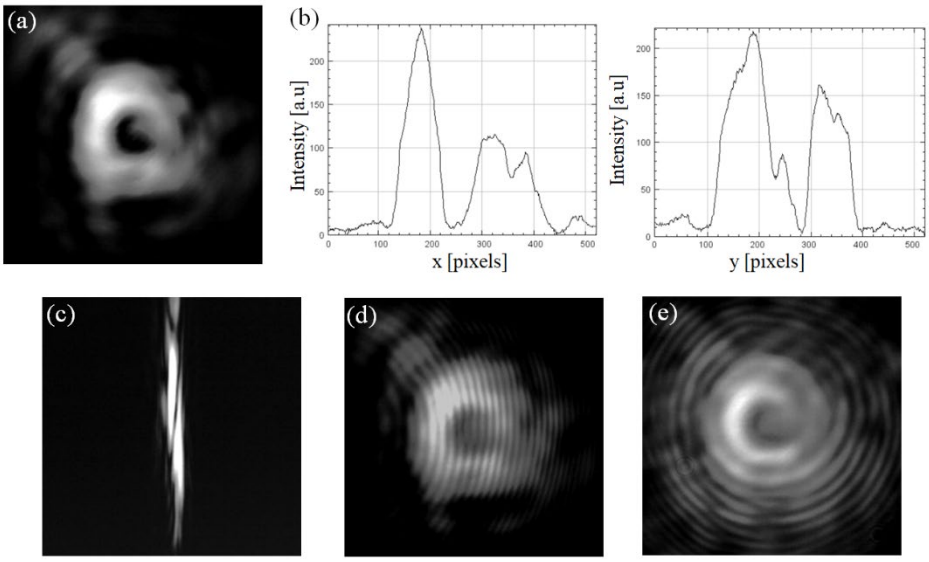

Figure 6.14 Experimental characterization of the selected fiber-based vortex converter sample in air: (a) donut-like pattern of intensity profile of the output beam cross-section; its astigmatic transformation(b); fork (c) and spiral (d) interference patterns obtained in Mach-Zehnder interference configuration indicating the phase singularity and topological charge l = 1.

However, the fabricated nVPM used for the selected converter system has a thickness of 28 μm, which is slightly thicker than the theoretically required nVPMs (25 μm) in order to convert incident beam at 633 nm wavelength into fundamental-charge OVBs. However, both experimental and numerical simulation results as analyzed above confirmed the formation of OVBs with topological charge of l = 1. The difference of 3 μm in the thickness is a result of the technical limitations in the accuracy of cutting and polishing. This issue together with the wave-guide effect has contributed to the non-perfect intensity distribution of the generated OVBs.

The subsequent experiments studies optical performance of the fiber-based vortex converter probe immersed in water, the microprobe is exactly the same as the one used for the previous measurements in air. The experimental results of the experiment are presented in Fig. 6.15. In particular, Fig. 6.15(a) shows the doughnut-like intensity profile of output beam. There is zero-intensity at its center. From interferometer experiments, existence of phase singularity is confirmed by the central bifurcation of the fringes forming fork-like interference pattern as shown in Fig. 6.15(c). The above confirms OVB generation in water. To verify the value of the obtained OVB the interference measurement were complemented with the astigmatic transformation of the generated OVB (depicted in Fig. 6.15(b). The results show that the generated OVB has a topological charge of l = 1 since there is only one dark stripe in astigmatic transformed pattern as well as one additional fringe in fork structure and single spiral arm in spherical wavefront interference pattern. The experimental results agreed with numerical calculations in Fig. 6.10 (b,d) for the case of ideal (fully continuous) as well as binary VPMs.

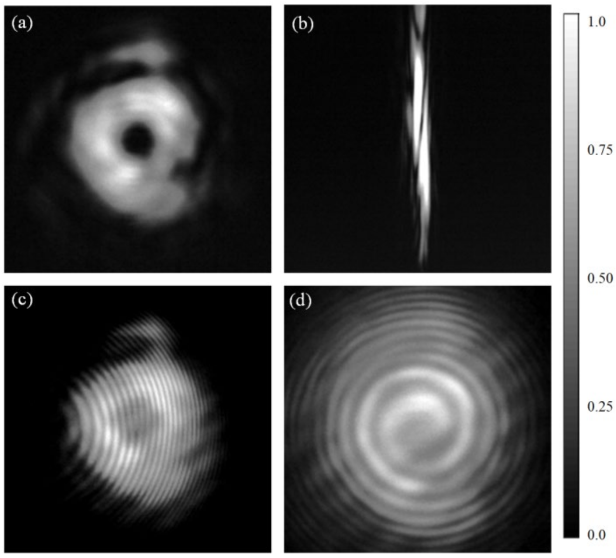

Figure 6.15 Experimental characterization of the investigated fiber-based vortex converter probe in water: (a) donut-like intensity profile in the output beam cross-section; (b) its astigmatic transformation; the fork (c) and spiral (d) interference patterns obtained in Mach-zehnder interference configuration indicating the phase singularity and topological charge l = 1.

6.4 Study on the effect of the polarization and the delivery fiber bend on performance of the fiber-based vortex converter microprobe

In this part, series of numerical calculations and experiments were conducted to verify the effect of orientation of linear polarization of the input beams and the bend of the delivery fiber on the performance of the converter. The results show that there is negligible change in the polarization state due to the fiber bending. Firstly, it should be noticed that the change of the polarization state of the input light will not affect the main property of the vortex beam. The polarization of the scalar vortex beam generated by VPMs is the same as that Gaussian beam which impinges the mask. It is because the designed and fabricated VPM here is a scalar vortex generator as discussed in detail in Chapter 5 and our previous studies showed marginal birefringence in the nanostructured fiber [192]. The formation of optical vortex beams is due to the azimuthal modulation of the refractive index in the nVPM, which results in the phase variation following the azimuthal angle. The mask is made of isotropic glass materials; thereby there is no induced mechanical stress in the mask. That means the mask would replicate polarization of the incident beam. The internal structure of nVPM has low short range order of the nanorods and the rods are round shaped, which means that there is no geometrical reason to favor any state of the light polarization.

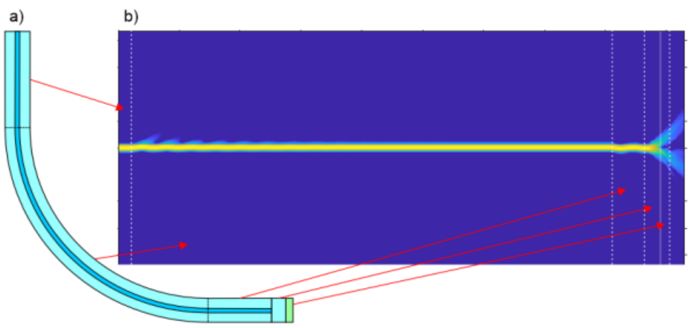

Figure 6.16 Studying scheme: (a) bent fiber, (b) distribution of light intensity in the fiber, the cross-section in the plane of the core.

Secondly, the scheme in Fig. 6.16 is introduced for studies on the insensitivity of the OVBs generated by the fibe-based vortex converter microprobe to the bending of the light delivery fiber. In these investigations, the fundamental mode is used to excite the fiber. Then light propagates in the bent fiber whose bent path has a radius *r* and a length of 1/4 of a circle. Then the light propagates in a short section of a straight fiber path with the spacer and VPM at the end.

The results represented in Fig. 6.17 show that the bend induced phase shift and phase slope, but this shift of the fundamental mode within the fiber core have a negligible effect on the quality of the generated OVBs. Only with a very strong bending (very small radius $r < 1$ mm), a change in light intensity could be observed due to bending losses inside the fiber. In this case, the centre of the vortex is slightly moving and the phase changes are also minor but still maintain their spiral character as depicted in Fig. 6.17(g). The shifting distances of the vortex centre observed when various bending radius is applied are shown in details by the graph in Fig. 6.17(a).

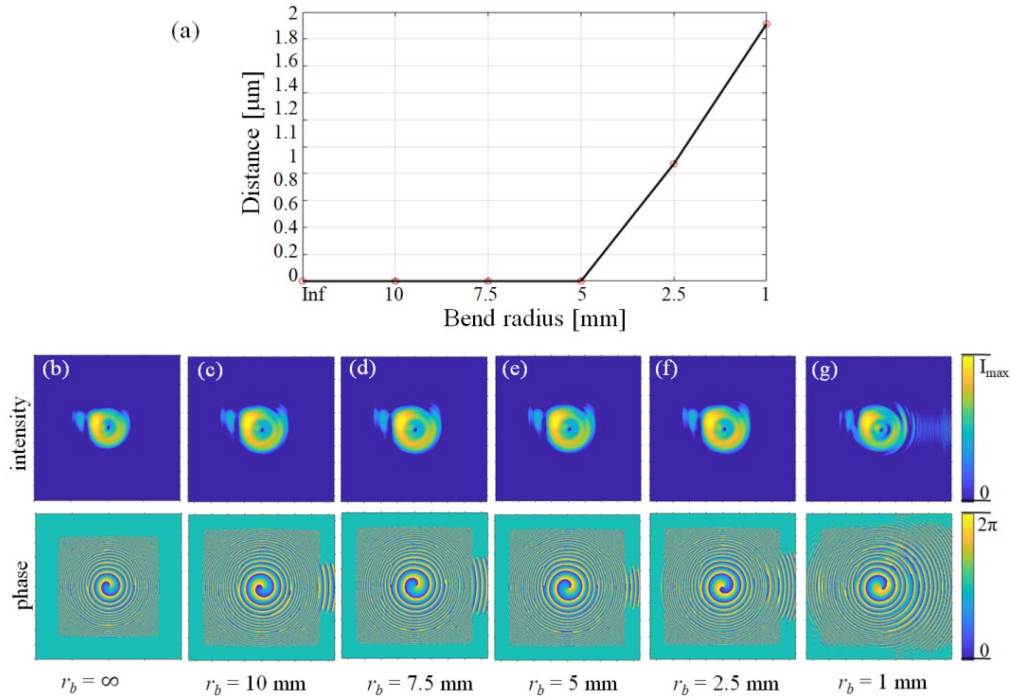

Figure 6.17 (a) Relative shift distance of the vortex centre as a function of the fiber bending radius *r*. (b-g) Numerical results for studying the influence of the fiber bending on the OVBs generated by the fiber-based vortex converter probe. Light intensity distributions and phase structures are visualized at the distance of 200 μm from the output surface of the nVPM.

6.5 Application of the microprobe for excitation of OAM modes in anti-resonant fiber

In addition, to verify the performance of fiber-based vortex converter micro-probe, we did experiments to excite the OAM mode (vortex beam) in anti-resonant (AR) fiber using this particular integrated converter microprobe. For that purpose, we have added an nGRIN lens of the probe to match the numerical aperture (NA) between the vortex generator probe and AR-fiber. The schematic of the developed microprobe is shown in Fig.6.18.

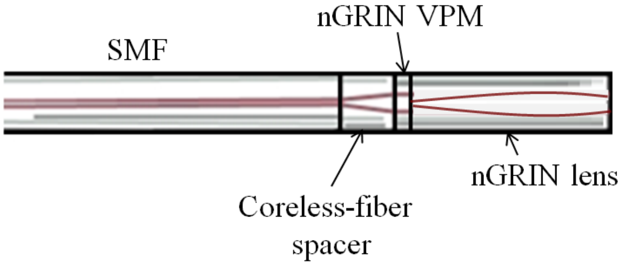

Figure 6.18 Schematic representation of the fiber-based vortex converter microprobe with nGRIN lens at the end.

The integration process was done manually using the same active alignment technique as discussed in Section 6.1. Here, the fiber-based vortex converter probe consists of a 41-µm-thick nVPM and a 610-µm-long nGRIN lens integrated at the end of a single-mode fiber. Since both components have flat surfaces and they are very compact and were directly integrated with a single-mode fiber to create a robust and alignment-free, easy-to-manipulate fiber-based generator of vortex beams. The performance of such a developed microprobe in generation of vortex beams was studied numerically as well as experimentally and reported in [64]. The study results are represented in Fig. 6.19.

The results demonstrated that the all-fiber vortex converter transforms a Gaussian beam into an optical vortex beam with topological charge l = 1 at wavelength λ = 980 nm. Moreover, we also proved that by changing distance between the fiber probe and the output plane we are able to reduce or enlarge the diameter of vortex without additional optical systems. It is worth noting that the fiber-based focused-vortex converter probe has a long working distance and the vortex beam after focal plane diverges slowly. That means the fiber-based vortex converter allows excitation of optical vortex modes in AR fiber.

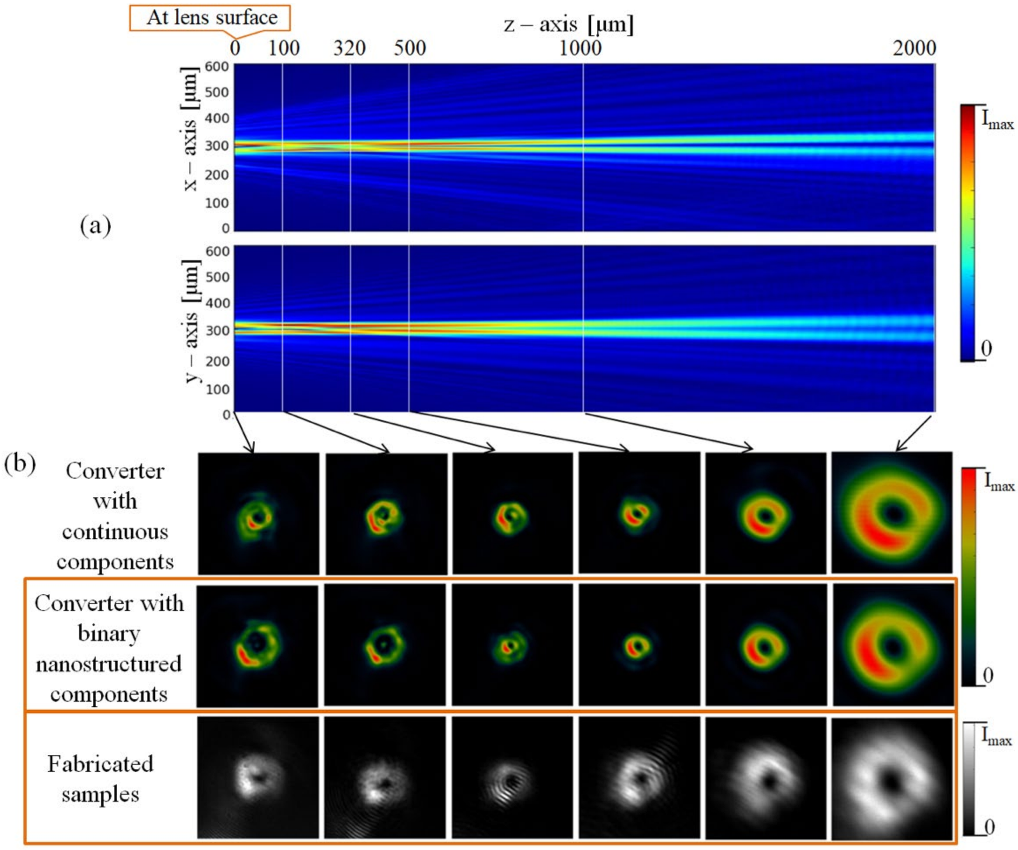

Figure 6.19 Intensity distribution of generated vortex along optical axis in free-space (a) modeling of propagation of beam along optical axes Z - cross section for XZ and YZ planes are presented, (b) intensity distribution at various distances from end face of the fiber-based vortex converter: modeling results for ideal continuous gradient index and nanostructured, experimental results for tested systems.

6.6 Summary

In this chapter, I presented in details the fabrication process of the novel fiber-based vortex converter microprobe as well as numerical and experimental results of its optical performance. The integrated probe includes an SMF path operating at the 633 nm wavelength, 84-μm-thick NC21-glass spacer and 28-μm-thick nVPM at the fiber end.

Both experimental and theoretical verifications done in this research confirmed that the fabricated fiber-based vortex converter probe efficiently converts fiber-guided fundamental mode into OVBs with single topological charge $l = 1$. It should be stressed that because of its gradient index principle, the integrated beam converter will maintain its optical performance in any transparent media including gas and liquids. Such a property is unique and for the first time reported for fiber-based systems providing opportunity to use the same component in different external environments.

It should be noticed that using the same nVPM component we can easily obtain OV beam with opposite sign ($l = -1$), however it requires to reassembly the fiber vortex converter. For this purpose it is enough to flip input and output facets of the nVPM in the fiber system. Similarly, it is straightforward to change a charge of the generated OV. In this case a longer nVPM has to be mounted in the fiber system. The thickness of this longer mask (D) is a multiple of d: $D = l \times d$, in which l is expected charge of the OV and d is the thickness of the nVPM for generation of OV with charge $l = 1$.

Our work confirms the feasibility of using a sequential combination of nanostructured gradient index micro-optical components having different functionalities in one optical system and still maintaining the compatibility with the optical fiber technique. One of the envisioned applications of the fiber-based vortex converter microprobe could be the optical trapping and a particle manipulation experiments in liquids. In such an application, the mircoprobe should dramatically simplify the experimental set-ups. Since attenuation of the fiber-based micro-vortex converter is very low and it is all glass made with high laser damage threshold. These properties open up perspectives for use this system for laser processing and ablation with structured beams including e.g. micro-drilling and surface structuring with twisted holes and pillars, respectively, as well as excitation of modes with orbital angular momentum in optical fibers. In addition, the nVPM can be considered for development of all-fiber laser vortex beam source, as it can be easily integrated with fiber laser resonator thanks to flat surfaces, rigid construction and overall compatibility with the fiber technology.

Chapter 7. Tailoring chromatic properties of nGRIN micro-optical components

In the previous chapters, I presented the concept of the nanostructured GRIN VPM and demonstrated its ability in the generation of micro-optical vortex beams. However this kind of nVPM is designed only for a monochromatic incident beam with a certain wavelength. To a considerable extend, in here a new nGRIN VPMs with achromatic properties has been proposed. It can generate “white-vortex beam”, which is a very vibrant subject in field of singular optics. To begin with, in the first section of this chapter, I will present the successful development of microlenses achromatically corrected in near-infrared part, reported in [65]. The optical performance of the microlens was numerically as well as experimentally verified. Research shows that the standard fiber drawing technology can be successfully applied to the development of achromatic gradient index microlenses by means of internal nanostructurization. These gradient index microlenses can achieve similar performance to standard aspheric doublets, while utilizing a simpler, singlet element geometry with flat surfaces. Furthermore, additional theoretical and numerical study of an achromatic vortex mask was carried out which will be discussed in details in section 7.2. For the vortex mask development, the appropriate pair of in-house-synthesized soft glass materials has been specified. The glasses are mechanically and thermally matched for joining in drawing process. Their refractive index difference needs to be appropriate in technically achievable thickness. Then, its nano-structure with an azimuthal gradient index profile is designed using a combination of the simulated annealing method and the effective medium approximation theory. The achromatic character of optical vortices generated with the designed VPMs is numerically verified by the usage of the aforementioned BPM method. Furthermore, already optimized white-vortex binary mask structure has been ready for fabrication in near future.

7.1 Monochromatic and achromatic properties of lenses

This section is devoted to an introduction of functionality of achromatic correction of a new-designed nGRIN microlens. The detail discussions of this work were reported in [65]. The successful creation of nGRIN microlenses having achromatic properties by using the nanostructurization technique opens up a possibility of exploiting it for the development of white-vortex components. Thus, I will not go into detail in demonstrating of optical behavior of the achromatic microlens. Instead, the concept and theoretical analysis will be more emphasized. This will provide the necessary knowledge to understand the white-vortex concept.

7.1.1 Concept

The standard lenses or singlets are typically monochromatic which means the lens has different focal lengths for different operating wavelengths (Fig 7.1(a,b)). This manifests as a chromatic aberration in imaging and is caused by the dispersive nature of glass materials.

The achromatic lenses perform with negligible chromatic aberrations in a wavelength range (see Fig 7.1(a)). This is highly beneficial behavior for imaging process and optical manipulations. Recently, the chromatic aberration can be elimited by optimizations of the lens’s shape, but it is very limited approach for single lens elements. Feasible common approaches have applied on development of achromatic lens mostly rely on combination of multiple lens elements or materials. In the former case, typical solutions include doublet [193] and hybrid diffractive-refractive achromatic lenses [194] whose schematics are presented in Fig. 7.1(c) and (d), respectively. In the later one, the GRIN lenses with refractive index changing axially [195] and radially [196] have been proposed as shown in Fig. 7.1(e) and (f), respectively.

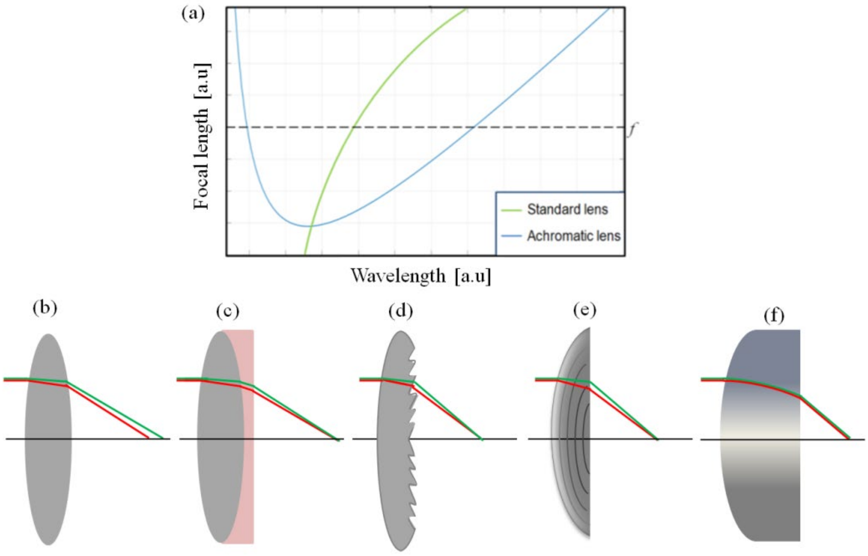

Figure 7.1 (a) Example of mono- and a- chromatic behaviors of the lenses. Schematic of standard singlet lens (b) and achromatic lenses developed by several approaches: (c) doublet lens, (d) hybrid diffractive-refractive achromatic lens, (e-f) achromatic refractive GRIN singlet lens. This figure is based on [65].

Those approaches are successfully applied for achromatic macro-lenses such as microscope and camera objectives. However, it is more difficult or even impossible for obtaining achromaticity with micro-size lenses because of technological limitations. Additionally, fabricated achromatic micro-lenses with at least one non-flat surface are difficult to be integrated with fiber optic systems. Therefore, there is a need for reliable approach to fabricate micro-sized, all-flat-surface lenses.

In several recent reports, we have successfully demonstrated possibilities of shaping flat-surface GRIN micro-lenses using the modified stack and draw method [52,54,59,182]. This method exploits the nanostructurization technique and EMT to create an arbitrary refractive index distribution defining different optical behaviors of the micro-optical components which were described in detail in Chapter 3. The nGRIN microlens which is constructed from spatial arranged nanorods made of two thermal-matched glasses with high (n_{high}) and low (n_{low}) refractive indices (Fig. 7.2(b)). The nanostructured microlens with effectively refractive index distribution mimicking the ideal continuous one is shown in Fig. 7.2(a).

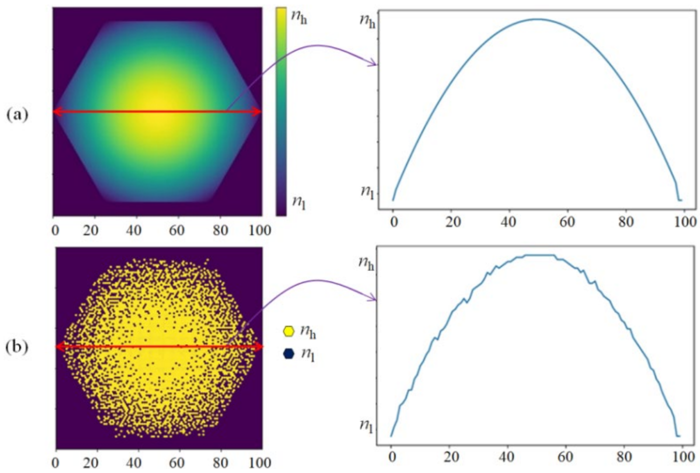

Figure 7.2 (a) ideal continuous GRIN microlens and the corresponding designed nanostructured lens (b) with corresponding refractive index profiles along the center line of the lenses.

The refractive index distribution along the line crossing through the optical axis of the GRIN lens has a parabolic shape. It decreases from its center with the highest value – n_h to its edge with the lowest value – n_l. According EMT described in Chapter 3, the effective index of an intermediate region in the nGRIN lens with a given filling factor parameter a of low index glass can be given as:

$$n_i = an_l + (1-a)n_h. \quad (7.1)$$

The refractive index along the line crossing through the nGRIN lens's optical axis is given by a radial dependence formula [199]:

$$n = n_l\left(1 - \frac{G}{2}r_j^2\right) \quad (7.2)$$

where r_j depicts the radial distance from the optical axis of the lens. G defines a gradient constant depending on the refractive index contrast between two glass materials ($\Delta n = n_h - n_l$) and the radius of the lens structure:

$$G = \frac{2\Delta n}{n_l r^2}. \quad (7.3)$$

And hence we obtain the focal length f predicted for the designed binary-nanostructured microlens as a function of its thickness (d) as below [199]:

$$f = \frac{1}{n_l\sqrt{G}\,\sin(d\sqrt{G})}. \quad (7.4)$$

Equivalently, the lens' working distance which is also known as the back focal length can be calculated by the following formula [199]:

$$WD = f\cos(d\,\sqrt{G}). \quad (7.5)$$

It is obvious that the focal length and the working distance of the designed nGRIN micro-lens vary for different thickness values. That means we can cut the structure into a suitable thickness for any desirable focal lengths. However, these lenses exhibit monochromatic properties. They perform different focal length f and working distance WD at different wavelengths.

We employed this innovative fabrication approach to develop achromatic nanostructured GRIN microlens with flat-parallel surfaces. Our achromatic lens has the same focal length and WD for two different wavelengths. It will be realized by incorporating correct glasses into the design. It is obvious that each pair of glass materials has certain profile of the refractive index difference changing with the wavelength. According to Eq. (7.3-7.5), if there are points at which for different wavelengths the refractive index difference are the same, the focal length and working distance of the fabricated nGRIN lens will be the same. For a carefully analysis, our achromatic nGRIN lenses can be obtained by quadratic function of refractive index difference with respect to wavelengths. In comparison to current achromatic GRIN singlet macro-sized lens designs which are not flat on both surfaces and not suitable for fiber systems [195,196], our lens is a significant advancement.

7.1.2 Proof of Concept

For a proof-of-concept of the achromatic nanostructured micro-lens, we have used a borosilicate high and low refractive index glass pair. They was synthesized in-house and labeled NC34 and NC21A, respectively [65,180]. These glasses satisfy the rheological and thermal matching conditions as required in Chapter 3. Fig 7.3 presents material dispersion characteristics for those glasses and calculated effective focal lengths of the achromatic GRIN microlens made of these glasses in the wavelength range of 0.5-2.0 µm. It can be seen that the nGRIN micro-lens made of theses glasses has the same focal lengths for pairs of wavelengths in the consider range. That means this lens is achromatic theoretically.

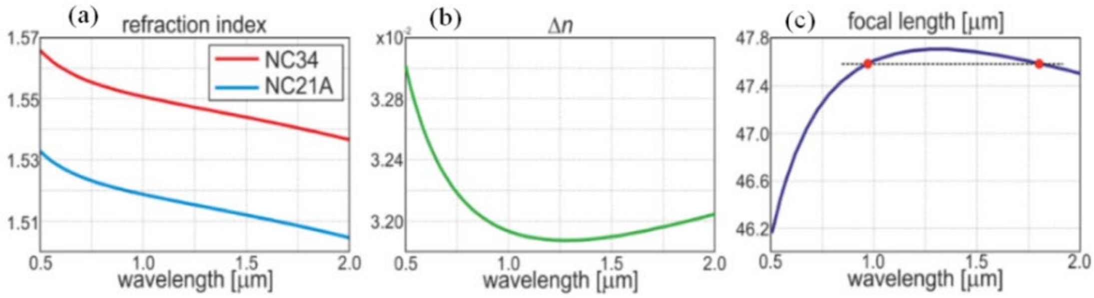

Figure 7.3 Dispersion properties of two used borosilicate glasses NC21A and NC34 ((a) refractive index curves for the glasses; (b) their refractive index difference and (c) the calculated focal length of the corresponding GRIN lens for the range of wavelength from 0.5 to 2.0 µm [65].

Starting with parameters beforehand calculated analytically, we conducted numerical modeling task to design and optimize the nano-structure of the achromatic nGRIN microlens using NC21A and NC34 glass nanorods. The final binary structure of the lens is represented in Fig. 7.4(a). There are 7651 boro-silicate glass nanorods used to form a binary hexagonal lattice. Those rods are well arranged to produce the effective refractive index distribution similar to the ideal continuously parabolic GRIN lens. The structure has a long diagonal containing 101 rods. The designed binary structure is fabricated using a modified stack and draw method as described in Chapter 3. The final fabricated lens structure with a diameter of ~20.0 µm has been verified with SEM images as depicted in Fig. 7.4(b). The lens structure is surrounded by low index glass to form a micro-optical component with a standard size of 125 µm. The pitch length measured for the created GRIN micro-lenses is 309 µm at the wavelength of 1550 nm. In this task, a fabricated nGRIN lens samples with a 36-µm thickness (0.12 pitch) has been selected for numerical and experimental investigation.

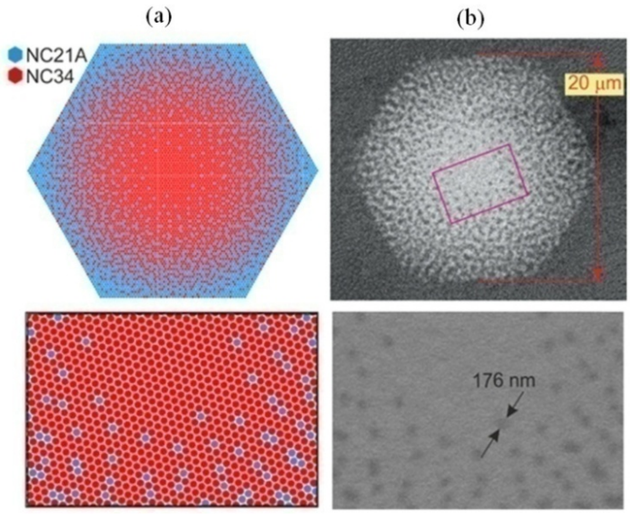

Figure 7.4 Desinged (a) and fabricated (b) binary nGRIN microlens for achromatic functionality performance and their corresponding magnified parts for a comparison [65].

Figure 7.5 shows the schematic of measurement setup used for experimentally characterizing the achromatic behavior of the fabricated nGRIN micro-optical lens. In this setup, the microlens was attached to a three axis translation stage (Thorlab, nanomax) for position adjustment in all of the experiments. The translation stage movement was controlled by a computer. In order to study the focusing and achromatic properties of the selected microlens for a wide band of light, we used various continuous-wave lasers, with corresponding wavelengths in the visible and near infrared bands: λ = 532, 658, 850, 980, 1310 and 1550 nm. The light beams emerging from those sources were collimated before going through the investigated lens. The output results were recorded by an imaging system including 40 × microscope-lens and a camera. For visible range and infrared up to 1.2 um, a regular monochromatic CCD camera was used. For longer wavelengths, a CCD camera with two-photon converting diaphragm was used. The distance between the camera's surface and the microscope was chosen in each measurement as such to keep the size of the structure image on the CCD camera constant. The cross-sectional intensity profiles of the beam propagetd through the lens were captured on the CCD camera at different distances from the lens end facet, incrementing with a step of 1 μm and a position accuracy of 0.1 μm.

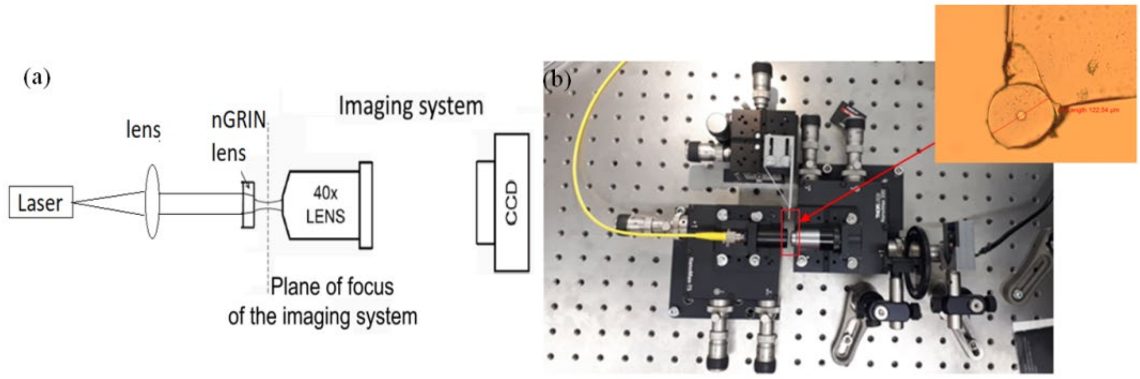

Figure 7.5 Schematic of optical setup (a) and its realization (b) for the experimental study on optical characterization of the achromatic nGRIN microlens.

After measurement, the series of taken images were analysed (Fig. 7.6(a,b)). The analysed intensity profiles in term of value of the beam diameter (FWHM) were combined in one plot. The plot of the FWHM of the beam cross-sections at difference distance along the light propagation axis is presented in Fig 7.6(c).

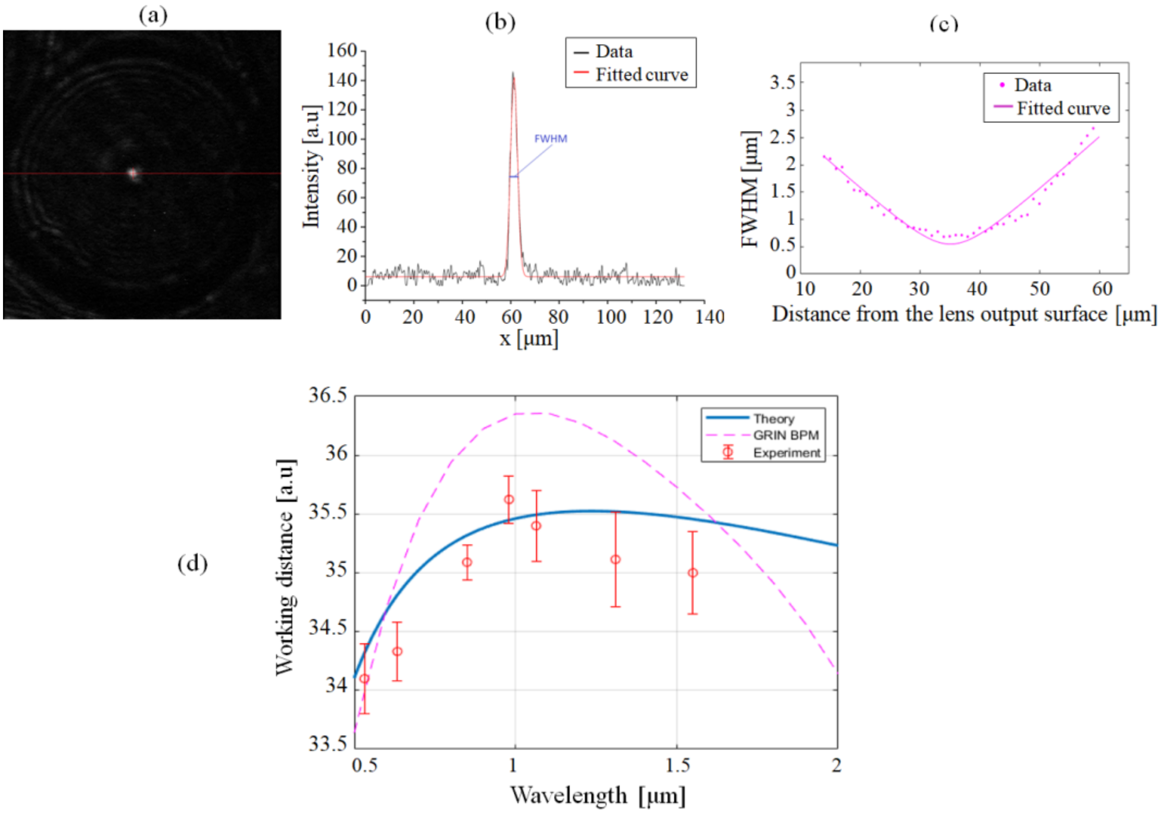

Figure 7.6 (a) Example of recorded intensity images and (b) its calculated FWHM. (c) The calculated FWHMs at difference distance along the light propagation axis for one wavelength (one light source). (d) Working distance parameters of the studied nGRIN micro-optical lens as functions of wavelength calculated by theoretical formula (the blue line), numerical simulations (the pink dash line) and experimental results (the points).

As a result, we could determine the effective working distance of the investigated nGRIN lens by looking at the position of the focal plane for each wavlength - the value of FWHM would be at a minimum. Experimental results in from Fig. 7.6(d) show that the beam spots at focal planes have FWHM values in the range of 2.1 – 4.1 μm for the wavelength range from 532 nm to1550 nm. The longitudinal FWHM profiles of the transmitted beams at different wavelengths beam indicate the axial achromatic behavior of the lens. In particular, the working distance of the investigated lens is the longest (35.6 μm) for the wavelength of 980 nm and reduces until 34.1 μm for both shorter and longer wavelengths as shown in Fig. 7.6.

It can be seen that both theoretical and numerical calculations for the performance of the same nGRIN microlens also verifies its achromatic properties. The numerical simulations were implemented using the Beam Propagation Method – FTBPM – described in Chapter 4. The assumed input parameters of all simulations correspond to those for the experimentally measured sample. The working distances *WD* of the lens was theoretically calculated according to Eq. (7.5). However, the dependences of the investigated lens's *WD* on wavelengths in these two cases are much different from each other. In addition, the measurement results are much more like the theoretical calculations rather than the simulated results. This issue can be caused by several factors. Firstly, the numerical simulation with BPM method does not consider the diffusion at the boundary of nanorods as discussed in Chapter 3. The diffusion smothers out the boundary transitions resulting in the more continuous change of refractive index of the nGRIN lens as assumed in the analytical equation (7.5). Secondly, the simulations also do not apply the high-order Padé approximation [36] on the transverse direction of the beam which is so important for the binary structure. Therefore, the diffusion between glasses as well as high order Padé approximation should be taken into account in BPM simulation to improve its accuracy.

7.1.3 Summary

In this section, a concept of nGRIN microlens with achromatic properties in visible and near-infrared spectral windows has been proposed and proved. The development of this kind of microlens is based on the EMT and nanostructurization. The achromatic microlens with flat-parallel surfaces has been designed and fabricated using two types of in-house made boro-silicate glasses (NC21A and NC34). This pair of glass provides the quadratic change of the difference of their refractive indices following wavelengths. This resulted in the realization of achromatic GRIN microlens. The optical performance of the microlens was numerically and experimentally verified. The fabricated nanostructured lens sample with a thickness of 36 μm (0.12 pitch) and a diameter of ~20 μm was investigated by the use of multiple laser sources with center wavelengths at 532, 658, 850, 980, 1310 and 1550 nm. Measurements revealed that working distances of the tested lens are in the range of ~ 34.1-35.6 μm for the considered wavelength range. In particular, the lens shows the longest working distance of 35.6 μm at 980 nm wavelength and for both shorter and longer wavelengths, shorter working distances were observed. This proved that our nGRIN microlens introduce similar optical performance to standard aspheric doublets, but utilize a simpler, singlet element geometry with flat surfaces and have a microscopic size.

The successful development and fabrication of achromatic singlet component of presented properties motivated us towards development of white-vortex mask described in the following chapter.

7.2 White-vortex phase mask

7.2.1 Concept

The nGRIN VPMs considered in previous chapters only perform well for a certain designed wavelength. That means each VPM is designed with a specific exact thickness for operating at a certain wavelength λ. This monochromatic property can be easily seen from the formula for the total phase shift Eq. (3.3) discussed in Chapter 3:

$$\Delta\varphi_{\text{VPM}} = \frac{2\pi d}{\lambda}\Delta n(\lambda) = 2\pi l,$$

in which, the refractive index difference of the used glass materials $\Delta n(\lambda)$ is almost constant for the considered wavelength range (0.5 µm – 1.5 µm).

In this chapter, a new nanostructured GRIN VPM with the achromatic property will be studied which is white-vortex phase masks (WVPM). In the concept, such an WVPM with a specific thickness allows correcting the chromatic aberration for at least two different wavelengths. According to the above equation, the WVPM with a given thickness to generate OVBs with topological charge l should have the same total phase shift for at least two wavelengths and equal to multiplication of 2π:

$$\Delta\varphi_{\text{WVPM}} = 2\pi l = \frac{2\pi d}{\lambda_1}\Delta n(\lambda_1) = \frac{2\pi d}{\lambda_2}\Delta n(\lambda_2). \tag{7.6}$$

Simplifying this equation with l = 1 (total phase shift is 2π), we have the condition for glass materials making the WVPM for generation of OVBs with fundamental topological charge:

$$\frac{\Delta n(\lambda_1)}{\lambda_1} = \frac{\Delta n(\lambda_2)}{\lambda_2} = \frac{1}{d} = \text{constant} \tag{7.7}$$

Similar to the case of achromatic nGRIN micro-lenses, this condition can be achieved by using an appropriate of the pair of glass materials. Specifically, the ratio between wavelengths λ and the corresponding index differences $\Delta n(\lambda)$ of these glasses for charge l = 1 WVPM must be the same for at least two wavelengths. As a result, the thickness of the mask, as a function of wavelengths for generation of OVBs with topological charge l = 1 should be a polynomial of degree 2 as examples in Fig.7.7.

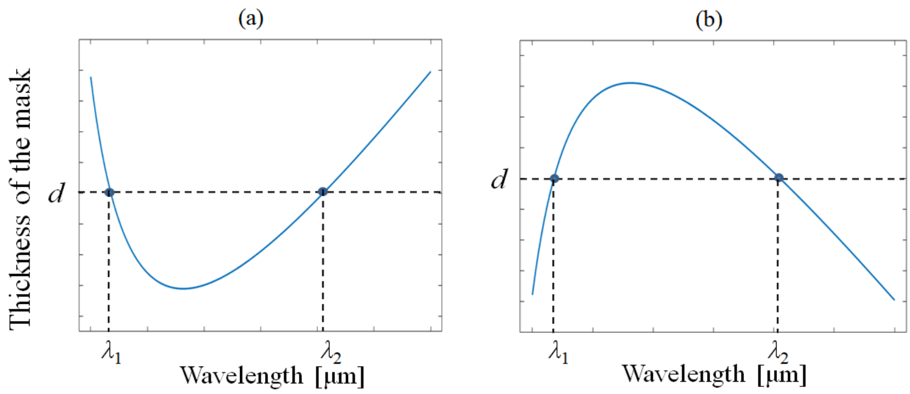

Figure 7.7 Examples of the thickness as a function of wavelengths for the WVPM for generation of OVBs with topological charge l = 1.

It should also notice that the refractive index difference of the selected glasses must ensure the feasibility of fabrication of the WVPM (its thickness should be possible to fabrication implementation). Therefore, it is important to properly select a glass pair having matched dispersion properties as well as the binary nano-rods structure has to be appropriately designed.

7.2.2 Materials

As discussed in chapter 3, the nVPM development using stack and draw technique requires the pair of glass materials having good rheological properties and relevant expansion coefficients as well as thermal matched coefficients. This is also applied on developing a nanostrucutred GRIN WVPM (nWVPM). From conditions presented in Section 7.2.1, we see that it is impossible to find the suitable glass pair from the available glass materials. However, it can be designed and synthesized in-house at *Łukasiewicz Research Network - Institute of Microelectronics & Photonics* (IMiF). First, as a low refractive index glass we proposed to use an already-fabricated soft glass. It is Lead-Bismuth-Gallium Silicate Glasses, labeled CS735 [178]. Its chemical compositions and thermal-physical characteristics are presented in detail in Table 7.1 and 7.2, respectively. Moreover, CS375 glass has high transmission in very wide range of wavelength from visible up to mid-infrared (500 nm and 2800 nm).

Glass label	SiO_2	B_2O_3	Ga_2O_3	PbO	CdO
CS735	35	14	14	30	7

Table 7.1 Chemical compositions of CS735 glass used as low refractive index material for nVPM realization (mol%) [178,180].

Paramaters	**CS735**
Refractive index n at wavelength of 633 nm	2.0139
Thermal expansion coefficient α for 20÷300° C [10^{-7} K^{-1}]	83.5
Transition temperature $\mathbf{T_g}$ [°C] logη = 13.4	467
Dilatometric softening point **SP** [°C] logη = 11.0	491
Characteristic temperatures in Leitz heating microscope **T** [°C]:	
curvature $\mathbf{T_c}$ logη = 9.0	520
sphere $\mathbf{T_{kph}}$ logη = 6.0	560
hemisphere $\mathbf{T_{hs}}$ logη = 4.0	630
spreading $\mathbf{T_{spr}}$ logη = 2.0	780

Table 7.2 Physical and thermal parameters of CS735 glasses

Another hypothetical soft glass was used for high index glass (named glass A). Its dispersion property is determined numerically such that the conditions on refractive indices mentioned in Section 7.2.1 are satisfied. Moreover, for fabrication, this pair of glasses needs to have the same viscosity at the similar temperatures for maintaining the stability of the drawing processes. The acceptable difference of the temperatures is not larger than 50°C. The thermal expansion difference Δα of those glasses should also not exceed the value of $8*10^{-7}$ K^{-1} [178,180] to ensure the structure is not warped.

As a result, the refractive index profiles of a selected artificial glass A and CS735 for the range from 0.5 to 2.5 μm are represented in Fig. 7.8(a). Their refractive index difference as a function of wavelengths in the considered range is depicted in Fig 7.8(b). It can be seen that the difference decreases rapidly going towards shorter wavelengths. In near IR the refractive index difference is small and in mid-IR region is almost constant. Consequently, the nWVPM made of those glasses should theoretically perform achromatically. In particular, Fig.7.8(c) shows the theoretically calculated graph for the mask thickness as a function of wavelengths in the range from 0.5 to 2.5 μm. It predicts that, the white-VPMs with thickness being greater than 55 μm would be able to produce OVBs with topological charge equal exactly 1 at two wavelengths. For instance, white-vortex masks with a thickness of 57 μm can theoretically convert Gaussian beams at wavelengths of 675 nm and 890 nm into two OVBs with charge l =1.

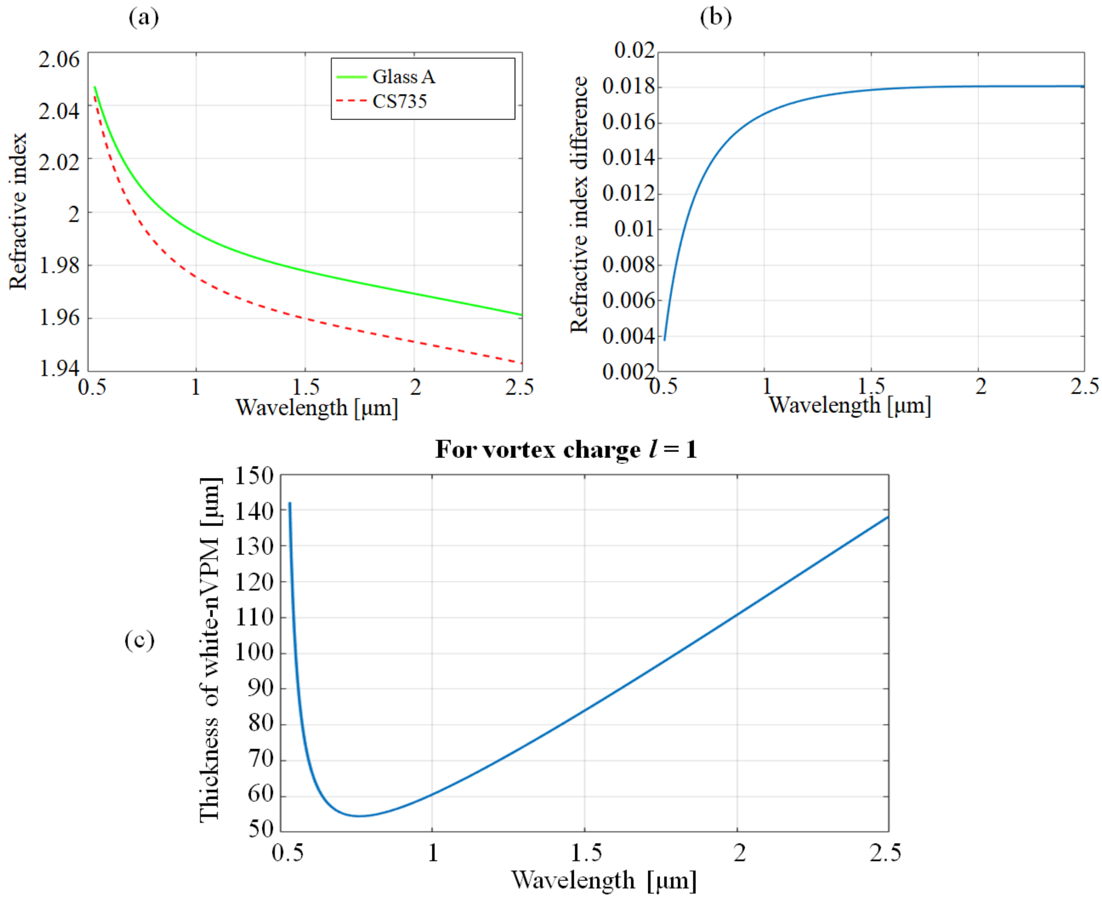

Figure 7.8 Refractive indices of CS735 glass and proposed glass A (a) and their index contrast (b) in the range wavelength from 0.5 to 1.6 μm. (c) thickness of the nGRIN VPMs made of these glasses as a function of wavelengths.

7.2.3 Structure design of white-vortex phase mask and numerical study on its optical performance

The design of a binary-internal structure for such a white-nVPM has been carried out with the whole procedures similar to previously described for nVPMs in Chapter 3. Here the design uses refractive index profiles of the selected glasses describe in Section 7.2.2. As a result, the optimized white-nVPM structure (Fig. 7.11(a)) has the effective refractive index profile is very similar to the ideal continuous index profile as shown in Fig. 7.11(b,c).

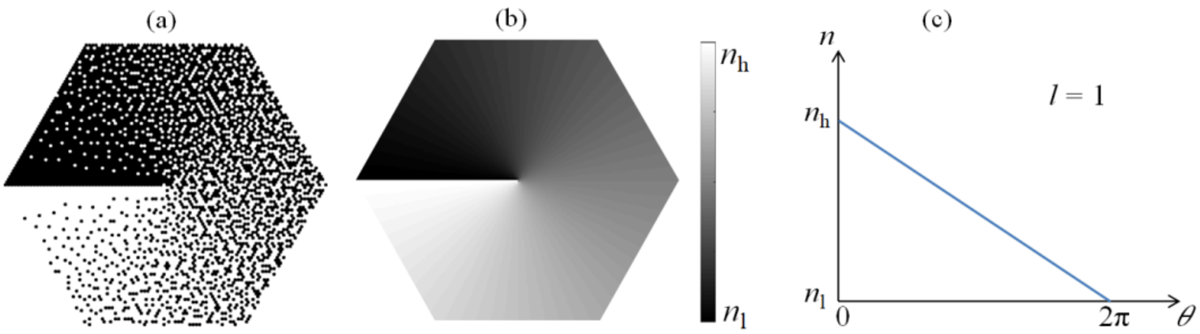

Figure 7.9 Binary nanostructured (a) and the ideal continuous index distribution (b) of white-vortex phase masks and its corresponding index change following the azimuthal angles (c).

The designed binary structure of the nWVPM totally composed of 17557 nanorods arranged in a hexagonal lattice. Its longer diagonal is of ~ of 20 μm with 151 rods along. Individual rods have a diameter of ~130 nm which is much smaller than the rod diameter in our previous nVPMs. As a result, the EMT can be applied more effectively on this nWVPM structure as explained in Chapter 3. As discussed before, the theoretical calculations predict the thickness values of nWVPM with charge l = 1for specific wavelengths as can be seen in listed in Table 7.3. These are based on the available laser sources (633, 890, 0.980, 1064, 1310, and 1550 nm) in our facility which we could use for testing the nGRIN white-VPMs after fabrications.

Thickness of white-VPMs [μm]	55	57	59	61	63	74	86
λ_1 [μm]	0.75	0.675	0.64	0.633	0.62	0.58	0.565
λ_2 [μm]	-	0.89	0.98	1.01	1.064	1.31	1.55

Table 7.3 Theoretically calculated thickness of nWVPM for generation of OVBs with topological charge l = 1 at two wavelength λ_1 and λ_2 .

It should be noticed that when the thickness of the nWVPM is greater, the OVB generation is more strongly influenced by the wave-guide effect as discussed in Chapter 4. At the same time, the wavelength 633 nm is very convenient because it is the He-Ne laser emitting laser line. Such a lasers source has long coherent length easing all interference vortex beam measurements used in previous parts in this dissertation. For this reason, the designed nWVPM with a 61 μm thickness and diameter of 20 μm is selected for the initial study on nWVPM. This mask allows generating OVBs with fundamental topological charge (l=1) at two wavelength λ_1 = 633 nm and λ_2 = 1010 nm has been selected for the initial study. The refractive indices of these selected glasses at 633 nm wavelength are n_{CS735} = 2.0139 and n_A = 2.0243. And those parameters at 1010 nm wavelength are n_{CS735} = 1.9750 and n_A = 1.9916.

The numerical verifications of such theoretical predictions have been carried out for both ideal and nanostructured WVPMs designs for comparisons. The conducted simulations were based on the Fast Fourier transform Beam propagation method described in detail in Chapter 4. The light beam propagation through the WVPM structure and then a 500 μm distance in air has been simulated. The simulations field has an x-y-z dimension of 600x600x561 μm. To make sure the algorithms of the BPM working effectively, the same small calculation steps of 0.1 μm on x axis as well as y axis have been applied in the whole simulated field. However, the steps along the optical axis (z-axis) are different for the structure and air, which are 0.1 μm inside the white-vortex component and 0.5 μm in air. All simulation results have been visualized at the distance of 500 μm from the output end of the components. The incident beams have a size (1/e^2 diameter) of 18 μm for a 20 um aperture of the WVPM which is selected due to similar reasons as discussed in Chapter 5. The numerical simulated field intensity and phase structure of the beam transmitted through the designed WVPMs are represented in Fig. 7.10. In all of cases, the intensity distributions have doughnut shape with a clear on-axis null point, with the spiral phase structure indicating the phase singularity. The beam topological charge l=1 can be determined from presence of single arm in the phase spiral. Therefore, we can confirm the formation of OVBs charge l=1 at both wavelengths of 633 nm and 1010 nm, for both ideal and nanostructured WVPM designs.

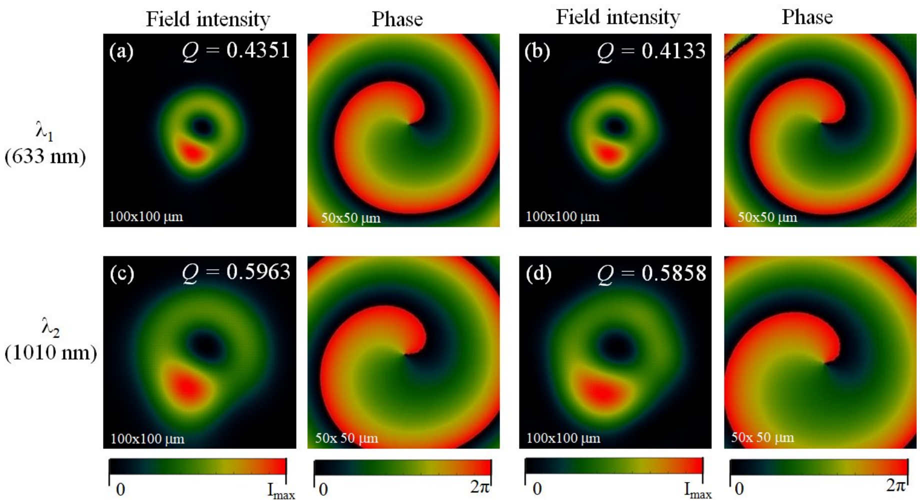

Figure 7.10 Numerically simulated field intensity and phase structure of the beam formed by designed white-VPMs with an ideal continuous index profile (a,c) and binary structure (b,d) at two wavelengths 633 nm (a,b) and 1010 nm (c,d). All results are visualized at the distance of 500 µm from the output surface of the components.

In addition, it is seen that the numerical results for ideal continuous GRIN WVPMs and its corresponding binary nano-structure are very similar. This confirms that there are no degradations of the optical performance when using the designed nanostructure components. It means we obtained an optimum designed structure for the nWVPM which can be used for fabrication in the near future. However, it is not possible to avoid the non-uniformity of intensity patterns of the generated OVBs due to the wave-guide effect as discussed in Chapter 4. The components designed here are quite thick (61 µm) leading the light to localize as a visible bright spot in all studied GRIN WVPMs.

Another interesting fact is that we can obtain OVBs of the same quality having the topological charge l = 1 for wavelength offsets resulting Δl in range of +/- 0.1. This is concluded from a careful theoretical analysis and experimental verification done in scope of chromatic nGRIN VPMs described in Chapter 5 and 6. As an illustration, we consider this properties for the nVPM with thickness of 25 µm (Chapter 5) and the nVPM with thickness of 28 µm used in the all-fiber vortex microprobe (Chapter 6). According with Eq. 3.3 in Chapter 3, we calculated the wavelength range in which an NC-glasses VPM with a certain thickness generate OVBs with topological charge l = 1± 0.1. Figure 7.11 shows the theoretical calculated results for NC-glasses VPMs with thicknesses of 25 µm and 28 µm and.

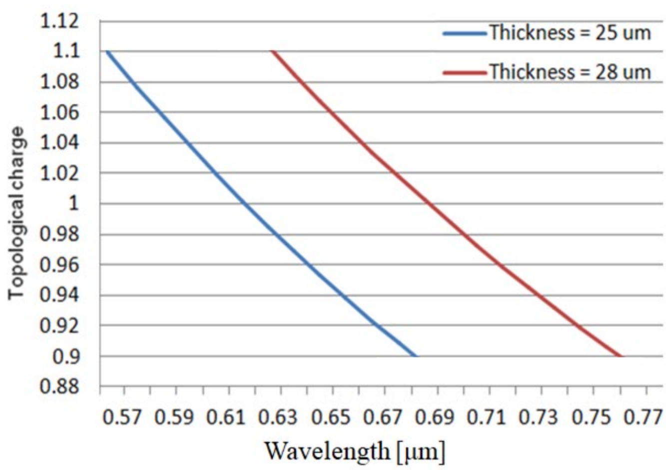

Figure 7.11 Calculated wavelength ranges in which the NC-glass VPMs with thicknesses of 25 and 28 µm can work properly to generate OVBs with fundamental charge.

The proper operation is predicted for a wavelength range of 565÷680 nm and 630÷760, respectively. It can be seen that both nVPMs can well work at the wavelength 633 nm. They numerically and experimentally generated charge 1 OVBs with similar quality as shown in Chapter 5 and Chapter 6. Therefore, we subsequently carried out the theoretical analysis and numerical simulations of such properties of the designed WVPM with thickness of 61 μm. As mentioned previously, there are no degradations of the performance of the binary nanostructure in comparison to the mask with ideal continuous index profile. Thus, it is enough to conduct the numerical simulations for only the binary nanostructured WVPMs. The study predicts that the 61-μm thick white-nVPM can effectively work for wavelength range from 600nm to 1165 nm which results with wavelength bandwidth of 565 nm (Fig. 7.12). Consequently, we achieve OVBs with charge $l \cong 1$ with an error Δl = [-0.1; +0.1] in that wavelength range.

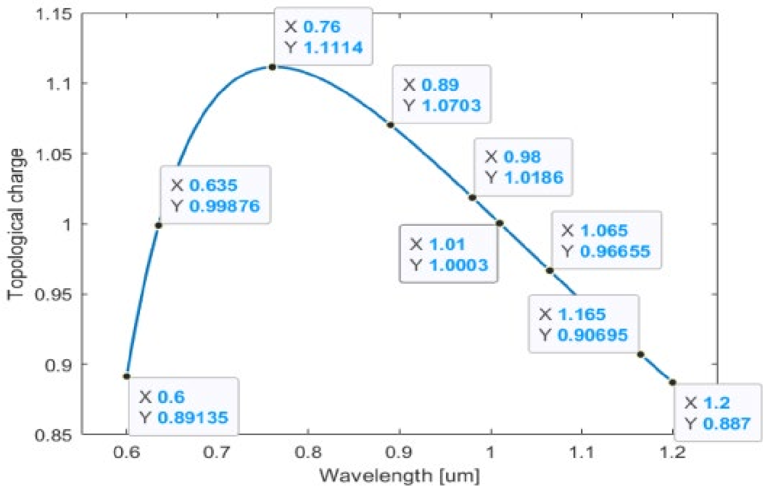

Figure 7.12 Calculated values of topological charge of OVBs using the 62-μm-thick white-nVPM as a function of wavelengths.

The numerical simulations have been performed for several selected wavelengths including 760, 600, 1165 nm at which OVBs are at the boundary of the topological charge (l = ~1.1 and 0.9) as depicted in Fig. 7.14. Other wavelengths have been chosen involving the available laser sources we have in our facility (890, 980, 1064 nm). Input geometrical parameters for the white-VPM and simulated parameter for modeling are kept the same as previously presented numerical calculation set. The obtained results are presented in Fig 7.13.

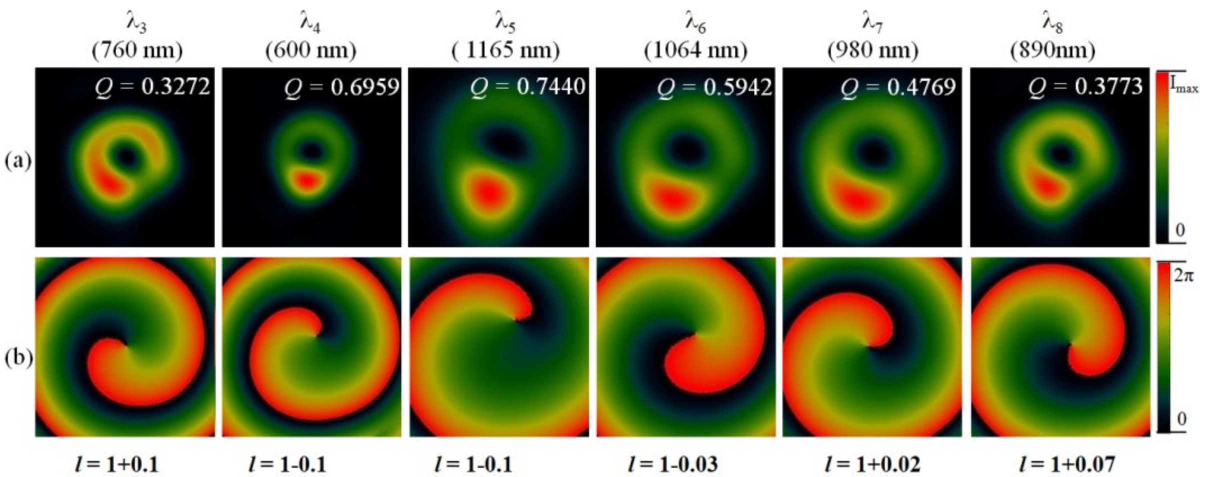

Figure 7.13 Numerically simulated intensity (a) and phase structure (b) of the beam formed by 61-μm-thick nWVPM at several selected wavelengths (760, 600, 1165, 1064, 980, 890 nm). All results are visualized at the distance of 500 μm from the output surface of the mask.

The modeling results are presented in Fig. 7.13. The output beams in all cases exhibit doughnut-like intensity patterns and single phase spirals. These results confirm the generation of OVBs with topological charge l = 1 in all considered cases. However, it is visible that the uniformity of those intensity patterns differs for different wavelengths, which is agreed by quality parameter Q. In particular, the light localizations on intensity profiles of created OVBs are the strongest for the extreme value of Δl = - 0.1. Their uniformity degree is the lowest with Q > 0.69. Moreover, at 1165 nm wavelength, the bright ring pattern starts to break. This is in agreement with its phase structure with the out-of-axis location of the phase singularity. Opposite situation resulted for the boundary Δl = + 0.1 (760 nm wavelength), the OVB presents correct phase distribution and much improvement of intensity uniformity with the lowest quality parameter Q of 0.3272. The uniformity degree reduces gradually for OVBs at shorter and longer wavelengths (the quality parameters for those cases are higher). The simulations as so far showed to be reliable which were proved by the performed experiment here. It is most likely also in this case. However, due to time constrains of the realization of the thesis, I was not able to fabricate the structure, and thereby measurements were not possible now.

7.3 Summary

In this chapter, the concept of the nWVPMs with achromatic property has been proposed and its ability to generate broadband beam white-vortex have been demonstrated numerically. So far the number of white vortex beam generation methods is very limited. Moreover there is high demand for such a beam; thereby it is vibrant subject of singular optics.

At first, we presented the successful development of achromatic nGRIN microlens for the near-infrared spectral range. The concept of nGRIN microlens with an achromatic property has been proposed and demonstrated. The design of this kind of microlens is based on the EMT and nanostructurization technique which is realized by a modified stack and draw method. The achromatic microlens with flat-parallel surfaces has been designed and fabricated using two types of in-house made boro-silicate glasses (NC21A and NC34). The fabricated nanostructured lens with a thickness of 36 μm (0.12 pitch) and a diameter of ~20 μm was investigated experimentally by the use of several laser sources at different wavelengths of 532, 658, 850, 980, 1310 and 1550 nm. Measurements revealed that working distances of the test lens are in range of 34.1 to 35.6 μm for the considered wavelength range. In particular, the lens shows the longest working distance of 35.6 μm at 980 nm wavelengths and for the extreme values of the considered wavelengths the working distance was the shortest. This proved that our nGRIN microlens have similar performance to standard aspheric doublets, but utilize a simpler, singlet element geometry with flat surfaces and have a microscopic size.

The promising results for microlens gave an idea to design white vortex phase mask, and its concept was proposed. The optical performance of WVPMs has been verified analytically and by numerical simulations. We used an in-house-made soft glass (CS375) and another hypothetical glass for the nWVPM. This appropriate glass pair produces the required index profile for the achromatic properties as well as technically achievable thickness of the component. Then, its nano-structure with an azimuthal gradient index profile is designed using a combination of the simulated annealing method and the effective medium theory. The numerical verifications of white-vortex generations of the 61-μm-thick VPM have been implemented by the usage of the aforementioned BPM method. In addition, we also have numerically proved that this WVPM is able to well convert Gaussian beam into OVBs with topological charge l≅1 for a wide wavelength range from 600nm to 1165 nm with a 565 nm bandwidth.

Chapter 8. Conclusion and future work

In this dissertation, I have theoretically and experimentally studied the optical performance of the fabricated nGRIN VPMs for a deeper understanding of their properties. I have developed new fiber-based vortex converter microprobes exploiting such nVPMs. I designed an achromatic vortex mask for white vortex generation. The accomplished objectives mentioned at the beginning of the dissertation are summarized with future potentials as per below.

The first thesis *"The microscopic optical vortex beams with various topological charge values can be generated in air and liquid media by using the same nano-srtuctured GRIN VPMs. The problem of the light waveguide effect inside the gradient phase components, which accounts to the non-uniformity of the beam intensity profile, can be mitigated"* **has been verified in Chapter 4 and Chapter 5.**

To verify the possibilities to mitigate the effect of the light waveguide on generated micro-optical vortices using the nanostructured GRIN VPM, I carried out numerical studies on several factors in terms of its refractive index contrast and index profiles of glass materials in Chapter 4. Obtained results demonstrated that, the light-localization on the doughnut-like intensity pattern of the OVBs could be significantly minimized by employing ***glass pairs which provide high index contrasts for nVPM fabrication***. In such a case, the mask thickness would be very small, and the wave-guide effect can be neglected. Almost perfect OVBs with topological charge l = 1 can be created by utilizing practically in-house synthesized glasses: a lead-bismuth-gallate glass PBG81 and silicate glass UV710 ($\Delta n_{UP} \approx 0.376$, the component thickness d_{UP} = 4 µm at λ = 1.55 µm). However, the fabrication of such a thin component is technologically challenging due to requirements on thickness accuracy. Another proposed approach in this work is developing technically-achievable-thickness nVPMs (60 µm) by ***investigating non-linear (described by power function) azimuthal gradient index profiles with various values of the shape power index*** g. We found a significant improvement in the uniformity of OVBs' cross-sectional intensity pattern for g = 1/4. Here the refractive index increases with an azimuthal angle slowly at the beginning and much faster towards the end of the profile. In this case, we used in-house-made borosilicate glasses NC21 and NC32 ($\Delta n_{NC} \approx 0.025$), whose mechanical and thermal properties are matched for joining in the drawing process. Performed numerical calculations showed that although the light localization was still present, the wave-guide effect was much minimized, producing a reasonable uniform pattern of generated OVBs.

In addition, ***possibilities of high topological charge OVB generation exploiting the same fabricated nanostructured vortex phase masks having different thicknesses*** have been numerically and experimentally verified in chapter 5. The same fabricated nanostructured nVPMs with thickness of 25 µm and 50 µm were used to generate OVBs with topological charges of l = 1 and l = 2 at the wavelength of 633 nm, respectively. That means the same fabricated vortex structured fiber can be cut into thicker slices of suitable thickness for higher topological charge masks. The properties of generated OVBs such as intensity and phase profiles indicating singularity and topological charge were determined with the use of two experimental techniques, astigmatic transformation, and Mach-Zehnder interferometry. Obtained simulation results showed that the optical performance of ideal continuous VPMs and nanostructured phase masks, fabricated by the modified stack-and-draw method, is the same. It proved the binary nanostructurization technique is the simplest implementation allowing the continuous azimuthal phase variation.

More importantly, I verified in Chapter 5 that ***optical performance of the nVPMs is not affected by surrounding transparent media***. I conducted the generations of optical vortex beams with topological charge l = 1 at the wavelength of 633 nm by using one nVPM with thickness of 25 µm demonstrated immersed in water, ethanol and in air. The results shown theoretically as well as experimentally that the component works the same in all these media, even, the intensity distribution of OVBs was better in liquid media.

Those above results bring a conclusion that the first thesis of this dissertation is verified positively.

The second thesis: "*Fiber-based micro-optical converter with the integrated gradient index vortex mask allows the efficient conversion of the Gaussian beam into the vortex beam*" **has been analyzed in Chapter 6.** Here, a novel fiber-based vortex converter microprobe has been fabricated and optically characterized in air and water. The integrated converter system includes a single-mode fiber operating at the 633 nm wavelength, 84-μm NC21-glass spacer, and 28-μm-thick nVPM at the fiber end. Both experimental and theoretical studies were demonstrated that the fabricated fiber-based vortex converter efficiently converts fiber-guided fundamental mode into OVBs with a single topological charge $l = 1$. Moreover, the optical performance is preserved in transparent external media. This was proved experimentally by measurements of the optical performance of fiber-based vortex converter microprobe immersed in water and air. All the reported fiber-based systems so far used conventional SPPs, and their optical performance was affected by the change of the external medium. The presented research results proved the compatibility of nVPM in fiber optics. These results bring a conclusion that the second Thesis of this dissertation is verified positively.

The third thesis "*Achromatic vortex beams can be obtained by using nGRIN vortex mask made of glasses with matched material dispersive properties*" **has been analyzed in Chapter 7**. Generation of white-vortex beam is an interesting subject in singular optics and there are only a few existing methods for the realization. In this work, the concept of the white-nVPMs (nWVPMs) with achromatic property has been proposed. Its ability to generate white-vortex beams has been demonstrated numerically. At first, the development of microlenses achromatically corrected in near-infrared spectral windows was demonstrated. This showed the possibility of applying the internal nanostructurization technique to the design of an nWVPM. I used an in-house-made soft glass (CS375) and another hypothetical glass (glass A) for the nWVPM. The glass pair made of the aforementioned glasses ensures the required refractive index profile for the achromatic properties as well as the thickness of the component is technically achievable. Its nano-structure with an azimuthal gradient index profile was designed using a combination of the simulated annealing method and the effective medium approximation theory. The numerical verifications of white-vortex generations using the 61-μm-thick VPM was performed using BPM method. In addition, I have also numerically proved that this white-nVPM can convert Gaussian beam into OVBs with topological charge $l \cong 1$ in the broad wavelength range with a 565 nm bandwidth (in the wavelength range 600 nm to 1165 nm). These results bring a conclusion that the second Thesis of this dissertation is verified positively.

Future perspective for nGRIN vortex phase masks

My achievement of this work is important because presented micro-optical VPMs have remarkable unique properties in comparison with vortex generators realized by other techniques. The unique properties make the nVPM good candidates for various promising applications and research fields.

The nVPMs, with flat-parallel surfaces, can be easily and efficiently integrated with other micro-components and optical fibers into compact optical systems. In particular, it allows making fiber-based vortex converter micro-probes which allow effective generation and flexible control of optical vortex beam in a dramatically simplified system instead of complex bulky free-space setup. Moreover, the fiber-based vortex converter probe can maintain its optical performance in any transparent media including gas and liquids. Such a property is unique and for the first time reported for fiber-based systems providing opportunity to use the same component in different external environments and promising for micro-optofluidic applications, especially where there is a need to study the microfluidic channel via the fiber port. For instance, the fiber-based vortex converter microprobe can be used in optical trapping and particle manipulation experiments in liquids.

The fabricated micro-vortex converter is made all of glass, and thereby it has the high laser damage threshold. That makes the device well suited to generate high power vortex. These properties open up perspectives for use this system for laser processing and ablation with structured beams including e.g. micro-drilling and surface structuring with twisted holes and pillars, respectively, as well as excitation of modes with orbital angular momentum in optical fibers.

In addition, our work confirms the feasibility of using a sequential combination of nanostructured gradient index micro-optical components having different functionalities in one optical system and still maintaining the compatibility with the optical fiber technique. The nVPM can be considered for development of all-fiber laser vortex beam source, as it can be easily integrated with fiber laser resonator thanks to flat surfaces, rigid construction and overall compatibility with the fiber technology.

There are still a lot of works left related to further fundamental research and development of different new techniques on next nVPM-based optical devices, for example, devices for generation of optical vortex beam in mid-IR regime.

References

1. M. Brambilla, F. Battipede, L. A. Lugiato, V. Penna, F. Prati, C. Tamm, and C. O. Weiss, "Transverse laser patterns. I. Phase singularity crystals," Phys. Rev. A **43**, 5090-5113 (1991).
2. I. Freund and N. Shvartsman, "Wave-field phase singularities: The sign principle," Phys. Rev. A, **50**, 5164-5172 (1994).
3. N. Shvartsman and I. Freund, "Vortices in random wave fields: Nearest neighbor anticorrelations," Phys. Rev. Lett. **72**, 4156 (1994).
4. L. D. P. Thborique and P. Valrose, "Optical Vortices," Opt. Commu. **73**, 403–408 (1989).
5. J. F. Nye, M. V Berry, and P. R. S. L. A, "Dislocations in wave trains," Proc. R. Soc. London. A. Math. Phys. Sci. **336**, 165–190 (1974).
6. Y. Shen, X. Wang, Z. Xie, C. Min, X. Fu, Q. Liu, M. Gong, and X. Yuan, "Optical vortices 30 years on: OAM manipulation from topological charge to multiple singularities," Light Sci. Appl. **8**, 1–29 (2019).
7. L. Zhu and J. Wang, "A review of multiple optical vortices generation: methods and applications," Front. Optoelectron. **12**, 52–68 (2019).
8. S. Fürhapter, A. Jesacher, S. Bernet, and M. Ritsch-Marte, "Spiral phase contrast imaging in microscopy," Opt. Express **13**, 689 (2005).
9. K. I. Willig, S. O. Rizzoli, V. Westphal, R. Jahn, and S. W. Hell, "STED microscopy reveals that synaptotagmin remains clustered after synaptic vesicle exocytosis," Nature **440**, 935–939 (2006).
10. H. He, M. E. J. Friese, N. R. Heckenberg, and H. Rubinsztein-Dunlop, "Direct Observation of Transfer of Angular Momentum to Absorptive Particles from a Laser Beam with a Phase Singularity," Phys. Rev. Lett. **75**, 826-829 (1995).
11. M. Padgett and R. Bowman, "Tweezers with a twist," Nat. Photonics **5**, 343–348 (2011).
12. V. G. Shvedov, A. V Rode, Y. V Izdebskaya, A. S. Desyatnikov, W. Krolikowski, and Y. S. Kivshar, "Giant optical manipulation," Phys. Rev. Lett. **105**, 1–4 (2010).
13. J. E. Curtis, B. A. Koss, and D. G. Grier, "Dynamic holographic optical tweezers," Opt. Commun. **207**, 169-175 (2002).
14. X. Zhuang, "Unraveling DNA condensation with optical tweezers," Science **305**, 188-190 2004).
15. D. G. Grier, "A revolution in optical manipulation," Nature **424**, 810–816 (2003).
16. J. Wang, "Advances in communications using optical vortices," Photonics Res. **4**, B14-B28 (2016).
17. A. E. Willner, H. Huang, Y. Yan, Y. Ren, N. Ahmed, G. Xie, C. Bao, L. Li, Y. Cao, Z. Zhao, J. Wang, M. P. J. Lavery, M. Tur, S. Ramachandran, A. F. Molisch, N. Ashrafi, and S. Ashrafi, "Optical communications using orbital angular momentum beams," Adv. Opt. Photonics **7**, 66-106 (2015).
18. G. Molina-Terriza, J. P. Torres, and L. Torner, "Twisted photons," Nat. Phys. **3**, 305 (2007).
19. M. Krenn, M. Malik, M. Erhard, and A. Zeilinger, "Orbital angular momentum of photons and the entanglement of LaguerreGaussian modes," Philos. Trans. R. Soc. A Math. Phys. Eng. Sci. **375**, (2017).
20. M. Erhard, R. Fickler, M. Krenn, and A. Zeilinger, "Twisted photons: new quantum perspectives in high dimensions," Light Sci. Appl. **7**, 17146–17146 (2017).
21. T. Omatsu, K. Miyamoto, K. Toyoda, R. Morita, Y. Arita, and K. Dholakia, "A New Twist for Materials Science: The Formation of Chiral Structures Using the Angular Momentum of Light," Adv. Opt. Mater. **1801672**, 1–18 (2019).
22. D. M. Palacios, G. Foo, and G. A. Swartzlander, "Optical vortex coronagraph," Opt. Lett. **30**, 3308–3310 (2005).
23. J. H. Lee, G. Foo, E. G. Johnson, and J. Grover A. Swartzlander, "Experimental Verification of an Optical Vortex Coronagraph," Phys. Rev. Lett. **97**, 053901 (2006).
24. T. Omatsu, K. Miyamoto, and A. J. Lee, "Wavelength-versatile optical vortex lasers," J. Opt. (United Kingdom) **19**, (2017).
25. X. Wang, Z. Nie, Y. Liang, J. Wang, T. Li, and B. Jia, "Recent advances on optical vortex

generation," Nanophotonics **7**, 1533–1556 (2018).
26. G. J. Gbur, *Singular Optics,* 1st Edition (2016).
27. M. W. Beijersbergen, R. P. C. Coerwinkel, M. Kristensen, and J. P. Woerdman, "Helical-wavefront laser beams produced with a spiral phaseplate," Opt. Commun. **112**, 321–327 (1994).
28. G. A. Swartzlander, Jr., "Achromatic optical vortex lens," Opt. Lett. **31**, 2042 (2006).
29. M. Massari, G. Ruffato, M. Gintoli, F. Ricci, and F. Romanato, "Fabrication and characterization of high-quality spiral phase plates for optical applications," Appl. Opt. **54**, 4077 (2015).
30. H.-Y. Tsai, H. I. Smith, and R. Menon, "Fabrication of spiral-phase diffractive elements using scanning-electron-beam lithography," J. Vac. Sci. Technol. B Microelectron. Nanom. Struct. **25**, 2068 (2007).
31. T. Watanabe, M. Fujii, Y. Watanabe, N. Toyama, and Y. Iketaki, "Generation of a doughnut-shaped beam using a spiral phase plate," Rev. Sci. Instrum. **75**, 5131 (2004).
32. A. Žukauskas, M. Malinauskas, and E. Brasselet, "Monolithic generators of pseudo-nondiffracting optical vortex beams at the microscale," Appl. Phys. Lett. **103**, (2013).
33. K. Qu, Q. Jia, and N. J. Fisch, "Plasma q -plate for generation and manipulation of intense optical vortices," Phys. Rev. E **96**, 053207 (2017).
34. N. R. Heckenberg, R. McDuff, C. P. Smith, and A. G. White, "Generation of optical phase singularities by computer-generated holograms," Opt. Lett. **17**, 221 (1992).
35. A. Forbes, A. Dudley, and M. McLaren, "Creation and detection of optical modes with spatial light modulators," Adv. Opt. Photonics **8**, 200 (2016).
36. N. Matsumoto, T. Ando, T. Inoue, Y. Ohtake, N. Fukuchi, and T. Hara, "Generation of high-quality higher-order Laguerre-Gaussian beams using liquid-crystal-on-silicon spatial light modulators," J. Opt. Soc. Am. A **25**, 1642-1651 (2008).
37. A. Jesacher, C. Maurer, A. Schwaighofer, S. Bernet, and M. Ritsch-Marte, "Full phase and amplitude control of holographic optical tweezers with high efficiency," Opt. Express **16**, 4479 (2008).
38. L. Zhu and J. Wang, "Arbitrary manipulation of spatial amplitude and phase using phase-only spatial light modulators," Sci. Reports **4**, 1–7 (2014).
39. S. Ramachandran and P. Kristensen, "Optical vortices in fiber," Nanophotonics **2**, 455–474 (2013).
40. X. Heng, J. Gan, Z. Zhang, J. Li, M. Li, H. Zhao, Q. Qian, S. Xu, and Z. Yang, "All-fiber stable orbital angular momentum beam generation and propagation," Opt. Express **26**, 17429 (2018).
41. Z. Lin, A. Wang, L. Xu, X. Zhang, B. Sun, C. Gu, and H. Ming, "Generation of optical vortices using a helical fiber bragg grating," J. Light. Technol. **32**, 2152–2156 (2014).
42. C. Jocher, C. Jauregui, C. Voigtländer, F. Stutzki, S. Nolte, J. Limpert, and A. Tünnermann, "Fiber based polarization filter for radially and azimuthally polarized light," Opt. Express **19**, 19582-19590 (2011).
43. P. Z. Dashti, F. Alhassen, and H. P. Lee, "Observation of orbital angular momentum transfer between acoustic and optical vortices in optical fiber," Phys. Rev. Lett. **96**, 043604 (2006).
44. T. Wang, F. Wang, F. Shi, F. Pang, S. Huang, T. Wang, and X. Zeng, "Generation of Femtosecond Optical Vortex Beams in All-Fiber Mode-Locked Fiber Laser Using Mode Selective Coupler," J. Light. Technol. **35**, 2161–2166 (2017).
45. Y. Zhao, T. Wang, C. Mou, Z. Yan, Y. Liu, and T. Wang, "All-Fiber Vortex Laser Generated with Few-Mode Long-Period Gratings," IEEE Photonics Technol. Lett. **30**, 752–755 (2018).
46. Y. Yan, L. Zhang, J. Wang, J.-Y. Yang, I. M. Fazal, N. Ahmed, A. E. Willner, and S. J. Dolinar, "Fiber structure to convert a Gaussian beam to higher-order optical orbital angular momentum modes," Opt. Lett. **37**, 3294 (2012).
47. Z. Yimin, R. Tao, H. Li, W. Fang, Z. Dong, C. Dai, L. Xu, C. Gu, W. Chen, Y. Zhu, Q. Zhan, and P. Yao, "Stable generation of cylindrical vector beams with an all-fiber laser using polarization-maintaining and ring-core fibers," Opt. Express **28**, 18351 (2020).
48. A. Gizatulin, I. Meshkov, I. Vinogradova, V. Bagmanov, E. Grakhova, and A. Sultanov, "Generation of Vortex Optical Beams Based on Chiral Fiber-Optic Periodic Structures,"

Sensors **20**, 5345 (2020).
49. R. S. Rodrigues Ribeiro, P. Dahal, A. Guerreiro, P. Jorge, and J. Viegas, "Optical fibers as beam shapers: from Gaussian beams to optical vortices," Opt. Lett. **41**, 2137 (2016).
50. K. Weber, F. Hütt, S. Thiele, T. Gissibl, A. Herkommer, and H. Giessen, "Single mode fiber based delivery of OAM light by 3D direct laser writing," Opt. Express **25**, 19672 (2017).
51. J. Yu, Y. P. Wang, W. Yang, Z. Y. Bai, Z. Xie, Z. Liu, and C. R. Liao, "All-fiber focused beam generator integrated on an optical fiber tip," Appl. Phys. Lett. **116**, 241102 (2020).
52. F. Hudelist, R. Buczynski, A. J. Waddie, and M. R. Taghizadeh, "Design and fabrication of nano-structured gradient index microlenses," Opt. Express **17**, 3255 (2009).
53. J. Nowosielski, R. Buczynski, A. J. Waddie, A. Filipkowski, D. Pysz, A. McCarthy, R. Stepien, and M. R. Taghizadeh, "Large diameter nanostructured gradient index lens," Opt. Express **20**, 11767 (2012).
54. F. Hudelist, J. M. Nowosielski, R. Buczynski, A. J. Waddie, and M. R. Taghizadeh, "Nanostructured elliptical gradient-index microlenses," Opt. Lett. **35**, 130 (2010).
55. R. Buczynski, A. Filipkowski, A. J. Waddie, B. Piechal, J. Nowosielski, D. Pysz, R. Stepien, and M. R. Taghizadeh, "Large elliptical nanostructured gradient-index microlens," Appl. Opt. **55**, 89 (2016).
56. A. Filipkowski, B. Piechal, D. Pysz, R. Stepien, A. Waddie, M. R. Taghizadeh, and R. Buczynski, "Nanostructured gradient index microaxicons made by a modified stack and draw method," Opt. Lett. **40**, 5200 (2015).
57. K. Switkowski, A. Anuszkiewicz, A. Filipkowski, D. Pysz, R. Stepien, W. Krolikowski, and R. Buczynski, "Formation of optical vortices with all-glass nanostructured gradient index masks," Opt. Express **25**, 31443 (2017).
58. A. Filipkowski, B. Piechal, D. Pysz, R. Stepien, J. Cimek, A. Waddie, M. Klimczak, P. Stafiej, M. R. Taghizadeh, and R. Buczynski, "World-smallest fiber-GRIN lens system for optofluidic applications," Photonics Lett. Pol. **8**, 36–38 (2016).
59. R. Kasztelanic, A. Filipkowski, A. Anuszkiewicz, P. Stafiej, G. Stepniewski, D. Pysz, K. Krzyzak, R. Stepien, M. Klimczak, and R. Buczynski, "Integrating Free-Form Nanostructured GRIN Microlenses with Single-Mode Fibers for Optofluidic Systems," Sci. Rep. **8**, 1–12 (2018).
60. A. Filipkowski, H. T. Nguyen, R. Kasztelanic, T. Stefaniuk, J. Cimek, D. Pysz, R. Stępień, K. Krzyżak, P. Karioja, and R. Buczynski, "Development of large diameter nanostructured GRIN microlenses enhanced with temperature-controlled diffusion," Opt. Express **27**, 35052 (2019).
61. H. T. Nguyen, A. Anuszkiewicz, J. Lisowska, A. Filipkowski, R. Kasztelanic, R. Buczynski, and W. Krolikowski, "Numerical analysis of optical vortices generation with nanostructured phase masks," Opt. Express **28**, 21143 (2020).
62. H. T. Nguyen, K. Switkowski, R. Kasztelanic, and A. Anuszkiewicz, "Optical characterization of single nanostructured gradient index vortex phase masks fabricated by the modified stack-and-draw technique," Opt. Commun. **463**, 125435 (2020).
63. H. T. Nguyen, K. Switkowski, A. Filipkowski, R. Kasztelanic, D. Pysz, H. Van Le, R. Stepien, W. Krolikowski, and R. Buczynski, "Fiber microprobe with integrated gradient index vortex mask," Opt. Commun. **477**, 126345 (2020).
64. H. T. Nguyen, K. Switkowski, A. Filipkowski, R. Kasztelanic, D. Pysz, H. Van Le, B. Van Chu, R. Stepien, W. Krolikowski, and R. Buczynski, "All-fiber nanostructured gradient optics vortex beam converter," Opt. Lasers Eng. **150**, 106841 (2022).
65. R. Buczynski, A. Filipkowski, B. Piechal, H. T. Nguyen, D. Pysz, R. Stepien, A. Waddie, M. R. Taghizadeh, M. Klimczak, and R. Kasztelanic, "Achromatic nanostructured gradient index microlenses," Opt. Express **27**, 9588 (2019).
66. M. R. Dennis, K. O. Holleran, and M. J. Padgett, *Chapter 5 Singular Optics: Optical Vortices and Polarization Singularities* (Elsevier B.V., 2009), Vol. **53**.
67. M. S. Soskin and M. V. Vasnetsov, "Nonlinear singular optics," Pure Appl. Opt. **7**, 301-311 (1998).
68. M. S. Soskin and M. V. Vasnetsov, "Chapter 4 Singular optics," in *Progress in Optics* (Elsevier, 2001), Vol. **42**, pp. 219–276.
69. Q. Zhan, "Cylindrical vector beams: From mathematical concepts to applications," Opt.

InfoBase Conf. Pap. **1**, 1–57 (2009).
70. M. Padgett, J. Courtial, and L. Allen, "Light's orbital angular momentum," Phys. Today **57**, 35–40 (2004).
71. L. Allen, M. W. Beijersbergen, R. J. C. Spreeuw, and J. P. Woerdman, "Orbital angular momentum of light and the transformation of Laguerre-Gaussian laser modes," Phys. Rev. A **45**, 8185–8189 (1992).
72. L. Allen, M. J. Padgett, and M. Babiker, "IV The Orbital Angular Momentum of Light," Prog. Opt. **39**, 291–372 (1999).
73. A. M. Yao and M. J. Padgett, "Orbital angular momentum: origins, behavior and applications," Adv. Opt. Photonics **3**, 161-204 (2011).
74. Q. Zhan, "Properties of circularly polarized vortex beams," Opt. Lett. **31**, 867 (2006).
75. D. G. Hall, "Vector-beam solutions of Maxwell's wave equation," Opt. Lett. **21**, 9 (1996).
76. B. Ndagano, I. Nape, M. A. Cox, C. Rosales-Guzman, and A. Forbes, "Creation and Detection of Vector Vortex Modes for Classical and Quantum Communication," J. Light. Technol. **36**, 292-301 (2018).
77. J. M. Vaughan and D. V. Willetts, "Interference properties of a light beam having a helical wave surface," Opt. Commun. **30**, 263–267 (1979).
78. M. Padgett, J. Arlt, N. Simpson, and L. Allen, "An experiment to observe the intensity and phase structure of Laguerre-Gaussian laser modes," Cit. Am. J. Phys. **64**, 77 (1996).
79. G. Bogatiryova and M. Soskin, "Detection and metrology of optical vortex helical wave fronts," Semicond. Phys. Quantum Electron. Optoelectron. **6**, 254–258 (2003).
80. C. Du, J. Wang, Q. Mo, S. Li, and X. Hu, "Controllable all-fiber orbital angular momentum mode converter," Opt. Lett. **40**, 4376–4379 (2015).
81. S. Cui, B. Xu, S. Luo, H. Xu, Z. Cai, Z. Luo, J. Pu, and S. Chávez-Cerda, "Determining topological charge based on an improved Fizeau interferometer," Opt. Express **27**, 12774 (2019).
82. B. Khajavi and E. J. Galvez, "Determining topological charge of an optical beam using a wedged optical flat," Opt. Lett. **42**, 1516 (2017).
83. P. Kumar and N. K. Nishchal, "Self-referenced interference of laterally displaced vortex beams for topological charge determination," Opt. Commun. **459**, 125000 (2020).
84. V. G. Shvedov, C. Hnatovsky, W. Krolikowski, and A. V. Rode, "Efficient beam converter for the generation of high-power femtosecond vortices," Opt. Lett. **35**, 2660 (2010).
85. A. P. Porfirev and S. N. Khonina, "Astigmatic transformation of optical vortex beams with high-order cylindrical polarization," J. Opt. Soc. Am. B **36**, 2193 (2019).
86. L. Yongxin, T. Hua, P. Jixiong, and L. Baida, "Detecting the topological charge of vortex beams using an annular triangle aperture," Opt. Laser Technol. **43**, 1233–1236 (2011).
87. C.-S. Guo, L.-L. Lu, and H.-T. Wang, "Characterizing topological charge of optical vortices by using an annular aperture," Opt. Lett. **34**, 3686 (2009).
88. C. S. Guo, S. J. Yue, and G. X. Wei, "Measuring the orbital angular momentum of optical vortices using a multipinhole plate," Appl. Phys. Lett. **94**, 231104 (2009).
89. G. Gibson, J. Courtial, M. J. Padgett, M. Vasnetsov, V. Pas'ko, S. M. Barnett, and S. Franke-Arnold, "Free-space information transfer using light beams carrying orbital angular momentum," Opt. Express **12**, 5448 (2004).
90. M. Chen, F. S. Roux, and J. C. Olivier, "Detection of phase singularities with a Shack-Hartmann wavefront sensor," J. Opt. Soc. Am. A **24**, 1994 (2007).
91. S. Pachava, R. Dharmavarapu, A. Vijayakumar, S. Jayakumar, A. Manthalkar, A. Dixit, N. K. Viswanathan, B. Srinivasan, and S. Bhattacharya, "Generation and decomposition of scalar and vector modes carrying orbital angular momentum: a review," Opt. Eng. **59**, 041205 (2019).
92. J.-F. Bisson, Y. Senatsky, and K.-I. Ueda, "Generation of Laguerre-Gaussian modes in Nd:YAG laser usingdiffractive optical pumping," Laser Phys. Lett. **2**, 327 (2005).
93. D. Lin, J. M. O. Daniel, and W. A. Clarkson, "Controlling the handedness of directly excited Laguerre Gaussian modes in a solid-state laser," Opt. Lett. **39**, 3903–3906 (2014).
94. K. Kano, Y. Kozawa, and S. Sato, "Generation of a purely single transverse mode vortex beam from a He-Ne laser cavity with a spot-defect mirror," Int. J. Opt. **2012**, (2012).
95. M. Okida, Y. Hayashi, T. Omatsu, J. Hamazaki, and R. Morita, "Characterization of 1.06 μm

optical vortex laser based on a side-pumped Nd:GdVO 4 bounce oscillator," Appl. Phys. B **95**, 69–73 (2009).
96. S. Ngcobo, I. Litvin, L. Burger, and A. Forbes, "A digital laser for on-demand laser modes," Nat. Commun. **4**, 1–6 (2013).
97. A. Forbes, "Controlling lights helicity at the source: orbital angular momentum states from lasers," Philos. Trans. R. Soc. A Math. Phys. Eng. Sci. **375**, (2017).
98. M. W. Beijersbergen, L. Allen, H. E. L. O. van der Veen, and J. P. Woerdman, "Astigmatic laser mode converters and transfer of orbital angular momentum," Opt. Commun. **96**, 123–132 (1993).
99. M. Padgett, J. Arit, N. Simpson, and L. Allen, "An experiment to observe the intensity and phase structure of laguerre-gaussian laser modes," Am. Assoc. Phys. Teach. **77**, 114–119 (1996).
100. M. J. Padgett and J. Courtial, "Poincaré-sphere equivalent for light beams containing orbital angular momentum," in *Optical Angular Momentum* (CRC Press, 2016), Vol. **24**, pp. 257–259.
101. L. Allen, J. Courtial, and M. J. Padgett, "Matrix formulation for the propagation of light beams with orbital and spin angular momenta," Phys. Rev. E - Stat. Physics, Plasmas, Fluids, Relat. Interdiscip. Top. **60**, 7497–7503 (1999).
102. J. Courtial and M. J. Padgett, "Performance of a cylindrical lens mode converter for producing Laguerre-Gaussian laser modes," Opt. Commun. **159**, 13–18 (1999).
103. M. R. Dennis, "Rows of optical vortices from elliptically perturbing a high-order beam," Opt. Lett. **31**, 1325 (2006).
104. T. Ohtomo, S.-C. Chu, and K. Otsuka, "Generation of vortex beams from lasers with controlled Hermite- and Ince-Gaussian modes," Opt. Express **16**, 5082 (2008).
105. S.-C. Chu, Y.-T. Chen, K.-F. Tsai, and K. Otsuka, "Generation of high-order Hermite-Gaussian modes in end-pumped solid-state lasers for square vortex array laser beam generation," Opt. Express **20**, 7128 (2012).
106. V. V. Kotlyar, A. A. Kovalev, and A. P. Porfirev, "Astigmatic laser beams with a large orbital angular momentum," Opt. Express **26**, 141 (2018).
107. V. Y. Bazhenov, M. V. Vasnetsov, and M. S. Soskin, "Laser beams with screw dislocations in their wavefronts," JETP Lett **52**, 429–431 (1990).
108. M. Szatkowski, J. Masajada, I. Augustyniak, and K. Nowacka, "Generation of composite vortex beams by independent Spatial Light Modulator pixel addressing," Opt. Commun. **463**, 125341 (2020).
109. S. S. R. Oemrawsingh, E. R. Eliel, J. P. Woerdman, E. J. K. Verstegen, J. G. Kloosterboer, and G. W. 'T Hooft, "Half-integral spiral phase plates for optical wavelengths," in *Journal of Optics A: Pure and Applied Optics* Vol. **6** (2004).
110. L. Torner, J. P. Torres, and S. Carrasco, "Digital spiral imaging," Opt. Express (2005).
111. P. S. Tan, X. C. Yuan, G. H. Yuan, and Q. Wang, "High-resolution wide-field standing-wave surface plasmon resonance fluorescence microscopy with optical vortices," Appl. Phys. Lett. **97**, 241109 (2010).
112. C. Zhang, C. Min, L. Du, and X. C. Yuan, "Perfect optical vortex enhanced surface plasmon excitation for plasmonic structured illumination microscopy imaging," Appl. Phys. Lett. **108**, 201601 (2016).
113. X. Xie, Y. Chen, K. Yang, and J. Zhou, "Harnessing the point-spread function for high-resolution far-field optical microscopy," Phys. Rev. Lett. **113**, 263901 (2014).
114. S. Wei, T. Lei, L. Du, C. Zhang, H. Chen, Y. Yang, S. W. Zhu, and X.-C. Yuan, "Sub-100nm resolution PSIM by utilizing modified optical vortices with fractional topological charges for precise phase shifting," Opt. Express **23**, 30143-3014 (2015).
115. Y. Kozawa, D. Matsunaga, and S. Sato, "Superresolution imaging via superoscillation focusing of a radially polarized beam," Optica **5**, 86-92 (2018).
116. A. Ashkin, J. E. Bjorkholm, J. M. Dziedzic, and S. Chu, "Observation of a single-beam gradient force optical trap for dielectric particles," Opt. Lett. **11**, 288–290 (1986).
117. V. Y. Bazhenov, M. S. Soskin, and M. V. Vasnetsov, "Screw dislocations in light wavefronts," J. Mod. Opt. **39**, 985-990 (1992).
118. L. Paterson, M. P. MacDonald, J. Arlt, W. Sibbett, P. E. Bryant, and K. Dholakia, "Controlled

rotation of optically trapped microscopic particles," Science **292**, 912 (2001).
119. N. B. Simpson, K. Dholakia, L. Allen, and M. J. Padgett, "Mechanical equivalence of spin and orbital angular momentum of light: An optical spanner," in *Optical Angular Momentum* (2016).
120. Z. Shen, L. Su, X.-C. Yuan, and Y.-C. Shen, "Trapping and rotating of a metallic particle trimer with optical vortex," Cite as Appl. Phys. Lett **109**, 241901 (2016).
121. S. Qiu, Q. Shao, Y. Ren, T. Liu, L. Chen, Z. Li, and C. Wang, "Manipulate and detect the rotation speed of particles simultaneously using perfect vortex," **11338**, 1133810 (2019).
122. M. J. Snadden, A. S. Bell, R. B. M. Clarke, E. Riis, and D. H. McIntyre, "Doughnut mode magneto-optical trap," J. Opt. Soc. Am. B **14**, 544-552 (1997).
123. T. Kuga, Y. Torii, N. Shiokawa, T. Hirano, Y. Shimizu, and H. Sasada, "Novel Optical Trap of Atoms with a Doughnut Beam," Phys. Rev. Lett. **78**, 4713 (1997).
124. A. T. O'Neil, I. MacVicar, L. Allen, and M. J. Padgett, "Intrinsic and Extrinsic Nature of the Orbital Angular Momentum of a Light Beam," Phys. Rev. Lett. **88**, 053601 (2002).
125. S. C. Chapin, V. Germain, and E. R. Dufresne, "Automated trapping, assembly, and sorting with holographic optical tweezers," Opt. Express **14**, 13095-13100 (2006).
126. M. Woerdemann, C. Alpmann, and C. Denz, "Optical assembly of microparticles into highly ordered structures using Ince-Gaussian beams," Appl. Phys. Lett. **98**, 111101 (2011).
127. M. P. MacDonald, L. Paterson, K. Volke-Sepulveda, J. Arlt, W. Sibbett, and K. Dholakia, "Creation and manipulation of three-dimensional optically trapped structures," Science **296**, 1101-1103 (2002).
128. S. H. Tao, X.-C. Yuan, J. Lin, X. Peng, and H. B. Niu, "Fractional optical vortex beam induced rotation of particles," Opt. Express **13**, 7726-7731 (2005).
129. L. Gong, B. Gu, G. Rui, Y. Cui, Z. Zhu, and Q. Zhan, "Optical forces of focused femtosecond laser pulses on nonlinear optical Rayleigh particles," Photon. Res. **6**, 138-143 (2018)
130. G. D. M. Jeffries, J. S. Edgar, Z. Yiqiong, J. P. Shelby, F. Christine, and D. T. Chiu, "Using polarization-shaped optical vortex traps for single-cell nanosurgery," Nano Lett. **7**, 415–420 (2007).
131. D. J. Richardson, J. M. Fini, and L. E. Nelson, "Space-division multiplexing in optical fibres," Nat. Photonics **7**, 354–362 (2013).
132. S. M. Haas, J. H. Shapiro, and V. Tarokh, "Space-time codes for wireless optical communications," EURASIP J. Appl. Signal Processing **200**2, 478950 (2002).
133. J. T. Barreiro, T. C. Wei, and P. G. Kwiat, "Beating the channel capacity limit for linear photonic superdense coding," Nat. Phys. **4**, 282–286 (2008).
134. J. Wang, J. Y. Yang, I. M. Fazal, N. Ahmed, Y. Yan, H. Huang, Y. Ren, Y. Yue, S. Dolinar, M. Tur, and A. E. Willner, "Terabit free-space data transmission employing orbital angular momentum multiplexing," Nat. Photonics **6**, 488–496 (2012).
135. N. Bozinovic, Y. Yue, Y. Ren, M. Tur, P. Kristensen, H. Huang, A. E. Willner, and S. Ramachandran, "Terabit-scale orbital angular momentum mode division multiplexing in fibers," Science **340**, 1545–1548 (2013).
136. M. P. J. Lavery, C. Peuntinger, K. Günthner, P. Banzer, D. Elser, R. W. Boyd, M. J. Padgett, C. Marquardt, and G. Leuchs, "Free-space propagation of high-dimensional structured optical fields in an urban environment," Sci. Adv. **3** (2017).
137. L. Li, R. Zhang, Z. Zhao, G. Xie, P. Liao, K. Pang, H. Song, C. Liu, Y. Ren, G. Labroille, P. Jian, D. Starodubov, B. Lynn, R. Bock, M. Tur, and A. E. Willner, "High-Capacity Free-Space Optical Communications between a Ground Transmitter and a Ground Receiver via a UAV Using Multiplexing of Multiple Orbital-Angular-Momentum Beams," Sci. Rep. **7**, 17427 (2017).
138. Y. Yan, G. Xie, M. P. J. Lavery, H. Huang, N. Ahmed, C. Bao, Y. Ren, Y. Cao, L. Li, Z. Zhao, A. F. Molisch, M. Tur, M. J. Padgett, and A. E. Willner, "High-capacity millimetre-wave communications with orbital angular momentum multiplexing," Nat. Commun. **5**, 4876 (2014).
139. P. Jia, Y. Yang, C. J. Min, H. Fang, and X.-C. Yuan, "Sidelobe-modulated optical vortices for free-space communication," Opt. Lett. **38**, 588-590 (2013).
140. J. A. Anguita, J. Herreros, and J. E. Cisternas, "Generation and detection of multiple coaxial vortex beams for free-space optical communications," in *Optics InfoBase Conference Papers* (2012).

141. Y. Ren, L. Li, Z. Wang, S. M. Kamali, E. Arbabi, A. Arbabi, Z. Zhao, G. Xie, Y. Cao, N. Ahmed, Y. Yan, C. Liu, A. J. Willner, S. Ashrafi, M. Tur, A. Faraon, and A. E. Willner, "Orbital angular momentum-based space division multiplexing for high-capacity underwater optical communications," Sci. Rep. **6**, 3306 (2016).
142. L. Zhu, A. Wang, S. Chen, J. Liu, Q. Mo, C. Du, and J. Wang, "Orbital angular momentum mode groups multiplexing transmission over 26-km conventional multi-mode fiber," Opt. Express **25**, 25637-25645 (2017).
143. M. Mafu, A. Dudley, S. Goyal, D. Giovannini, M. McLaren, M. J. Padgett, T. Konrad, F. Petruccione, N. Lütkenhaus, and A. Forbes, "Higher-dimensional orbital angular momentum based quantum key distribution with mutually unbiased bases," Phys. Rev. A - At. Mol. Opt. Phys. **88**, (2014).
144. A. Sit, B. Heim, C. Peuntinger, C. Marquardt, D. Elser, E. Karimi, F. Bouchard, G. Leuchs, H. Larocque, J. Gagnon-Bischoff, K. Günthner, K. Heshami, R. Fickler, and R. W. Boyd, "High-dimensional intracity quantum cryptography with structured photons," Optica **4**, 1006–1010 (2017).
145. A. Nicolas, L. Veissier, L. Giner, E. Giacobino, D. Maxein, and J. Laurat, "A quantum memory for orbital angular momentum photonic qubits," Nat. Photonics **8**, 234–238 (2014).
146. Z. Q. Zhou, Y. L. Hua, X. Liu, G. Chen, J. S. Xu, Y. J. Han, C. F. Li, and G. C. Guo, "Quantum Storage of Three-Dimensional Orbital-Angular-Momentum Entanglement in a Crystal," Phys. Rev. Lett. **115**, 070502 (2015).
147. D. S. Ding, W. Zhang, Z. Y. Zhou, S. Shi, G. Y. Xiang, X. S. Wang, Y. K. Jiang, B. Sen Shi, and G. C. Guo, "Quantum storage of orbital angular momentum entanglement in an atomic ensemble," Phys. Rev. Lett. **114**, 050502 (2015).
148. L. Chen, J. Lei, and J. Romero, "Quantum digital spiral imaging," Light Sci. Appl. **3**, e153–e153 (2014).
149. X. L. Wang, X. D. Cai, Z. E. Su, M. C. Chen, D. Wu, L. Li, N. Le Liu, C. Y. Lu, and J. W. Pan, "Quantum teleportation of multiple degrees of freedom of a single photon," Nature (2015).
150. A. Forbes, B. Ndagano, C. Rosales-Guzman, I. Nape, and M. A. Cox, "Creation and Detection of Vector Vortex Modes for Classical and Quantum Communication," J. Light. Technol. **36**, 292–301 (2018).
151. E. Otte, C. Rosales-Guzmán, B. Ndagano, C. Denz, and A. Forbes, "Entanglement beating in free space through spin-orbit coupling," Light Sci. Appl. **7**, 18009 (2018).
152. K. Toyoda, F. Takahashi, S. Takizawa, Y. Tokizane, K. Miyamoto, R. Morita, and T. Omatsu, "Transfer of light helicity to nanostructures," Phys. Rev. Lett. **110**, 143603. (2013).
153. Y. Jin, O. J. Allegre, W. Perrie, K. Abrams, J. Ouyang, E. Fearon, S. P. Edwardson, and G. Dearden, "Dynamic modulation of spatially structured polarization fields for real-time control of ultrafast laser-material interactions," Opt. Express **21**, 25333-25343 (2013).
154. O. J. Allegre, Y. Jin, W. Perrie, J. Ouyang, E. Fearon, S. P. Edwardson, and G. Dearden, "Complete wavefront and polarization control for ultrashort-pulse laser microprocessing," Opt. Express **21**, 21198-21207 (2013).
155. K. Toyoda, K. Miyamoto, N. Aoki, R. Morita, and T. Omatsu, "Using optical vortex to control the chirality of twisted metal nanostructures," Nano Lett. **12**, 3645–3649 (2012).
156. S. Syubaev, A. Zhizhchenko, A. Kuchmizhak, A. Porfirev, E. Pustovalov, O. Vitrik, Y. Kulchin, S. Khonina, and S. Kudryashov, "Direct laser printing of chiral plasmonic nanojets by vortex beams," Opt. Express **25**, 10214 (2017).
157. K. Masuda, S. Nakano, D. Barada, M. Kumakura, K. Miyamoto, and T. Omatsu, "Azo-polymer film twisted to form a helical surface relief by illumination with a circularly polarized Gaussian beam," Opt. Express **25**, 12499-12507 (2017).
158. F. Takahashi, K. Miyamoto, H. Hidai, K. Yamane, R. Morita, and T. Omatsu, "Picosecond optical vortex pulse illumination forms a monocrystalline silicon needle," Sci Rep **6**, 21738 (2016).
159. L. Yang, D. Qian, C. Xin, Z. Hu, S. Ji, D. Wu, Y. Hu, J. Li, W. Huang, and J. Chu, "Direct laser writing of complex microtubes using femtosecond vortex beams," Appl. Phys. Lett. **110**, 221103 (2017).
160. S. Freidank, A. Vogel, and N. Linz, "Optical Vortex Beam for Gentle and Ultraprecise

Intrastromal Corneal Dissection in Refractive Surgery," Transl. Vis. Sci. Technol. **9**, 22–22 (2020).
161. J. Leach, M. J. Padgett, S. M. Barnett, S. Franke-Arnold, and J. Courtial, "Measuring the Orbital Angular Momentum of a Single Photon," Phys. Rev. Lett. **88**, 257901 (2002).
162. M. Harwit, "Photon Orbital Angular Momentum in Astrophysics," Astrophys. J. **597**, 1266 (2003).
163. G. A. Swartzlander, "The optical vortex coronagraph," J. Opt. A Pure Appl. Opt. **11**, 094022 (2009).
164. D. W. Wilson, D. M. Palacios, E. L. Ford, G. A. Swartzlander, L. M. Close, M. A. Peters, and R. S. Abdul-Malik, "Astronomical demonstration of an optical vortex coronagraph," Opt. Express **16**, 10200–10207 (2008).
165. A. Thompson, "New method could image Earth-like planets," https://www.nbcnews.com/id/wbna36528711.
166. D. Mawet, P. Riaud, O. Absil, and J. Surdej, "Annular Groove Phase Mask Coronagraph," Astrophys. J. **633**, 1191 (2005).
167. O. Absil, D. Mawet, M. Karlsson, B. Carlomagno, V. Christiaens, D. Defrère, C. Delacroix, B. F. Castella, P. Forsberg, J. Girard, C. A. G. González, S. Habraken, P. M. Hinz, E. Huby, A. Jolivet, K. Matthews, J. Milli, G. O. de Xivry, E. Pantin, P. Piron, M. Reggiani, G. J. Ruane, G. Serabyn, J. Surdej, K. R. W. Tristram, E. V. Catalán, O. Wertz, and P. Wizinowich, "Three years of harvest with the vector vortex coronagraph in the thermal infrared," Ground-based Airborne Instrum. Astron. VI **9908**, 99080Q (2016).
168. M. Takeda, R. Ishijima, S. G. Hanson, T. Yokozeki, and W. Wang, "Optical vortex metrology based on the core structures of phase singularities in Laguerre-Gauss transform of a speckle pattern," Opt. Express, **14**, 10195–10206 (2006).
169. M. P. J. Lavery, F. C. Speirits, S. M. Barnett, and M. J. Padgett, "Detection of a spinning object using light's orbital angular momentum," Science **341**, 537-540 (2013).
170. N. Cvijetic, G. Milione, E. Ip, and T. Wang, "Detecting lateral motion using light's orbital angular momentum," Sci. Rep. **5**, 15422 (2015).
171. G. Xie, H. Song, Z. Zhao, G. Milione, Y. Ren, C. Liu, R. Zhang, C. Bao, L. Li, Z. Wang, K. Pang, D. Starodubov, M. Tur, and A. E. Willner, "Using a Complex Optical Orbital-Angular-Momentum Spectrum to Measure Object Parameters: A Spatial Domain Approach," Opt. Lett. **42**, 4482-4485 (2017).
172. J. A. O. Huguenin, L. da Silva, M. H. M. Passos, M. R. Lemos, S. R. Almeida, and W. F. Balthazar, "Speckle patterns produced by an optical vortex and its application to surface roughness measurements," Appl. Opt. **56**, 330–335 (2017).
173. A. Sihvola, *Electromagnetic Mixing Formulas and Applications* (IET, 1999).
174. S. Kirkpatrick, C. D. Gelatt, and M. P. Vecchi, "Optimization by simulated annealing," Science **220**, 671–680 (1983).
175. A. K. Hartmann and H. Rieger, *Optimization Algorithms in Physics*, 1st editio (Wiley-VCH Verlag Berlin GmbH, 2002).
176. V. A. Markel, "Introduction to the Maxwell Garnett approximation: tutorial," J. Opt. Soc. Am. A **33**, 1244-1256 (2016).
177. A. Filipkowski, H. T. Nguyen, R. Kasztelanic, J. Cimek, R. Stępień, D. Pysz, M. Trippenbach, and R. Buczynski, "Development of nanostructured GRIN microlenses with temperature-controlled diffusion," **27**, 21 (2019).
178. A. Filipkowski, *Fabrication and Integration of Nanostructured Optical Devices* (2015).
179. N. Metropolis, A. W. Rosenbluth, M. N. Rosenbluth, A. H. Teller, and E. Teller, "Equation of state calculations by fast computing machines," J. Chem. Phys. (1953).
180. R. Stepien, J. Cimek, D. Pysz, I. Kujawa, M. Klimczak, and R. Buczynski, "Soft glasses for photonic crystal fibers and microstructured optical components," Opt. Eng. (2014).
181. D. Pysz, I. Kujawa, R. Stepien, M. Klimczak, A. Filipkowski, M. Franczyk, L. Kociszewski, J. Buzniak, K. Harasny, and R. Buczynski, "Stack and draw fabrication of soft glass microstructured fiber optics," Bull. Polish Acad. Sci. Tech. Sci. (2014).
182. J. M. Nowosielski, R. Buczynski, F. Hudelist, A. J. Waddie, and M. R. Taghizadeh, "Nanostructured GRIN microlenses for Gaussian beam focusing," Opt. Commun. **283**, 1938–

1944 (2010).
183. K. Okamoto, *Fundamentals of Optical Waveguides* (2006).
184. J. W. Goodman, *Introduction to Fourier Optics, Second Edition*, Opt. Eng. (1996).
185. A. Anuszkiewicz, R. Kasztelanic, A. Filipkowski, G. Stepniewski, T. Stefaniuk, B. Siwicki, D. Pysz, M. Klimczak, and R. Buczynski, "Fused silica optical fibers with graded index nanostructured core," Sci. Rep. **8**, (2018).
186. J. Cimek, R. Stępień, G. Stępniewski, B. Siwicki, P. Stafiej, M. Klimczak, D. Pysz, and R. Buczyński, "High contrast glasses for all-solid fibers fabrication," Opt. Mater. **62**, 159-163 (2016).
187. G. Zhao, Z. Wei, W. Wang, D. Feng, A. Xu, W. Liu, and Z. Song, "Review on modeling and application of chemical mechanical polishing," Nanotechnol. Rev. (2020).
188. G. Campbell, B. Hage, B. Buchler, and P. K. Lam, "Generation of high-order optical vortices using directly machined spiral phase mirrors," Appl. Opt. **51**, 873-876 (2012).
189. J. Wang, A. Cao, M. Zhang, H. Pang, S. Hu, Y. Fu, L. Shi, and Q. Deng, "Study of Characteristics of Vortex Beam Produced by Fabricated Spiral Phase Plates," IEEE Photonics J. **8**, 1-9 (2016).
190. V. Denisenko, V. Shvedov, A. S. Desyatnikov, D. N. Neshev, W. Krolikowski, A. Volyar, M. Soskin, and Y. S. Kivshar, "Determination of topological charges of polychromatic optical vortices," Opt. Express **17**, 23374 (2009).
191. C. He, J. Chang, Q. Hu, J. Wang, J. Antonello, H. He, S. Liu, J. Lin, B. Dai, D. S. Elson, P. Xi, H. Ma, and M. J. Booth, "Complex vectorial optics through gradient index lens cascades," Nat. Commun. **10**, 1–8 (2019).
192. A. Filipkowski, A. Anuszkiewicz, D. Pysz, M. Bidus, M. Dlubek, R. Buczynski, and R. Buczynski, "Experimental analysis of axial stress distribution in nanostructured core fused silica fibers," Opt. Mater. Express **9**, 4370–4378 (2019).
193. R. Kingslake and R. B. Johnson, *Lens Design Fundamentals* (Elsevier Inc., 2010).
194. N. Davidson, A. A. Friesem, and E. Hasman, "Analytic design of hybrid diffractive–refractive achromats," Appl. Opt. **32**, 4770 (1993).
195. R. A. Flynn, E. F. Fleet, G. Beadie, and J. S. Shirk, "Achromatic GRIN singlet lens design," Opt. Express **21**, 4970 (2013).
196. J. N. Mait, G. Beadie, P. Milojkovic, and R. A. Flynn, "Chromatic analysis and design of a first-order radial GRIN lens," Opt. Express **23**, 22069 (2015).
197. J. Pniewski, R. Kasztelanic, J. M. Nowosielski, A. Filipkowski, B. Piechal, A. J. Waddie, D. Pysz, I. Kujawa, R. Stepien, M. R. Taghizadeh, and R. Buczynski, "Diffractive optics development using a modified stack-and-draw technique," Appl. Opt. **55**, 4939 (2016).
198. A. J. Waddie, R. Buczynski, F. Hudelist, J. Nowosielski, D. Pysz, R. Stepien, and M. R. Taghizadeh, "Form birefringence in nanostructured micro-optical devices," Opt. Mater. Express **1**, 1251 (2011).
199. M. J. Riedl, *Optical Design Fundamentals for Infrared Systems, Second Edition* (SPIE, 2001).